



Thomas Suppan, BSc

# Tomographic Volume Concentration Estimation in Pneumatic Conveying from Capacitive Data

**Master's Thesis**

to achieve the university degree of

Master of Science

Master's degree programme: Electrical Engineering

submitted to

**Graz University of Technology**

Supervisor

Dipl.-Ing. Dr.techn. Markus Neumayer

Institute of Electrical Measurement and Measurement Signal Processing

Graz, May 2018



## Abstract

Pneumatic conveying systems have become the most common transport system for bulk materials such as granulates or powdery. An important parameter for flow measurement is the so called volume concentration. This thesis investigates the capability of electrical capacitance tomography (ECT) to estimate the volume concentration in pneumatic conveying processes from capacitive sensor data. ECT is a non-invasive imaging technique, providing information about the spacial material distribution within the sensor. The reconstruction of the material distribution by means of ECT is a so called ill-posed inverse problem. In order to solve this kind of problem, meaningful prior information about the material distribution has to be incorporated. For this reason the different flow patterns occurring in pneumatic conveying systems are investigated. To formulate a prior distribution for those flow regimes a sample based approach is presented. Within the Bayesian framework different reconstruction algorithms are derived and adapted for this specific application. The reconstruction result of ECT is given by the spacial distribution of the relative permittivity. This information is used to estimate the volume concentration within the sensor. A framework is presented for a comprehensive statistical analyses of the estimation quality of different reconstruction algorithms and material distributions. In the course of this analyses it is shown, that the incorporation of specific prior knowledge about flow patterns leads to a significant improvement of the estimation result. Lastly selected parameter studies are implemented in order to analyse the impact on the estimation results.



## Kurzfassung

Pneumatische Fördersysteme zählen zu den wichtigsten Transportsystemen für die Beförderung von Schüttgütern wie Granulaten oder Pulvern. Zur Erfassung des Durchflusses eines pneumatische Förderprozesses ist die Ermittlung der Volumenkonzentration erforderlich. In dieser Arbeit wird die Schätzung dieses Parameters mittels elektrischer Kapazitätstomografie (ECT) aus kapazitiven Messdaten untersucht. Die ECT ist eine nicht invasive bildgebende Technik, welche Informationen über die räumliche Materialverteilung innerhalb eines Sensors liefert. Die Rekonstruktion der Materialverteilung mittels ECT stellt ein schlechtgestelltes inverses Problem dar. Die Einbringung sinnvoller Vorinformation über die Materialverteilungen ist nötig, um Probleme dieser Art lösen zu können. In der pneumatische Förderung von Schüttgut bildet das Förderregime eine Quelle für die Konstruktion von Vorwissen. Um diese Strömungsprofile als A-priori-Verteilung zu formulieren wird ein Sample basierter Ansatz präsentiert. Im Bayesschen Rahmen werden verschiedene Rekonstruktionsalgorithmen abgeleitet und für die spezifische Anwendung adaptiert. Das ECT Rekonstruktionsergebnis ist durch die räumliche Verteilung der relativen Permittivität des Schüttgutes gegeben. Aus dieser kann die Volumenkonzentration innerhalb des Sensors bestimmt werden. In der Arbeit wird ein Framework präsentiert welches umfangreiche statistische Analysen der Schätzqualität für verschiedene Rekonstruktionsalgorithmen und Materialverteilungen ermöglicht. In Zuge dieser Analysen wird gezeigt, dass die Einbringung von spezifischer Vorinformation für Strömungsprofile eine signifikante Verbesserung der Schätzergebnisse mit sich bringt. Zudem werden die Eigenschaften des Messsystems hinsichtlich des Einflusses auf das Messergebnis untersucht.



## **Acknowledgment**

In the first place I want to thank my supervisor Markus Neumayer for his commitment and support in order to enable the success of this thesis.

Particular thanks also go to my family for supporting me, to all those people responsible for the fact that I am supplied with coffee and everyone else who contributed to the success of this thesis.



## Eidesstattliche Erklärung

Ich erkläre an Eides statt, dass ich die vorliegende Arbeit selbstständig verfasst, andere als die angegebenen Quellen/Hilfsmittel nicht benutzt, und die den benutzten Quellen wörtlich und inhaltlich entnommenen Stellen als solche kenntlich gemacht habe.

Graz, am .....

.....

(Unterschrift)

## Statutory Declaration

I declare that I have authored this thesis independently, that I have not used other than the declared sources / resources, and that I have explicitly marked all material which has been quoted either literally or by content from the used sources.

Graz, the .....

.....

(Signature)



# Contents

<b>1</b>	<b>Introduction</b>	<b>1</b>
1.1	Problem Statement and Motivation . . . . .	1
1.2	Electrical Capacitance Tomography . . . . .	3
1.2.1	Inverse Problems . . . . .	5
1.3	Volume Concentration Estimation by means of ECT . . . . .	7
1.4	Thesis Outline . . . . .	8
<b>2</b>	<b>ECT Framework</b>	<b>10</b>
2.1	The Physics of ECT . . . . .	10
2.1.1	ECT specific Simplifications . . . . .	11
2.2	Measurement Process . . . . .	13
2.3	Standard Finite Element Simulation . . . . .	14
2.3.1	Charge Computation . . . . .	16
2.3.2	Computation of Derivatives . . . . .	16
2.4	Fast Simulation Framework . . . . .	17
2.4.1	Fast Stiffness Matrix Assembly . . . . .	17
2.4.2	Charge Map . . . . .	19
2.4.3	Green's Functions . . . . .	20
2.4.4	Summary of the Forward Map . . . . .	21
2.4.5	Jacobian Operations . . . . .	22
2.4.6	Exact Fast Low-Rank Updates . . . . .	24
2.5	Calibration . . . . .	25
<b>3</b>	<b>Reconstruction Algorithms</b>	<b>27</b>
3.1	Bayesian Inversion . . . . .	27
3.2	Sample based Prior and Gaussian Summary Statistics . . . . .	29
3.2.1	Generation of Random Samples . . . . .	29
3.2.2	Gaussian Summary Statistics . . . . .	31
3.3	Prior Based State Reduction . . . . .	32
3.4	Linear Back Projection Type Algorithms . . . . .	33
3.4.1	Sample based Back Projection Algorithms . . . . .	34

3.4.2	Linearised MAP and ML type Estimator . . . . .	35
3.5	Non-linear Iterative Methods . . . . .	38
3.5.1	Kalman Filter . . . . .	38
3.5.2	Gibbs Sampler . . . . .	43
<b>4</b>	<b>Flow Parameter Estimation</b>	<b>47</b>
4.1	Flow Regimes in Pneumatic Conveying Systems . . . . .	47
4.1.1	Random Samples for Flow Patterns . . . . .	49
4.2	Analysis of the Intrinsic Information of the Prior Samples . . .	52
4.2.1	Principle Component Analysis . . . . .	53
4.2.2	An Intuitive Approach for the Reduced State Representation for Flow Patterns . . . . .	56
4.3	Estimation of the Volume Concentration by means of ECT . .	58
4.4	Reconstruction Algorithm Setup and Notation . . . . .	60
4.4.1	Algorithm Setup . . . . .	60
4.4.2	Summary and Notation of the Algorithms . . . . .	62
<b>5</b>	<b>Case Studies for the Reconstruction Behaviour</b>	<b>64</b>
5.1	Reconstruction Algorithm Overview . . . . .	64
5.2	Simulation Setup . . . . .	66
5.2.1	Simulation Procedure . . . . .	66
5.2.2	Simulation Parameters . . . . .	68
5.2.3	Representation of the Simulation Results . . . . .	69
5.3	Simulation Study for Different Material Distributions . . . . .	70
5.3.1	Simulation Results for Rod Type Samples . . . . .	70
5.3.2	Simulation Results for Gaussian Type Samples . . . . .	74
5.3.3	Simulation Results for Horizontal Conveying Flow Samples . . . . .	77
5.3.4	Simulation Results for Vertical Downward Conveying Flow Samples . . . . .	80
5.3.5	Detailed Error Analysis . . . . .	84
5.4	Simulations with Non-linear Iterative Algorithms . . . . .	86
5.4.1	Simulation Results . . . . .	86
5.5	Selected Parameter Studies . . . . .	88
5.5.1	Variation of the Number of Electrodes . . . . .	88
5.5.2	Impact of Measurement Noise . . . . .	90
5.5.3	Variation of the Material Values . . . . .	91
5.5.4	Variations in the Flow Profile . . . . .	96
<b>6</b>	<b>Summary and Conclusion</b>	<b>104</b>

**CONTENTS**

---

**iii**

**References**

**107**

# 1 Introduction

## 1.1 Problem Statement and Motivation

Pneumatic conveying has become an important transport system for bulk materials such as powdery or granulates. In pneumatic conveying processes the solid bulk material is transported by means of streaming gas within a closed process pipe. One important parameter to determine the state of the conveying process is given by the mass flow rate  $\dot{m}(t)$  defined by

$$\dot{m}(t) = \iint_{\Gamma_{\text{ROI}}} \rho(x, y, t) v(x, y, t) dx dy. \quad (1.1)$$

Herby  $\rho(x, y, t)$  denotes the instantaneous density at position  $(x, y)$  in  $\text{kg/m}^3$  and  $v(x, y, t)$  denotes the instantaneous velocity at the same position in  $\text{m/s}$  [1].  $\Gamma_{\text{ROI}}$  denotes the cross section of the process pipe in  $\text{m}^2$ . Common techniques for the continuous determination of the mass flow rate of solid bulk material are for example scale based techniques or baffle plates. In pneumatic conveying those mentioned techniques are limited applicable due to several reasons. To outline the drawbacks of common methods for the measurement based determination of the mass flow rate, one has to discuss the processes within pneumatic conveying systems in more detail.

Different spacial material distributions occur in pneumatic conveying processes, which are termed flow regimes. Those flow regimes mainly depend on the gas velocity. Figure 1.1 sketches the often used phase diagram to describe the relation between the gas velocity and the pressure drop and depict the resulting flow regimes [2]. High gas velocities and low pressure drops cause the so called dilute flow. This flow regime is characterized by a low density, with particles distributed over the whole cross section of the process pipe. For decreasing gas velocities a growing ground layer appears until the so called slug flow is reached. Slug flow is caused by very low gas velocities and high pressure drops also termed dense flow. Here the ground layer can

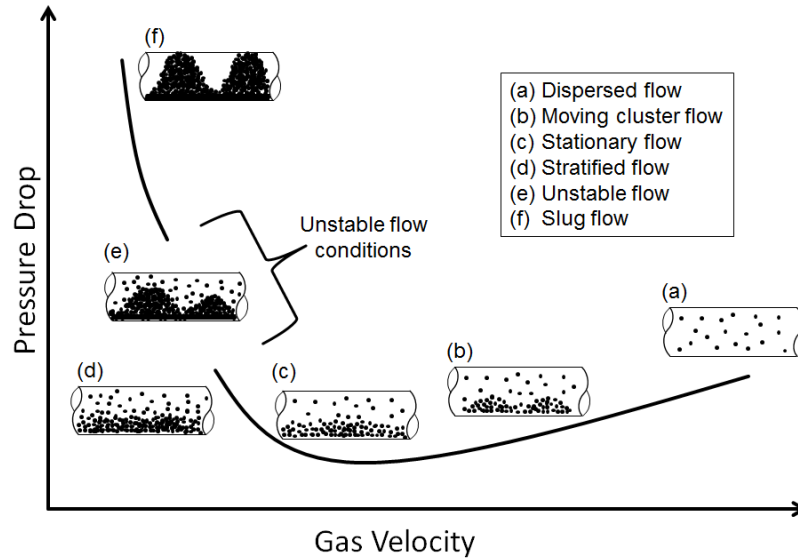


**Figure 1.1:** Flow regimes in pneumatic conveying as a function of the gas velocity and the pressure drop [2].

cover the whole cross section of the pipe [2].

Given this overview about the occurring flow regimes in pneumatic conveying systems the drawbacks of methods like scale based techniques or baffle plates becomes evident.

Scale based techniques requires the bulk material to causes a gravitational force on the weighting instrumentation. In the case of dilute flow the solid particles are distributed over the whole cross section of the process pipe with a low density. Therefore the particles are not able to cause a gravitational force on the weighting instrumentation. For this reason scale based techniques are unsuitable for the determination of the mass flow rate in pneumatic conveying systems.

Baffle plates use the impact force of the bulk material on the plate to continuously determine the mass flow rate. This highly invasive measurement principle causes significantly increased pressure drops along the process pipe. For this reason this measurement principle makes the conveying process more likely to clog, especially for dense flow regimes.

Having addressed the limiting properties of common mass flow rate measurement techniques for bulk materials with respect to pneumatic conveying, the necessity of a non-invasive measurement principle becomes obvious. There are several non-invasive sensing techniques available. Amongst them are electrical measurement principles such as capacitive sensing. In capacitive sensing a number of electrodes are mounted on the process pipe. The material distribution within the pipe influences the capacitances between the electrodes. Given the capacitive sensor data, conclusions about the material distribution within the sensor can be made. One possible approach for this task is tomographic signal processing leading to the technique of electrical capacitance tomography.

## 1.2 Electrical Capacitance Tomography

Electrical capacitance tomography (ECT) is an imaging technique, which provides information about the spacial permittivity distributions within the cross section of the process pipe. Although the achievable resolution of ECT is comparatively low, it was already shown that ECT is a suitable technique to estimate flow profiles within pneumatic conveying systems [3]. This is of particular interest with respect to pneumatic conveying since the behaviour of the conveying process depends on the different flow regimes. For this reason it is reasonable to investigate ECT also about the usability for the estimation of the mass flow rate  $\dot{m}(t)$ . Therefore, this section is intended to provide the reader with the measurement principle and the properties of ECT.

A scheme of an ECT sensor is depicted in figure 1.2. A number of  $N_{\text{elec}}$  electrodes is mounted on the surface of a non conductive tube. The measurements of the ECT sensor are the capacitances between the electrodes, the so called inter-electrode capacitances. A typical measurement pattern is shown in figure 1.3 [7]. For a sensor with  $N_{\text{elec}}$  electrodes, the number of independent measurements is given by

$$M = \frac{N_{\text{elec}}(N_{\text{elec}} - 1)}{2}. \quad (1.2)$$

The task is to reconstruct the material distribution within the sensor, which is referred to as region of interest (ROI). The material distribution within the ECT sensor modulates the inter-electrode capacitances. This measurement process is used to determine the spacial material distribution in the ROI from the measurements [7].

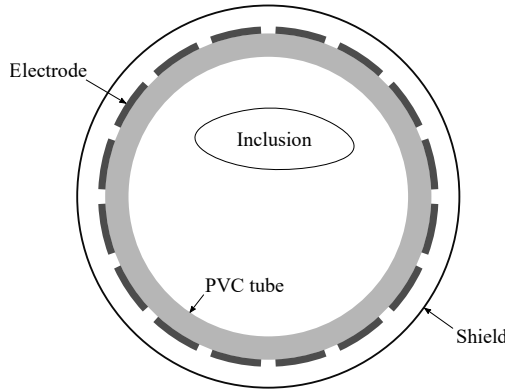


**Figure 1.2:** Scheme of the ECT sensor.

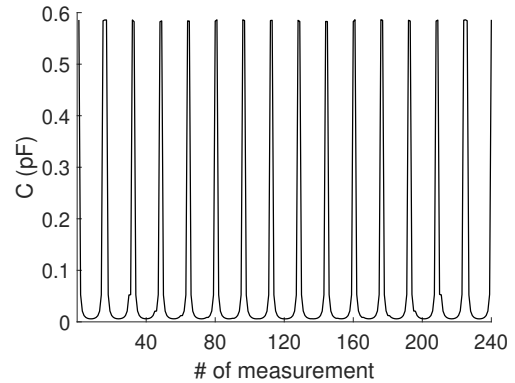


**Figure 1.3:** Typical ECT measurement pattern [7].

The estimation of the spacial material distribution is an indirect measurement problem, also termed inverse problem, since the quantity of interest can not be measured in a direct way. The inverse problem of ECT is of ill-posed nature since there usually exists no unique solution [5]. This circumstance is given by the fact, that the information obtained by the measured inter-electrode capacitances is not sufficient for the reconstruction of the spacial material distribution with an acceptable resolution.

Tomography systems can be classified by the way, the physical quantity used for the measurement system interacts with the object. Tomographic methods like for example *x*-ray tomography, where the direction of the physical quantity is not influenced in its direction are termed as so called hard field tomography. The beam passes straight trough the object and is influenced only in its intensity. Tomographic systems where the physical quantity is influenced in its direction between material transitions are classified to be so called soft field tomography systems. Since the distribution of the displacement currents and consequently also the inter-electrode capacitances are influenced by material transitions, ECT belongs to the class of soft field tomography. For this reason ECT systems suffers from drawbacks in resolution compared to hard field systems [7].

The interaction of the field with objects also results in different achievable resolutions for different regions within the ECT sensor. In other words, soft field systems are suffering from a spatial dependence of the sensitivity. For capacitive measurement systems like ECT, the sensitivity is usually decreasing with the distance to the electrodes. This causes a lower sensitivity in the

center of the pipe compared to regions near the electrodes.

Because of this circumstances, the inverse problem of ECT is generally hard to solve and the achievable resolutions are comparatively low with respect to hard field systems. Nevertheless ECT has several advantages, which may make it preferable compared to other tomography systems. The main advantage of electrical methods like ECT is the simple hardware concept, since only some electrodes and the measurement circuitry are necessary. Therefore ECT also requires less space to mount. It should also be kept in mind, that ECT produces no ionizing radiation, which makes it a save sensing technology compared to methods like  $x$ -ray or  $\gamma$ -ray [7].

Even though the real ECT sensor is always a three dimensional system, the solution of the inverse problem is usually done for a two dimensional model. Thus, the reconstruction result provides only the cross section of the material distribution. This simplification of the simulation model is only reasonable, if the electrodes have a certain length with respect to the diameter of the process pipe [7] due to boundary effects. Generally the 2D model is accurate enough, if the length of the electrodes is in the range of the diameter of the tube [8]. If this does not hold, 3D effects are not negligible and the 2D model will provide wrong results.

Also the number of electrodes is a crucial parameter for the design of a ECT sensor. Sensors with a number of electrodes between 8 and 16 are typically [8]. As the number of information obtained from an ECT sensor is increased with the number of electrodes, there where also designs of ECT systems with an increased number of smaller electrodes. Certainly the number of measurements is increased with this design. However such systems also suffer from a decreased signal to noise ratio (SNR). The inter-electrode capacitances decrease due to the smaller areas of the electrodes [7].

### 1.2.1 Inverse Problems

Since the estimation task of ECT is an ill-posed inverse problem, this section should provide a short introduction into the basics of inverse problems. Inverse problems are problems where a quantity of interest  $\phi$  can only be observed in an indirect way [9]. In the case of ECT,  $\phi$  is given by the spacial permittivity distribution within the sensor. To draw conclusions about the quantity of interest measurements  $\tilde{\mathbf{d}} \in \mathbb{R}^M$  are made, which are affected by  $\phi$ . In this particular case  $\tilde{\mathbf{d}}$  is a vector holding the measured inter-electrode capacitances. The physical relation between the quantity of interest  $\phi$  and

the measurement  $\tilde{\mathbf{d}}$  is given by the measurement process  $\mathbf{P}$  [10]. Given this, the problem can be formulated by

$$\tilde{\mathbf{d}} = \mathbf{P}(\phi, \mathbf{v}), \quad (1.3)$$

where  $\mathbf{v}$  denotes the measurement noise. To obtain information about  $\phi$  from the data  $\tilde{\mathbf{d}}$ , the development of a mathematical model, which describes the measurement process  $\mathbf{P}$  is necessary.

The first step of this modeling process concerns the representation of  $\phi$  itself.  $\phi$  presents the continuous cross sectional material distribution within the ECT sensor. For the mathematical model the continuous material distribution has to be presented with single numbers. For this reason a mapping  $D : \phi \mapsto \mathbf{x}$  has to be formulated to describe the quantity of interest  $\phi$  by means of the so called state vector  $\mathbf{x} \in \mathbb{R}^N$ . This step is often referred to as data modeling. One way to do so, is the discretization of the cross section. For this representation of  $\phi$  the further modeling of the measurement process by means of the finite element method is obvious. Given this approach the material values of the finite elements within the ECT sensor can be summarized by means of the state vector  $\mathbf{x}$ . Note that the representation of  $\phi$  is always a problem dependent task and there is no predetermined way for this step of the modeling process.

In the next step the measurement process  $\mathbf{P}$  itself has to be formulated by means of a mathematical expression leading to the so called measurement model. The mapping  $\mathbf{F} : \mathbf{x} \mapsto \mathbf{y}$  is referred to as forward map with the claim that

$$\mathbf{F}(\mathbf{x}) = \mathbf{P}(\mathbf{x}) \quad \forall \mathbf{x}, \quad (1.4)$$

holds. In other words, the model output  $\mathbf{y} \in \mathbb{R}^M$  is equal to the noise free data  $\mathbf{d} = \mathbf{P}(\mathbf{x})$  [10]. As it is usually not possible to consider every physical effect and due to numerical inaccuracy the relation given by equation (1.4) will not exactly hold, but

$$\mathbf{F}(\mathbf{x}) \approx \mathbf{P}(\mathbf{x}), \quad (1.5)$$

holds instead. The model error  $\mathbf{e}$  is introduced given by

$$\mathbf{e} = \mathbf{P}(\mathbf{x}) - \mathbf{F}(\mathbf{x}). \quad (1.6)$$

Calibration schemes are needed to reduce model errors. Using calibration techniques, the inverse problem can be solved for real measurements or for simulated measurements coming from a more detailed process model [10]. This is necessary for the real testing of reconstruction algorithms. Generating the simulated measurement with the same model, which is used for the reconstruction algorithms is referred to as inverse crime [9].

For the consideration of measurement noise  $\mathbf{v}$  the so called noise model is necessary. For the statistical properties of the measurement noise usually Gaussian distributions with zero mean  $\mathbf{v} \propto \mathcal{N}(\mathbf{0}, \mathbf{\Sigma}_{\mathbf{v}})$  are assumed.  $\mathbf{\Sigma}_{\mathbf{v}}$  denotes the covariance matrix of the measurement noise. For a fully description of the measurement noise, not only the the statistical properties are necessary but also how the noise free measurements are corrupted by the noise  $\mathbf{v}$ . For example

$$\tilde{\mathbf{d}} = \mathbf{P}(\mathbf{x}) + \mathbf{v}, \tag{1.7}$$

is referred to as additive noise model.

The definition of well posed problems was introduced by Hadamard [5] given by the properties that:

- A solution exists.
- The solution is unique.
- The solution continuously depends on the data.

If one of these points do not hold, the problem is of ill-posed nature. Since the size of the state vector  $N$  is usually much larger than the number of measurements  $M$ , the inverse problem of ECT is of ill-posed nature. To obtain stable solutions for ill-posed inverse problems the so called prior model is required. With this model prior information about the state vector  $\mathbf{x}$  is incorporated. To construct this model, the knowledge about the properties of  $\phi$  has to be transformed into conditions for  $\mathbf{x}$ .

### 1.3 Volume Concentration Estimation by means of ECT

To determine the mass flow rate by means of ECT, equation (1.1) has to be modified. Assuming bulk materials with a constant density  $\rho_S$ , the instantaneous density can be replaced by

$$\rho(x, y, t) = \rho_S \beta_S(x, y, t), \tag{1.8}$$

with the unitless instantaneous solid volume concentration  $\beta_S(x, y, t)$  at position  $(x, y)$ . For uniform flows, where the particles moves along their flow lines with constant velocity, equation (4.2) is simplified to [4]

$$\dot{m}(t) = \rho_S \Gamma_{\text{ROI}} \bar{v}(t) \bar{\beta}_S(t). \tag{1.9}$$

Here,  $\bar{v}(t)$  denotes the cross-sectional average velocity of the solid particles and  $\bar{\beta}_S(t)$  denotes the cross-sectional average solid volume concentration at time instant  $t$ . Thus the mass flow rate  $\dot{m}(t)$  can be described by means of the two parameters  $\bar{v}(t)$  and  $\bar{\beta}_S(t)$ . The aim of the present thesis is the estimation of the cross-sectional average solid volume concentration  $\bar{\beta}_S$  by means of the spacial permittivity distributions provided by an ECT sensor. This estimation is based on the assumption, that the instantaneous density  $\rho(x, y, t)$  is related to the relative permittivity  $\varepsilon_r$  by

$$\rho(x, y, t) \propto \varepsilon_r(x, y, t) - 1 = \chi(x, y, t). \quad (1.10)$$

Hereby  $\chi(x, y, t)$  denotes the instantaneous susceptibility. This assumption enables the application of ECT to the task of volume concentration estimation in pneumatic conveying systems.

The continuous metrological registration of the mass flow rate is required for the state determination of the conveying process. For this reason the issue of computational costs has to be taken into account. The imaging task of ECT is of ill-posed inverse nature and the relation between the measurements and spacial permittivity distribution is highly non-linear. For this reasons the reconstruction of the material distributions within the ECT sensor can be a computational expensive problem. A multitude of different reconstruction algorithms is available for the solution of such problems. Amongst others are also linear back projection type algorithms. This kind of algorithms are given by a simple matrix vector multiplication, using linear approximations of the problem. The main drawback of linearisation techniques is given by the fact, that they will fail for large deviations from the linearization point. In the case of ECT and pneumatic conveying this means that the differences in the permittivity values of the bulk materials and the gas used for the conveying process has to be small. This usually is indeed the case in pneumatic conveying systems [6]. The permittivity values for common bulk materials are usually low. This enables the application of ECT for the continuous determination of flow parameters in pneumatic conveying systems. Therefore the main focus of this thesis lies on the estimation of the cross-sectional average solid volume concentration  $\bar{\beta}_S$  by means of linear back projection type algorithms.

## 1.4 Thesis Outline

This section contains the outline of this thesis given by a short summary of the content attributed to each chapter.

- The **second chapter** provides the computational framework of the sensor. This framework contains the mathematical model of the measurement process and gives also access to derivative informations such as the Jacobian matrix. In the first sections the physical effects within the sensor and the measurement process are discussed leading to a standard FEM simulation model. For an efficient solution of the forward problem and fast access to derivative informations adaptations of the standard FEM are presented. This leads to a simulation framework with superior numerical performance.
- The **third chapter** concerns the solution of the ill-posed inverse problem of ECT. For this reason the fundamentals of Bayesian inversion theory are provided. The construction of a sample based prior is presented and different way to incorporate this information to the reconstruction algorithms. Within the Bayesian framework different reconstruction algorithms are derived, which are classified by linear back projection type algorithms and non-linear iterative algorithms.
- In the **fourth chapter** the particular application of ECT for the estimation of flow parameters is addressed. Therefore, flow patterns occurring in pneumatic conveying systems are investigated to construct a meaningful sample based prior for reconstruction of flow patterns. In the next section the intrinsic information of this sample based prior is analysed and compared to sample based priors for arbitrary material distributions. The reconstruction result of ECT is given by the relative permittivity values of the finite elements. A linear approach is presented to relate these electrical material values with the flow parameter of interest. In the last section of this chapter the setup of each implemented reconstruction algorithm is discussed in detail.
- The **fifth chapter** contains case studies for the behaviour of different algorithms in order to estimate the cross-sectional average solid volume concentration  $\bar{\beta}_S$ . Hence comprehensive statistical analysis of the estimation results for linear back projection type algorithms are implemented. For non-linear iterative algorithms only a few examples are illustrated. Lastly selected parameter studies are presented in order to analyse the impact of particular process parameters on the estimation results.

## 2 ECT Framework

This chapter is intended to give the reader a basic understanding of the physical effects within an ECT sensor. Given this insight a finite element framework for the simulation of the ECT sensor will be provided. This framework comprises a set of functions to simulate the measurement process, which is referred to as forward map. The framework gives also access to derivative information such as the Jacobian matrix. As computational costs are an immanent issue for solving inverse problems, methods are introduced, which provide superior numerical performance for the simulation of the ECT sensor. Detailed informations about the fast simulation framework can be found in [10]. Since the modeling process of the ECT Sensor includes some simplifications and assumptions also model errors have to be considered. A way to minimize the impact of model errors is a correction of the model output, leading to the topic of calibration, which is also discussed in this chapter.

### 2.1 The Physics of ECT

The sensing principle of ECT is of electrical nature. The partial differential equations (PDE) describing the dominating physical effects within the sensor are given by Maxwell's equations [11]

$$\nabla \times \mathbf{H} = \mathbf{J} + \frac{\partial \mathbf{D}}{\partial t}, \quad (2.1)$$

$$\nabla \times \mathbf{E} = -\frac{\partial \mathbf{B}}{\partial t}, \quad (2.2)$$

$$\nabla \cdot \mathbf{B} = 0, \quad (2.3)$$

$$\nabla \cdot \mathbf{D} = \rho. \quad (2.4)$$

$\mathbf{H}$  denotes the magnetic field in  $\text{Am}^{-1}$ ,  $\mathbf{E}$  denotes the electric field in  $\text{Vm}^{-1}$ ,  $\mathbf{B}$  denotes the magnetic flux density in  $\text{Vsm}^{-2}$ ,  $\mathbf{D}$  denotes the electric displacement in  $\text{Asm}^{-2}$  and  $\mathbf{J}$  denotes the current density in  $\text{Am}^{-2}$ . Equation (2.1)

is called Ampere's circuital law. It states that electric currents as well as time varying displacement current cause a magnetic field. Equation (2.2) is termed Faraday's law of induction and it says that  $\mathbf{E}$  is generated by means of a time varying magnetic field. Equation (2.3) is sometimes termed as Gauss's law of magnetism. It has the interpretation, that no magnetic sources exist. Equation (2.3) is called Gauss's law and it states that charges  $\rho$  are the source of the electric field. The three material equations are given by

$$\mathbf{B} = \mu\mathbf{H}, \quad (2.5)$$

$$\mathbf{D} = \varepsilon\mathbf{E}, \quad (2.6)$$

$$\mathbf{J} = \sigma\mathbf{E}, \quad (2.7)$$

where  $\mu$  denotes the magnetic permeability,  $\varepsilon$  denotes the dielectric permittivity and  $\sigma$  denotes the conductivity. The permeability is given by  $\mu = \mu_0\mu_r$ , with the absolute permeability  $\mu_0 = 4\pi \cdot 10^{-7} \text{ VsA}^{-1}\text{m}^{-1}$  and the dimensionless relative permeability  $\mu_r$ . In the same way the permittivity is given by  $\varepsilon = \varepsilon_0\varepsilon_r$  with the absolute permittivity  $\varepsilon_0 = 8,854 \cdot 10^{-12} \text{ AsV}^{-1}\text{m}^{-1}$  and the dimensionless relative permittivity  $\varepsilon_r$ . The third material equation results in Ohm's law. It describes the relation between the current density  $\mathbf{J}$  and the electric field  $\mathbf{E}$ . The physical unit of the conductivity  $\sigma$  is given by  $\Omega^{-1}\text{m}^{-1}$ .

### 2.1.1 ECT specific Simplifications

Maxwell's equations describe the physical effects within the ECT sensor. However, for ECT it is common to make specific assumptions given by [7]:

- The magnetic fields inside the sensor have no influence on the electric field.
- The conductivity of the materials is zero.
- Absence of charges.

Given this simplifications the derivation of a partial differential equation, which covers the important sensor effects is provided in this subsection. This step is required for an efficient solution of the inverse problem since the reduced set of Maxwell's equations is more suitable for the simulation of the sensor.

The first assumption is the main simplification for the derivation of the ECT simulation model as it reduces the type of the partial differential equation to a Laplace type PDE. With this the second Maxwell's equation is given by

$$\nabla \times \mathbf{E} = -\frac{\partial \mathbf{B}}{\partial t} = \mathbf{0}. \quad (2.8)$$

This simplification is valid since the wave lengths due to the typical frequency range are typically several times larger than the sensor dimensions [7].

As equation (2.8) states that the electric field  $\mathbf{E}$  has no curl, the scalar potential  $V$  in V (Volt) can be introduced. Then the electric field  $\mathbf{E}$  can be expressed by

$$\mathbf{E} = -\nabla V. \quad (2.9)$$

For general vector fields  $\mathbf{A}$  the relation

$$\nabla \cdot (\nabla \times \mathbf{A}) = 0, \quad (2.10)$$

holds. Hence the divergence of Amperes law (2.1) leads to

$$\nabla \cdot \left( \mathbf{J} + \frac{\partial \mathbf{D}}{\partial t} \right) = 0. \quad (2.11)$$

For harmonic signals the Fourier transform can be applied

$$\nabla \cdot (\mathbf{J} + j\omega \mathbf{D}) = 0, \quad (2.12)$$

with the circular frequency given by  $\omega = 2\pi f$  and the frequency  $f$  in Hz. Applying the material relations (2.6) and (2.7) results in

$$\nabla \cdot (\sigma \mathbf{E} + j\omega \varepsilon_0 \varepsilon_r \mathbf{E}) = 0. \quad (2.13)$$

With the definition of the scalar potential given by equation (2.9), the relation (2.13) becomes

$$-\nabla \cdot ((\sigma + j\omega \varepsilon_0 \varepsilon_r) \nabla V) = 0. \quad (2.14)$$

Since the absence of conductive materials is assumed, equation (2.14) is reduced to

$$-\nabla \cdot (j\omega \varepsilon_0 \varepsilon_r \nabla V) = 0, \quad (2.15)$$

which can be further simplified to

$$\nabla \cdot (\varepsilon_r \nabla V) = 0, \quad (2.16)$$

as neither  $j\omega$  nor  $\varepsilon_0$  has an impact on the solution  $V$ . This elliptic PDE will be used for the simulation of the ECT sensor.

## 2.2 Measurement Process

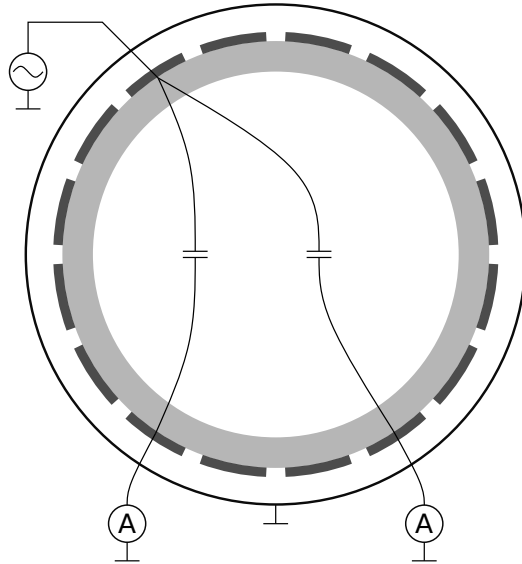


**Figure 2.1:** Scheme of the measurement process [7].

The solution of the PDE (2.16) requires boundary conditions. These boundary conditions are depending on the way the ECT sensor is operated in order to determine the inter-electrode capacitances. This section provides the realization of the measurement process to subsequently obtain the required boundary conditions for the simulation model of the ECT sensor.

Figure 2.1 depicts the principle of the measurement process. Due to the low input impedance of the measurement circuitry this scheme is stated as low- $Z$  measurement instrumentation. Detailed information about the circuitry for ECT can be found in [12].

The determination of the impedances between the electrodes is done by the following steps:

- An AC voltage source is connected to one electrode, which is termed as active electrode or transmitter electrode.
- The other electrodes are connected to ground potential through a low input impedance circuitry. These electrodes are referred to as receiver electrodes.

- The inter-electrode capacitances are obtained by measuring the displacement currents by means of the relation

$$i = \frac{u}{\frac{1}{j\omega C}} = j\omega C u. \quad (2.17)$$

Although AC signals have to be used for the measurement process, an electrostatic simulation is sufficient as  $i \propto Q$  holds.

Given this measurement principle, the Dirichlet boundary conditions for the partial differential equation (2.16) can be formulated as

$$V_{\Gamma_i} = V_0, \quad (2.18)$$

$$V_{\Gamma_j} = 0 \quad \forall j \neq i, \quad (2.19)$$

$$V_{\partial\Omega} = 0. \quad (2.20)$$

$\Gamma_i$  denotes the surface of the  $i^{\text{th}}$  electrode and  $\partial\Omega$  denotes the shield of the ECT sensor shown in figure 1.2 and 2.2. Using the solution  $V_i$  with the  $i^{\text{th}}$  electrode active and the relations (2.6) and (2.9), the total surface charge  $Q_j$  on the  $j^{\text{th}}$  electrode can be computed by

$$\begin{aligned} Q_j &= \int_{\Omega_j} \rho d\Omega = \int_{\Omega_j} \nabla \cdot \mathbf{D} d\Omega = \oint_{\Gamma_j} \mathbf{D} \mathbf{n} d\Gamma \\ &= - \oint_{\Gamma_j} \varepsilon_0 \varepsilon_r \nabla V_i \mathbf{n} d\Gamma. \end{aligned} \quad (2.21)$$

This integral is known as Gauss's law. The inter-electrode capacitance can be determined with the relation  $Q = CV_0$ , leading to the result

$$C_{i,j} = -\frac{1}{V_0} \oint_{\Gamma_j} \varepsilon_0 \varepsilon_r \nabla V_i \mathbf{n} d\Gamma. \quad (2.22)$$

## 2.3 Standard Finite Element Simulation

This section provides a standard finite element (FEM) forward map of the ECT sensor [13]. The forward problem refers to the computation of the inter-electrode capacitances for a given material distribution inside the domain  $\Omega_{\text{ROI}}$ . ROI denotes the region of interest, which in this case is the inner tube of the ECT sensor. The different domains of the ECT model are depicted in figure 2.2.

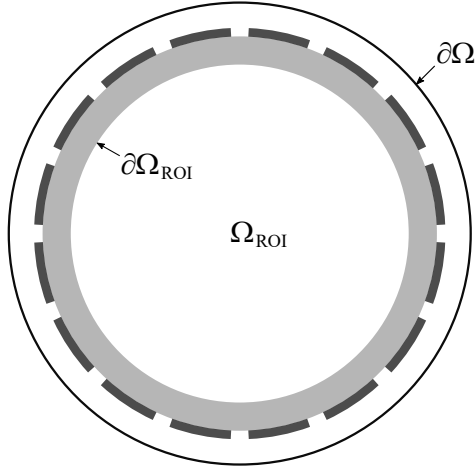


**Figure 2.2:** Domains of the ECT sensor.  $\Omega$  denotes the whole problem domain.

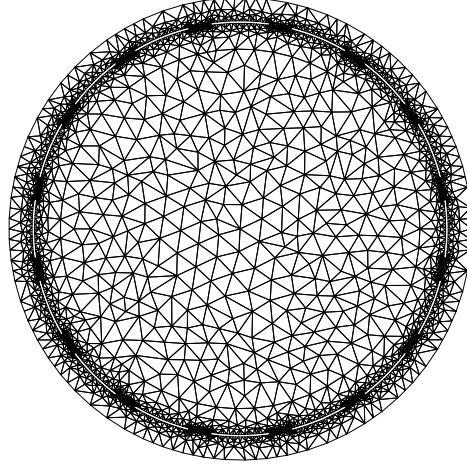


**Figure 2.3:** Exemplary mesh with triangular FE.

The approach of the FEM is based on the discretization of the whole problem domain  $\Omega$  by means of so called finite elements (FE). Figure 2.3 depict an exemplary FE mesh for the ECT sensor. Within the domain  $\Omega_{\text{FE}}$  of each FE the scalar potential  $V$  is approximated by means of a superposition of the basis functions  $N_i$  with the weights  $v_i$  given by

$$V \approx \sum_i v_i N_i. \quad (2.23)$$

Thereby the index  $i$  indicates the nodes of the FE. Figure 2.3 depict a exemplary FE discretization for the ECT sensor with triangular finite elements. In the next step the element matrix  $\tilde{\mathbf{K}}_{\text{FE},i}$  is assembled for each FE. The coefficients of this matrix are given by

$$\tilde{k}_{i,j} = \int_{\Omega_{\text{FE}}} (\nabla N_i)^T (\nabla N_j) \, d\Omega, \quad (2.24)$$

termed Ritz-Galerkin equation. Given the element matrices the so called stiffness matrix is assembled by means of

$$\mathbf{K} = \bigcup_{i=1}^{N_{\text{FE}}} \varepsilon_i \tilde{\mathbf{K}}_{\text{FE},i}, \quad (2.25)$$

whereby  $N_{\text{FE}}$  denotes the number of FE and  $\varepsilon_i$  denotes the material value of the  $i^{\text{th}}$  FE. The stiffness matrix  $\mathbf{K}$  forms a discrete representation of the

PDE (2.16) for the approximation of the scalar potential  $V$  given by (2.23). As no boundary conditions are yet incorporated to the problem,  $\mathbf{K}$  forms a singular matrix. Including the Dirichlet type boundary conditions presented in section 2.2 to the problem leads to the non-singular matrix  $\hat{\mathbf{K}}$ . Detailed information about the incorporation of the boundary conditions can be found in [7]. Given this approach, the solution of the partial differential equation (2.16) for the boundary conditions (2.18) to (2.20) results in a linear equation system of the form

$$\hat{\mathbf{K}}\mathbf{v} = \mathbf{r}. \quad (2.26)$$

Here  $\mathbf{v}$  denotes the solution vector holding the potentials  $v_i$  of each node and  $\mathbf{r}$  is referred to as right hand side vector.

Equation (2.26) provides the solution of one field problem also referred to as solver run. The simulation of the ECT sensor requires one solver run for each electrode is once set as active. Therefore the equation system (2.26) can be extended to the form

$$\hat{\mathbf{K}}\mathbf{V} = \mathbf{R}, \quad (2.27)$$

where  $\hat{\mathbf{K}}$  is the common stiffness matrix.  $\mathbf{V}$  is a matrix holding the  $N_{\text{elec}}$  solution vectors  $\mathbf{v}$  in each column, whereby  $N_{\text{elec}}$  denotes the number of electrodes.  $\mathbf{R}$  contains the  $N_{\text{elec}}$  right hand side vectors in each column

### 2.3.1 Charge Computation

To avoid the computation of the gradient  $\nabla V$ , the charge computation shown in equation (2.21) can also be done with the so called charge method [14] given by

$$Q_j = \sum_{n_j} (\mathbf{K}\mathbf{v})_{n_j}. \quad (2.28)$$

$(\mathbf{K}\mathbf{v})_{n_j}$  denotes the scalar product between the solution vector  $\mathbf{v}$  and the rows of the matrix  $\mathbf{K}$  that correspond to the nodes of the finite element mesh, which are located on the boundary of the electrode  $j$ .  $\mathbf{K}$  is the stiffness matrix without boundary conditions.

### 2.3.2 Computation of Derivatives

Some reconstruction algorithms presented in the later chapter 3 are using linear approximations of the forward map. Therefore the computation of derivatives, especially the Jacobian, defined by

$$\mathbf{J} = [\nabla C_1 \quad \nabla C_2 \quad \dots \quad \nabla C_N]^T, \quad (2.29)$$

is of special interest with respect to the solution of inverse problem.  $\nabla C_i$  is the gradient of the  $i^{\text{th}}$  inter-electrode capacitance with respect to the permittivity values of the finite elements in  $\Omega_{\text{ROI}}$ .

There are efficient methods for the the computation of the Jacobian such as the so called adjoint variable method [15] given by

$$dC_{i,j} = \boldsymbol{\gamma}_i^T \left[ \left[ \frac{\partial \mathbf{r}}{\partial \varepsilon_k} \right] - \left[ \frac{\partial \hat{\mathbf{K}}}{\partial \varepsilon_k} \right] \mathbf{v}_j \right] d\varepsilon_k. \quad (2.30)$$

For this approach the the adjoint solution  $\boldsymbol{\gamma}_i$  has to be evaluated by solving

$$\hat{\mathbf{K}} \boldsymbol{\gamma}_i = \frac{\partial C_{i,j}}{\partial \mathbf{v}_j}. \quad (2.31)$$

Although the adjoint variable method is quiet efficient, still one computation of the forward problem is necessary to obtain the adjoint solution. For this reason more efficient methods are required, which are presented in the next section.

## 2.4 Fast Simulation Framework

In this section methods are presented for a fast and efficient simulation of the ECT sensor. This efficient framework provides the same results as the standard methods presented in section 2.3 but has superior numerical properties. This enables the fast simulation the ECT sensor in order to solve the ill-posed inverse problem within an appropriate time.

### 2.4.1 Fast Stiffness Matrix Assembly

The update of the stiffness matrix  $\hat{\mathbf{K}}$  after a change in the material distribution requires the evaluation of equation (2.25), which is computationally expensive.

Given the domains depict in figure 2.2, the whole problem domain  $\Omega$  within the boundary  $\partial\Omega$  can be decomposed into two domains. A material depending domain  $\Omega_{\text{ROI}}$  within the boundary  $\partial\Omega_{\text{ROI}}$  and a domain with constant material values  $\Omega_{\text{ini}} = \Omega \setminus \Omega_{\text{ROI}}$ . This domain decomposition can be used to derive a faster method for assembling the stiffness matrix  $\hat{\mathbf{K}}$ .

The Dirichlet boundary conditions given by equation (2.18) to (2.20) are the potentials on the electrodes and the shield of the ECT sensor. Therefore  $\Omega_{\text{ini}}$  also contains the boundary conditions. With this the FE equation system can be assembled by

$$\hat{\mathbf{K}} = \hat{\mathbf{K}}_{\text{ini}} \cup \mathbf{K}_{\text{ROI}}, \quad (2.32)$$

where  $\hat{\mathbf{K}}_{\text{ini}}$  is the constant part of the stiffness matrix representing the domain  $\Omega_{\text{ini}}$ , which already contains the boundary conditions.  $\mathbf{K}_{\text{ROI}}$  is the material dependent part of  $\hat{\mathbf{K}}$  representing the domain  $\Omega_{\text{ROI}}$ . Similar to equation (2.25) the assembly of  $\mathbf{K}_{\text{ROI}}$  is done by

$$\mathbf{K}_{\text{ROI}} = \bigcup_{i=1}^{N_{\text{FE,ROI}}} \varepsilon_i \tilde{\mathbf{K}}_{\text{FE,ROI},i}, \quad (2.33)$$

where  $N_{\text{FE,ROI}}$  denotes the number of FE in ROI and  $\mathbf{K}_{\text{FE,ROI}}$  denotes the element matrices of the FE within ROI. This approach already reduces the computational effort, though the assembly of (2.33) by means of a loop implementation is still slow. A faster way is based on an eigenvalue decomposition of the element matrices  $\tilde{\mathbf{K}}_{\text{FE,ROI},i}$  [10]. For an arbitrary quadratic matrix  $\mathbf{A}$  the eigenvalue decomposition is given by

$$\mathbf{A} = \mathbf{V}\mathbf{D}\mathbf{V}^{-1}. \quad (2.34)$$

The columns of the matrix  $\mathbf{V}$  hold the eigenvectors of the matrix  $\mathbf{A}$ .  $\mathbf{D}$  is a diagonal matrix holding the eigenvalues of  $\mathbf{A}$ . For the matrix  $\mathbf{A}$  being symmetric, which holds for the element matrices, the inverse  $\mathbf{V}^{-1}$  in equation (2.34) can be replaced by the transposed  $\mathbf{V}^T$ . The further procedure to obtain an efficient way for the assembly of  $\hat{\mathbf{K}}$  by means of this eigenvalue decomposition is now illustrated for one  $3 \times 3$  element matrix  $\tilde{\mathbf{K}}_{\text{FE,ROI}}$ . The eigenvalue decomposition is given by

$$\tilde{\mathbf{K}}_{\text{FE,ROI}} = [\mathbf{v}_1 \quad \mathbf{v}_2 \quad \mathbf{v}_3] \begin{bmatrix} d_1 & 0 & 0 \\ 0 & d_2 & 0 \\ 0 & 0 & d_3 \end{bmatrix} \begin{bmatrix} \mathbf{v}_1^T \\ \mathbf{v}_2^T \\ \mathbf{v}_3^T \end{bmatrix}, \quad (2.35)$$

where  $\mathbf{v}_i$  denotes the eigenvectors and  $d_i$  denotes the eigenvalues of  $\mathbf{K}_{\text{FE,ROI}}$ . Since the finite element matrices of the considered partial differential equation are positive semi-definite one eigenvalue is zero. Hence the matrix  $\mathbf{K}_{\text{FE,ROI}}$  can be assembled by the eigenvectors of the two non zero eigen-

values by

$$\begin{aligned}
\tilde{\mathbf{K}}_{\text{FE,ROI}} &= [\mathbf{v}_1 \quad \mathbf{v}_2 \quad \mathbf{v}_3] \begin{bmatrix} d_1 & 0 & 0 \\ 0 & d_2 & 0 \\ 0 & 0 & 0 \end{bmatrix} \begin{bmatrix} \mathbf{v}_1^T \\ \mathbf{v}_2^T \\ \mathbf{v}_3^T \end{bmatrix} \\
&= [\sqrt{d_1}\mathbf{v}_1 \quad \sqrt{d_2}\mathbf{v}_2] \begin{bmatrix} \sqrt{d_1}\mathbf{v}_1^T \\ \sqrt{d_2}\mathbf{v}_2^T \end{bmatrix} \\
&= \mathbf{a}_1\mathbf{a}_1^T + \mathbf{a}_2\mathbf{a}_2^T,
\end{aligned} \tag{2.36}$$

where the vectors  $\mathbf{a}_i$  are given by

$$\mathbf{a}_i = \sqrt{d_i}\mathbf{v}_i. \tag{2.37}$$

The vectors  $\mathbf{a}_i$  of each finite element in  $\Omega_{\text{ROI}}$  are now used to assemble the sparse matrix  $\mathbf{A}_i$  by the following principle:

- The vectors  $\mathbf{a}_i$  are in each case assigned to one column of  $\mathbf{A}_i$ .
- The global numbers of the finite element determine the row positions of the vectors  $\mathbf{a}_i$ .

Given this approach the matrix  $\mathbf{K}_{\text{ROI}}$  can be computed by

$$\hat{\mathbf{K}} = \hat{\mathbf{K}}_{\text{ini}} + \mathbf{A}_1\boldsymbol{\mathcal{E}}\mathbf{A}_1^T + \mathbf{A}_2\boldsymbol{\mathcal{E}}\mathbf{A}_2^T, \tag{2.38}$$

where  $\boldsymbol{\mathcal{E}}$  denotes a sparse diagonal matrix holding the permittivity values of the finite elements in  $\Omega_{\text{ROI}}$ . This equation only contains sparse matrix operations, which reduces the computational effort for the assembly of the stiffness matrix  $\hat{\mathbf{K}}$  significantly.

### 2.4.2 Charge Map

Given the concept of the domain decomposition depict in figure 2.2, also the computation of the charges can be done in a more efficient way. This is done by separating the  $N_{\text{elec}} \times N_{\text{elec}}$  charge matrix  $\mathbf{Q}$  in a constant part  $\mathbf{Q}_a$  and a part  $\mathbf{Q}_c$  depending on the potential distribution on  $\partial\Omega_{\text{ROI}}$  by [10]

$$\mathbf{Q} = \mathbf{Q}_a + \mathbf{Q}_c\mathbf{V}_{\partial\Omega_{\text{ROI}}}. \tag{2.39}$$

Hereby  $\mathbf{V}_{\partial\Omega_{\text{ROI}}}$  denotes a matrix holding the finite element solutions  $\mathbf{v}_{\partial\Omega_{\text{ROI}}}$  on  $\partial\Omega_{\text{ROI}}$  as column vectors. The matrix  $\mathbf{Q}_c : \mathbf{v}_{\partial\Omega_{\text{ROI}}} \mapsto \Delta\mathbf{Q}$  is referred to as charge map.

### Computation of $\mathbf{Q}_a$

The constant part  $\mathbf{Q}_a$  is obtained by solving the partial differential equation (2.16) in the domain  $\Omega_{\text{ini}}$  for the boundary conditions

$$V_{\Gamma_i} = V_0, \quad (2.40)$$

$$V_{\Gamma_j} = 0 \quad \forall j \neq i, \quad (2.41)$$

$$V_{\partial\Omega} = 0, \quad (2.42)$$

$$V_{\partial\Omega_{\text{ROI}}} = 0, \quad (2.43)$$

and subsequently computing the charges on the electrodes.

### Computation of $\mathbf{Q}_c$

To obtain the charge map  $\mathbf{Q}_c : \mathbf{v}_{\partial\Omega_{\text{ROI}}} \mapsto \Delta\mathbf{Q}$  again the solution of the partial differential equation (2.16) in  $\Omega_{\text{ini}}$  is necessary. This time the PDE is solved for the boundary conditions

$$V_{\Gamma_i} = V_0 \quad \forall i, \quad (2.44)$$

$$V_{\partial\Omega} = 0, \quad (2.45)$$

$$V_{\partial\Omega_{\text{ROI}}} = \delta [\mathbf{z} - \mathbf{z}_{\partial\Omega_{\text{ROI},i}}]. \quad (2.46)$$

Thereby  $\delta[\mathbf{z} - \mathbf{z}_{\partial\Omega_{\text{ROI},i}}]$  denotes applying the potential of 1 V to the  $i^{\text{th}}$  FE node on  $\partial\Omega_{\text{ROI}}$ . The subsequent computation of the charges on the electrodes yield the charge map.

This method requires  $N_{\partial\Omega_{\text{ROI}}}$  solutions of the PDE (2.16) in  $\Omega_{\text{ini}}$  where  $N_{\partial\Omega_{\text{ROI}}}$  denotes the number of FE nodes on the boundary  $\partial\Omega_{\text{ROI}}$ . Since the matrices  $\mathbf{Q}_a$  and  $\mathbf{Q}_c$  are computed in the pre-processing phase, the charge matrix  $\mathbf{Q}$  is obtained by means of a simple matrix multiplication.

### 2.4.3 Green's Functions

In this subsection a Green's functions approach for the computation of the forward map is presented. A detailed derivation of this approach and a proof for the applicability of Green's functions to the finite element equation system for the PDE (2.16) can be found in [10] and [16]. Since  $\hat{\mathbf{K}}$  is symmetric and real valued the property of self adjointness holds for the ECT forward problem. Therefore Green's functions can be applied to the equation system (2.26).

The evaluation of the charge matrix  $\mathbf{Q}$  given by equation (2.39) requires the nodal potentials on the boundary  $\partial\Omega_{\text{ROI}}$ . This can be done by solving the standard ECT forward problem (2.26) and using the components of  $\mathbf{v}$  on  $\partial\Omega_{\text{ROI}}$ . Instead of doing so, the equation system

$$\hat{\mathbf{K}}\mathbf{g}_i = \mathbf{e}_i, \quad (2.47)$$

is solved, where  $\mathbf{g}_i$  denotes the  $i^{\text{th}}$  Green's function and  $\mathbf{e}_i$  is the  $i^{\text{th}}$  unit vector. The index  $i$  belongs to the nodes on  $\partial\Omega_{\text{ROI}}$ . Given the Green's function  $\mathbf{g}_i$ , the potential of the  $i^{\text{th}}$  node  $v_i$  can be computed by

$$v_i = \mathbf{g}_i^T \mathbf{r}. \quad (2.48)$$

For the evaluation of the charge matrix  $\mathbf{Q}$  this concept has to be extended to the equation system

$$\hat{\mathbf{K}}\mathbf{G} = \mathbf{E}_{\partial\Omega_{\text{ROI}}}. \quad (2.49)$$

The matrix  $\mathbf{G}$  holds the  $N_{\partial\Omega_{\text{ROI}}}$  Green's functions and the matrix  $\mathbf{E}_{\partial\Omega_{\text{ROI}}}$  holds the corresponding unit vectors. The potentials of the nodes on the boundary  $\partial\Omega_{\text{ROI}}$  are now given by

$$\mathbf{V}_{\partial\Omega_{\text{ROI}}} = \mathbf{G}^T \mathbf{R}. \quad (2.50)$$

To overcome the computation of the  $N_{\partial\Omega_{\text{ROI}}}$  Green's functions, the equation system (2.49) can be manipulated by the right side multiplication by  $\mathbf{Q}_c^T$

$$\hat{\mathbf{K}}\mathbf{G}\mathbf{Q}_c^T = \mathbf{E}_{\partial\Omega_{\text{ROI}}}\mathbf{Q}_c^T, \quad (2.51)$$

$$\hat{\mathbf{K}}\mathbf{G}_Q = \mathbf{R}_Q. \quad (2.52)$$

This approach reduces the number of equation system down to the original number of  $N_{\text{elec}}$ . The charge matrix  $\mathbf{Q}$  can be computed by

$$\mathbf{Q} = \mathbf{Q}_a + \mathbf{G}_Q^T \mathbf{R}. \quad (2.53)$$

The computational steps of the whole forward map are now reduced to three operations of linear algebra given by equation (2.38), (2.52) and (2.53).

#### 2.4.4 Summary of the Forward Map

This subsection summarizes the computational steps of the ECT forward map. The steps can be distinguished by the pre computation of the constant matrices and the final equations for the simulation of the sensor.

The pre-computation contains the following steps:

- Assembly of the constant part of the stiffness matrix  $\hat{\mathbf{K}}_{\text{ini}}$  and the matrix holding the right hand side vectors  $\mathbf{R}$ .
- Computation of the matrices  $\mathbf{A}_1$  and  $\mathbf{A}_2$  by means of the eigenvector decomposition of the element matrices in  $\Omega_{\text{ROI}}$ .
- Computation of the constant part of the charge matrix  $\mathbf{Q}_a$ .
- Computation of the charge map  $\mathbf{Q}_c$ .
- Computation of the right hand side vectors  $\mathbf{R}_Q = \mathbf{E}_{\partial\Omega_{\text{ROI}}} \mathbf{Q}_c^T$ .

After this pre-computation the ECT sensor can be simulated by

$$\begin{aligned}\hat{\mathbf{K}} &= \hat{\mathbf{K}}_{\text{ini}} + \mathbf{A}_1 \boldsymbol{\varepsilon} \mathbf{A}_1^T + \mathbf{A}_2 \boldsymbol{\varepsilon} \mathbf{A}_2^T, \\ \hat{\mathbf{K}} \mathbf{G}_Q &= \mathbf{R}_Q, \\ \mathbf{Q} &= \mathbf{Q}_a + \mathbf{G}_Q^T \mathbf{R}.\end{aligned}$$

This three equations are used to simulate the ECT sensor and they are referred to as forward map  $\mathbf{F}(\boldsymbol{\varepsilon})$ .

### 2.4.5 Jacobian Operations

Derivative informations about the forward map are of special interest for the solution of inverse problems as mentioned in section 2.3. The Green's function approach can also be used for an efficient evaluation of Jacobian operations. Operating on the Jacobian is referred to the computation of a matrix vector product of the form  $\mathbf{J}\mathbf{x}$  without the explicit computation of the Jacobian  $\mathbf{J}$ . For the vector  $\mathbf{x}$  for example holding a small change in the permittivity values  $\mathbf{x} = d\boldsymbol{\varepsilon}$ , the operation  $\mathbf{J}d\boldsymbol{\varepsilon}$  results in a linear approximation of the forward map, evident in the definition of the Jacobian given by equation (2.29).

The starting point for the derivation of the Jacobian operation is the finite element equation system given by equation (2.26) [10]. A small change in the stiffness matrix  $d\hat{\mathbf{K}}$  results in a change in the solution vector  $d\mathbf{v}$ . This can be formulated by

$$\left( \hat{\mathbf{K}} + d\hat{\mathbf{K}} \right) (\mathbf{v} + d\mathbf{v}) = \mathbf{r}. \quad (2.54)$$

As  $\hat{\mathbf{K}}\mathbf{v} = \mathbf{r}$  holds, this relation can be rearranged to

$$\hat{\mathbf{K}}d\mathbf{v} = -d\hat{\mathbf{K}}(\mathbf{v} + d\mathbf{v}). \quad (2.55)$$

Since the product of differentials cancels out, the change in the solution vector can be expressed by

$$d\mathbf{v} = -\hat{\mathbf{K}}^{-1}d\hat{\mathbf{K}}\mathbf{v}. \quad (2.56)$$

Given this relation the derivative with respect to one material value  $\varepsilon_j$  can be expressed by

$$\frac{d\mathbf{v}}{d\varepsilon_j} = -\hat{\mathbf{K}}^{-1}\frac{d\hat{\mathbf{K}}}{d\varepsilon_j}\mathbf{v}. \quad (2.57)$$

By taking use of the chain rule this expression can be extended to all material values  $\boldsymbol{\varepsilon}$  of the finite elements. This results in

$$\begin{aligned} d\mathbf{v} &= \mathbf{J}\boldsymbol{\varepsilon} = -\sum_j \hat{\mathbf{K}}^{-1}\frac{d\hat{\mathbf{K}}}{d\varepsilon_j}\mathbf{v}d\varepsilon_j \\ &= -\hat{\mathbf{K}}^{-1}\left[\sum_j \frac{d\hat{\mathbf{K}}}{d\varepsilon_j}d\varepsilon_j\right]\mathbf{v} \\ &= -\hat{\mathbf{K}}^{-1}\hat{\mathbf{K}}_{d\boldsymbol{\varepsilon}}\mathbf{v}. \end{aligned}$$

As the problem is self adjoint [10], the use of Green's functions is possible. Hence the inverse  $\hat{\mathbf{K}}^{-1}$  can be replaced by  $\mathbf{G}^T$ . With this  $d\mathbf{v}$  can be expressed by

$$d\mathbf{v} = -\mathbf{G}^T\hat{\mathbf{K}}_{d\boldsymbol{\varepsilon}}\mathbf{G}. \quad (2.58)$$

With this result no matrix inversion is necessary to evaluate  $\mathbf{J}d\boldsymbol{\varepsilon}$ .

To directly work on the charges by means of a Jacobian operation,  $\mathbf{G}$  can be replaced by  $\mathbf{G}_Q$  due to the linearity of the charge map. With this the Jacobian operation becomes

$$d\mathbf{Q} = -\mathbf{G}_Q^T\hat{\mathbf{K}}_{d\boldsymbol{\varepsilon}}\mathbf{G}_Q. \quad (2.59)$$

By taking use of the fast stiffness matrix assembly procedure presented in subsection 2.4.1, the Jacobian operation can be evaluated by

$$d\mathbf{Q} = -\mathbf{G}_Q^T[\mathbf{A}_1d\boldsymbol{\varepsilon}\mathbf{A}_1^T + \mathbf{A}_2d\boldsymbol{\varepsilon}\mathbf{A}_2^T]\mathbf{G}_Q, \quad (2.60)$$

where  $d\boldsymbol{\varepsilon}$  denotes the diagonal matrix holding the changes in the material values.

If an explicit expression of the Jacobian  $\mathbf{J}$  is needed it is also possible to apply this procedure. As this approach results in a matrix vector product, it is possible to apply identity vectors to the diagonal matrix in such a way that

$$\text{diag}(\mathbf{d}\boldsymbol{\mathcal{E}}) = \mathbf{e}_i, \quad (2.61)$$

holds. Afterwards the Jacobian  $\mathbf{J}$  is assembled out of the single results of  $\mathbf{J}\mathbf{e}_i$ .

### 2.4.6 Exact Fast Low-Rank Updates

For solution of the inverse problem an approach for a numerical efficient computation of the forward map for a marginally changed material distribution could be advantageous. This occurs for example when only the material value of one finite element has changed. An appropriate method for this task is the linear approximation by means of the Jacobian. Since this is only an approximation an exact method for this problem is desirable. A method for the exact solution of the forward problem for low rank material updates is given by the Woodbury matrix identity [17]

$$(\mathbf{A} + \mathbf{L}\mathbf{U})^{-1} = \mathbf{A}^{-1} - \mathbf{A}^{-1}\mathbf{L}(\mathbf{I} + \mathbf{U}\mathbf{A}^{-1}\mathbf{L})^{-1}\mathbf{U}\mathbf{A}^{-1}. \quad (2.62)$$

With this it is possible to evaluate the update of the inverse of a matrix without inverting the whole matrix.  $\mathbf{A}$  is a quadratic matrix with the known inverse  $\mathbf{A}^{-1}$ . The small change in the matrix  $\mathbf{A}$  is given by the matrix product  $\mathbf{L}\mathbf{U}$ .  $(\mathbf{I} + \mathbf{U}\mathbf{A}^{-1}\mathbf{L})$  is referred to as Woodbury matrix which is a quadratic matrix of the size of the rank of the update. So for the update of the inverse  $(\mathbf{A} + \mathbf{L}\mathbf{U})^{-1}$  only the Woodbury matrix has to be inverted.

Considering the ECT problem, the matrix  $(\mathbf{A} + \mathbf{L}\mathbf{U})$  is given by [10]

$$(\mathbf{A} + \mathbf{L}\mathbf{U}) = \hat{\mathbf{K}}_{\text{new}} = \hat{\mathbf{K}}_{\text{old}} + (\mathbf{A}_1\Delta\boldsymbol{\mathcal{E}}\mathbf{A}_1^T + \mathbf{A}_2\Delta\boldsymbol{\mathcal{E}}\mathbf{A}_2^T), \quad (2.63)$$

where  $\Delta\boldsymbol{\mathcal{E}}$  denotes the change in the material distribution. With this, the change of the matrix is given by

$$\gamma\mathbf{L}\mathbf{U} = \gamma(\mathbf{A}_1\Delta\boldsymbol{\mathcal{E}}\mathbf{A}_1^T + \mathbf{A}_2\Delta\boldsymbol{\mathcal{E}}\mathbf{A}_2^T), \quad (2.64)$$

with the scaling variable of the update term  $\gamma$ . This decomposition can be done by the so called LU-decomposition. If only the material value of one finite element is changed,  $\mathbf{L}$  is given by a  $N_{\text{node}} \times 3$  matrix, where  $N_{\text{node}}$

denotes the total number of nodes. The matrix  $\mathbf{L}$  has only entries in the rows  $C$  which correspond to the nodes of the finite element.

By taking use of Green's functions it is possible to replace the inverse  $\mathbf{A}^{-1} = \hat{\mathbf{K}}_{\text{old}}^{-1}$ . According to [18] only the Green's functions of the nodes  $C$  have to be computed. With this the low-rank update is given by [10]

$$\Delta \mathbf{Q} = -\gamma \mathbf{G}_Q^T \mathbf{L} (\mathbf{I} + \gamma \mathbf{U}_{:,C} \mathbf{G}_{C,C} \mathbf{L}_{C,:})^{-1} \mathbf{U} \mathbf{G}_Q. \quad (2.65)$$

$\mathbf{G}_{C,C}$  denotes the Green's functions of the nodes  $C$  which are evaluated by solving (2.47) and  $\mathbf{U}_{:,C}$  and  $\mathbf{L}_{C,:}$  denotes taking only the components which correspond to the nodes  $C$ . Hence the forward map has to be solved for  $C$  identity vectors to obtain  $\mathbf{G}_{C,C}$ . Subsequently the result for an arbitrary scaling of  $\Delta \mathcal{E}$  by the factor  $\gamma$  can be evaluated by inverting the Woodbury matrix once.

## 2.5 Calibration

One important issue with respect to the solution of ill-posed inverse problem is given by model errors as already mentioned in 1.2.1. These errors are caused due to several reasons such as:

- Two dimensional modeling of a three dimensional problem.
- Discretization of the problem domain.
- Simplifications during the derivation of the forward map.
- Not considering the effects of the measurement hardware.
- Further effects, which were not considered.

To minimize the model error given by equation (1.6) calibration strategies has to be introduced.

An often used calibration approach for ECT sensors is given by a Offset-Gain calibration [7] of the form

$$\tilde{\mathbf{d}}_{\text{calib.}} = \mathbf{F}(\boldsymbol{\varepsilon}_{\text{empty}}) + K \left( \tilde{\mathbf{d}} - \tilde{\mathbf{d}}_{\text{empty}} \right), \quad (2.66)$$

with

$$K = \frac{\mathbf{F}(\boldsymbol{\varepsilon}_{\text{full}}) - \mathbf{F}(\boldsymbol{\varepsilon}_{\text{empty}})}{\tilde{\mathbf{d}}_{\text{full}} - \tilde{\mathbf{d}}_{\text{empty}}}. \quad (2.67)$$

Thereby  $\tilde{\mathbf{d}}_{\text{calib.}}$  denotes the calibrated data,  $\mathbf{F}(\boldsymbol{\varepsilon})$  denotes the simulated data by means of the forward map and  $\tilde{\mathbf{d}}$  denotes the real sensor data. The index empty labels the simulation or the measurement for an empty sensor. The index full labels, that the simulation or the measurement was done for a sensor homogeneous filled with a certain material. This material should exhibit a permittivity value in the range of the materials occurring in the measurement process. With this approach a correction of the measurements is performed. In a similar way the output of the simulation model can be calibrated by

$$\mathbf{F}_{\text{calib.}}(\boldsymbol{\varepsilon}) = \tilde{\mathbf{d}}_{\text{empty}} + K (\mathbf{F}(\boldsymbol{\varepsilon}) - \mathbf{F}(\boldsymbol{\varepsilon}_{\text{empty}})), \quad (2.68)$$

with

$$K = \frac{\tilde{\mathbf{d}}_{\text{full}} - \tilde{\mathbf{d}}_{\text{empty}}}{\mathbf{F}(\boldsymbol{\varepsilon}_{\text{full}}) - \mathbf{F}(\boldsymbol{\varepsilon}_{\text{empty}})}. \quad (2.69)$$

Thereby  $\mathbf{F}_{\text{calib.}}(\boldsymbol{\varepsilon})$  denotes the calibrated output of the forward map.

# 3 Reconstruction Algorithms

This chapter outlines the solution of the ill-posed inverse problem of ECT. All reconstruction algorithms presented in this chapter are derived within the Bayesian framework, which is termed Bayesian inversion or statistical inversion theory [9]. With this approach different estimators can be derived, which are suitable for solving the ill-posed inverse problem of ECT. The following reconstruction algorithms are presented in this chapter:

- Linear back projection type algorithms:
  - Sample based back projection algorithms.
  - Linearized MAP and ML type estimator.
- Non-linear iterative methods:
  - Kalman Filter.
  - Gibbs Sampler.

A further topic discussed in this chapter is the concept of state reduction. The estimation task of ECT is typically of high dimension with respect to the quantities of interest. This causes an immanent issue concerning the computational effort for the solution of the problem. Therefore an approach is presented to reduce the dimension of the state space based on principal component analysis [19]. Furthermore it is shown, how to apply this approach to the reconstruction algorithms.

## 3.1 Bayesian Inversion

The Bayesian approach is based on the principle, that all variables are considered to be random variables. These random variables are described by means of probability density functions (pdf)  $\pi$ . With this concept it is possible to connect the measurement data  $\tilde{\mathbf{d}} \in \mathbb{R}^M$  and the state vector  $\mathbf{x} \in \mathbb{R}^N$ . The

data vector  $\tilde{\mathbf{d}}$  is holding the measured inter-electrode capacitances  $C_1 \dots C_M$  and the state vector  $\mathbf{x}$  is holding the quantities of interest, which in this case are the material values of the finite elements  $\varepsilon_{r,1} \dots \varepsilon_{r,N}$ . Bayes law is given by

$$\pi(\mathbf{x}|\tilde{\mathbf{d}}) = \frac{\pi(\tilde{\mathbf{d}}|\mathbf{x})\pi(\mathbf{x})}{\pi(\tilde{\mathbf{d}})} \propto \pi(\tilde{\mathbf{d}}|\mathbf{x})\pi(\mathbf{x}). \quad (3.1)$$

The pdfs  $\pi(\mathbf{x}|\tilde{\mathbf{d}})$ ,  $\pi(\tilde{\mathbf{d}}|\mathbf{x})$  and  $\pi(\mathbf{x})$  are referred to as posterior distribution, likelihood function and prior distribution, respectively. The posterior distribution  $\pi(\mathbf{x}|\tilde{\mathbf{d}})$  provides a probability measure for the state vector  $\mathbf{x}$ , given the measurement data  $\tilde{\mathbf{d}}$ .

To construct the posterior pdf the so called likelihood function  $\pi(\tilde{\mathbf{d}}|\mathbf{x})$  is necessary, which is a pdf for the measurement data  $\tilde{\mathbf{d}}$  given the state vector  $\mathbf{x}$ . It is assumed, that the measurements are corrupted by additive measurement noise

$$\tilde{\mathbf{d}} = \mathbf{d} + \mathbf{v}. \quad (3.2)$$

Hereby  $\mathbf{d} \in \mathbb{R}^M$  denotes the noise free measurement data and  $\mathbf{v} \in \mathbb{R}^M$  is a multivariate random variable representing the measurement noise with the pdf  $\pi_{\mathbf{v}}(\mathbf{v})$ . Given this noise model, the likelihood function is formulated by [20]

$$\pi(\tilde{\mathbf{d}}|\mathbf{x}) = \pi_{\mathbf{v}}(\mathbf{F}(\mathbf{x}) - \tilde{\mathbf{d}}). \quad (3.3)$$

$\mathbf{F}(\mathbf{x})$  is the forward map of the ECT sensor presented in chapter 2, which simulates the noise free measurement process. For Gaussian distributed noise  $\mathbf{v} \propto \mathcal{N}(\mathbf{0}, \Sigma_{\mathbf{v}})$ , with zero mean and the covariance matrix  $\Sigma_{\mathbf{v}}$ , the likelihood function is given by

$$\pi(\tilde{\mathbf{d}}|\mathbf{x}) = \frac{1}{(2\pi)^{\frac{M}{2}} |\Sigma_{\mathbf{v}}|^{-1}} \exp\left(-\frac{1}{2} (\mathbf{F}(\mathbf{x}) - \tilde{\mathbf{d}})^T \Sigma_{\mathbf{v}}^{-1} (\mathbf{F}(\mathbf{x}) - \tilde{\mathbf{d}})\right). \quad (3.4)$$

The aim is the solution of the ill-posed inverse problem of ECT. Hence prior information about the state vector  $\mathbf{x}$  is required to obtain stable estimation results. This prior information is incorporated by means of the prior distribution  $\pi(\mathbf{x})$ , which is a pdf for the material distribution within the ECT sensor. As it is hard to find a meaningful mathematical formulation for the prior information, one possible approach is that  $\pi(\mathbf{x})$  is also of Gaussian type. Given the mean  $\boldsymbol{\mu}_{\mathbf{x}}$  and the covariance matrix  $\Sigma_{\mathbf{x}}$  for the random variable  $\mathbf{x}$ ,

it is assumed that  $\pi(\mathbf{x}) \propto \mathcal{N}(\boldsymbol{\mu}_{\mathbf{x}}, \boldsymbol{\Sigma}_{\mathbf{x}})$  holds. With this the prior distribution is formulated by

$$\pi(\mathbf{x}) = \frac{1}{(2\pi)^{\frac{N}{2}} |\boldsymbol{\Sigma}_{\mathbf{x}}|^{-1}} \exp\left(-\frac{1}{2}(\mathbf{x} - \boldsymbol{\mu}_{\mathbf{x}})^T \boldsymbol{\Sigma}_{\mathbf{x}}^{-1}(\mathbf{x} - \boldsymbol{\mu}_{\mathbf{x}})\right). \quad (3.5)$$

Detailed information on how to find meaningful values for  $\boldsymbol{\mu}_{\mathbf{x}}$  and  $\boldsymbol{\Sigma}_{\mathbf{x}}$  by means of a sample based approach can be found in the later section 3.2. Another possible approach is given by

$$\pi(\mathbf{x}) = \exp\left(\alpha \|\mathbf{L}\mathbf{x}\|_2^2\right), \quad (3.6)$$

where  $\mathbf{L}$  is referred to as regularization matrix and  $\alpha$  is an additional regularization parameter. One common prior in ECT is to assume a smooth material distribution. In this case the regularization matrix  $\mathbf{L}$  is chosen to be a discrete version of the Laplace operator [7].

## 3.2 Sample based Prior and Gaussian Summary Statistics

One important issue with respect to ill-posed inverse problem is the incorporation of meaningful prior information to the reconstruction algorithms. In the particular case of ECT the patterns of the material distributions are often well known, though finding a meaningful mathematical formulation for the prior information is difficult. Therefore the approach of sample based prior is presented in this section. Hereby a set of random samples is generated, suitable to describe the occurring material pattern within the ECT sensor. Subsequently a Gaussian summary statistic given by equation (3.5) is calculated for this set of random samples. This Gaussian prior distribution  $\pi(\mathbf{x})$  is afterwards incorporated to the Bayesian reconstruction algorithms presented in the later sections 3.4 and 3.5.

### 3.2.1 Generation of Random Samples

For arbitrary material distribution two different sample generators are presented, namely one for rod type samples and one for Gaussian type samples [7]. Figure 3.1 depict exemplary random samples for both types of patterns. For the generation of the samples, firstly a number of inclusions  $\#_{\text{incl}}$  within the ECT sensor is randomly selected. In the next step the material value  $\varepsilon_r$ , the center point  $[\mu_x, \mu_y]$  and the radius  $r$  for rod type samples

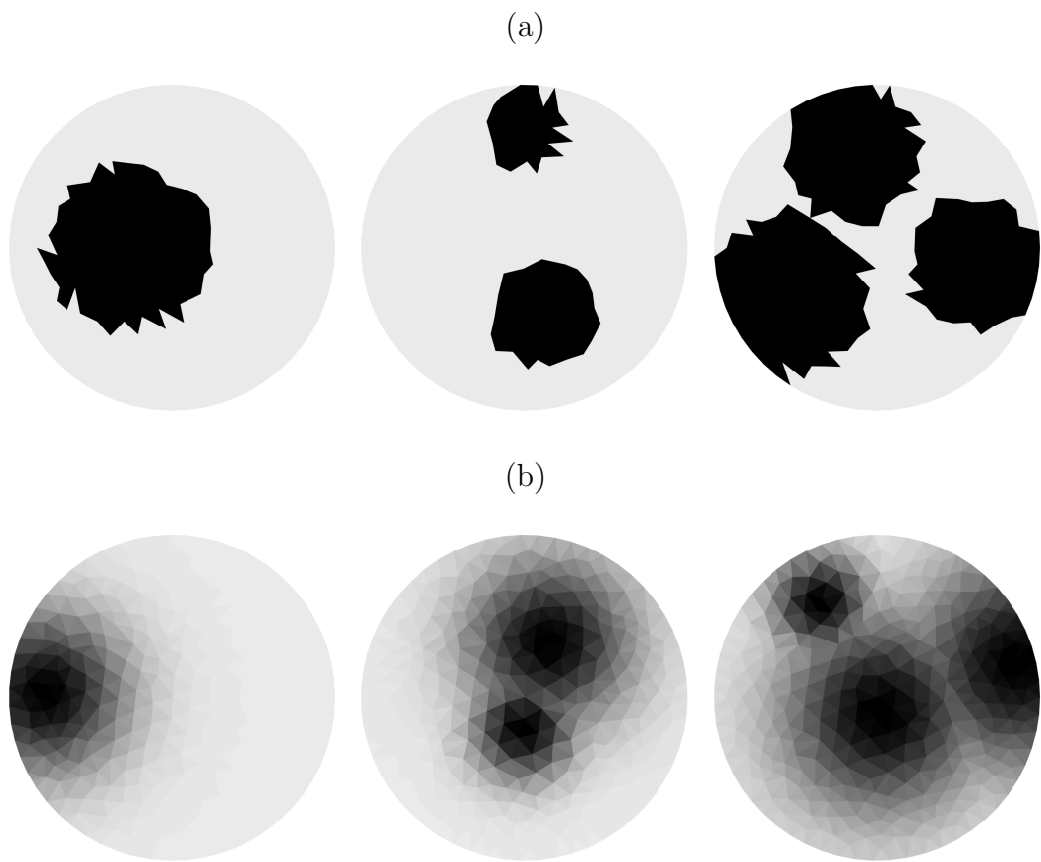


**Figure 3.1:** Exemplary rod (a) and Gaussian (b) type random samples.

or the standard deviation  $\sigma$  for Gaussian type samples of each inclusion is randomly selected. Finally the inclusions given by this random parameters are mapped onto the finite element mesh. For rod type samples the mapping is done by setting the material values of the finite elements within the domain with the center point  $[\mu_x, \mu_y]$  and the radius  $r$  to the material value  $\varepsilon_r$ . For Gaussian type samples the mapping is done by

$$x_i = 1 + (\varepsilon_r - 1) \exp\left(\frac{(\mu_{\text{FE},x,i} - \mu_x)^2 + (\mu_{\text{FE},y,i} - \mu_y)^2}{\sigma^2}\right). \quad (3.7)$$

$[\mu_{\text{FE},x,i}, \mu_{\text{FE},y,i}]$  denotes the center point of the  $i^{\text{th}}$  finite element and  $x_i$  is the corresponding element of the resulting state vector  $\mathbf{x}$ . With this the state vector  $\mathbf{x}$  of the random sample is given by a vector holding the elements  $x_i$  for  $i = 1 \dots N$ . A pseudo code for both pattern generators is given by algorithm 3.1 [7].

---

**Algorithm 3.1** Algorithm to obtain random samples for arbitrary material patterns.

---

- 1: Draw  $\#\text{incl} \propto \mathcal{U}(1, \#\text{incl,max})$
  - 2: **for**  $i = 1$  to  $\#\text{incl}$
  - 3:     Draw  $[\mu_x, \mu_y] \propto \mathcal{U}(\text{in ROI})$
  - 4:     Draw  $\varepsilon_r \propto \mathcal{U}(\varepsilon_{r,\text{min}}, \varepsilon_{r,\text{max}})$
  - 5:     Draw  $r \propto \mathcal{U}(r_{\text{min}}, r_{\text{max}})$  or  $\sigma \propto \mathcal{U}(\sigma_{\text{min}}, \sigma_{\text{max}})$
  - 6:     Create the inclusion out of the parameters
  - 7: **end**
  - 8: Map the inclusions onto the finite element mesh  $\rightarrow \mathbf{x}$
- 

### 3.2.2 Gaussian Summary Statistics

Given the approach for the generation of random samples, a method is required to incorporate the information held by these samples to the reconstruction algorithms. Therefore a Gaussian summary statistic  $\pi(\mathbf{x}) \propto \mathcal{N}(\boldsymbol{\mu}_{\mathbf{x}}, \boldsymbol{\Sigma}_{\mathbf{x}})$  given by equation (3.5) is computed to formulate a prior pdf. This pdf is parametrized by the mean  $\boldsymbol{\mu}_{\mathbf{x}}$  and the covariance matrix  $\boldsymbol{\Sigma}_{\mathbf{x}}$ .

To obtain  $\boldsymbol{\mu}_{\mathbf{x}}$  and  $\boldsymbol{\Sigma}_{\mathbf{x}}$ , a number of  $N_{\text{sample}}$  random samples is stored in the  $N \times N_{\text{samples}}$  matrix  $\mathbf{X}$ , where each column represents one sample. Each row  $i$  can be seen as a row vector holding realizations  $x_{ij}$  of the random variable  $X_i$ . The mean  $\boldsymbol{\mu}_{\mathbf{x}}$  is given by a column vector holding the means of

each row of  $\mathbf{X}$

$$\mu_{X_i} = \mathcal{E} \{X_i\} = \frac{1}{N_{\text{sample}}} \sum_{j=1}^{N_{\text{sample}}} x_{ij}. \quad (3.8)$$

The  $N \times N$  covariance matrix is given by

$$\Sigma_{\mathbf{X}} = \mathcal{E} \left\{ (\mathbf{X} - \boldsymbol{\mu}_{\mathbf{X}}) (\mathbf{X} - \boldsymbol{\mu}_{\mathbf{X}})^T \right\} \quad (3.9)$$

$$= \mathcal{E} \left\{ \begin{array}{ccc} (X_1 - \mu_{X_1})^2 & \dots & (X_1 - \mu_{X_1})(X_N - \mu_{X_N}) \\ \vdots & \ddots & \vdots \\ (X_N - \mu_{X_N})(X_1 - \mu_{X_1}) & \dots & (X_N - \mu_{X_N})^2 \end{array} \right\}. \quad (3.10)$$

With this, the Gaussian prior  $\pi(\mathbf{x})$  is fully parametrized.

### 3.3 Prior Based State Reduction

In this section the approach for a reduced state representation based on prior information is presented. This concept is given by the approximation of the original state vector  $\mathbf{x} \in \mathbb{R}^N$  by a reduced state vector  $\mathbf{x}_R \in \mathbb{R}^{N_R}$ , where  $N_R < N$  holds [19]. To describe the relation between the full state vector  $\mathbf{x}$  and the reduced state vector  $\mathbf{x}_R$  the so called projection matrix  $\mathbf{P}_{N_R}$  is introduced. The projection is given by

$$\mathbf{x} = \mathbf{P}_{N_R} \mathbf{x}_R. \quad (3.11)$$

$\mathbf{P}_{N_R}$  maps the reduced state space into the full state space  $\mathbf{P}_{N_R} : \mathbf{x}_R \mapsto \mathbf{x}$ . The basis vectors of the reduced state representation are given by the columns of  $\mathbf{P}_{N_R}$ . One way to construct those basis vectors is a principle component analysis (PCA) of a set of random samples from the prior distribution  $\pi(\mathbf{x})$ . Therefore a  $N \times N_{\text{samples}}$  matrix  $\mathbf{X}$  is assembled where the  $N_{\text{samples}}$  columns are given by random samples from the prior distribution  $\pi(\mathbf{x})$ . In the next step a singular value decomposition of  $\mathbf{X}$  is performed given by

$$\mathbf{U} \boldsymbol{\Sigma} \mathbf{V}^T = \mathbf{X}. \quad (3.12)$$

The columns  $\mathbf{u}_i$  of the unitary  $N \times N$  matrix  $\mathbf{U}$  can now be used to construct the projection matrix  $\mathbf{P}_{N_R}$ . The matrix  $\boldsymbol{\Sigma}$  is a diagonal matrix holding the singular values of  $\mathbf{X}$ . The singular values are decreasing with the index  $i$  [19]. They can be seen as an importance weight for the basis vectors  $\mathbf{u}_i$ . This property can be used to assemble the projection matrix  $\mathbf{P}_{N_R}$  by

$$\mathbf{P}_{N_R} = [\mathbf{1} \quad \mathbf{u}_1 \quad \mathbf{u}_2 \quad \dots \quad \mathbf{u}_{N_R-1}]. \quad (3.13)$$

The vector  $\mathbf{1}$  forming the first column of  $\mathbf{P}_{N_R}$  is required to present constant parts of the material distribution. With only the first  $N_R - 1$  column vectors of  $\mathbf{U}$  the essential components of the material distribution within the ECT sensor can be reproduced. This is possible due to the circumstance, that the importance of the vectors  $\mathbf{u}_i$  is decreasing with the index  $i$ . Because the vectors  $\mathbf{u}_i$  for  $i > N_R - 1$  are skipped the estimation result for a reduced state representation exhibit a self regulating behaviour against noisy measurements and model errors.

Given the matrix  $\mathbf{P}_{N_R}$  the reduced state vector  $\mathbf{x}_R$  can be calculated in a least squares sense

$$\hat{\mathbf{x}}_{R,1} = (\mathbf{P}_{N_R}^T \mathbf{P}_{N_R}) \mathbf{P}_{N_R}^T \mathbf{x}, \quad (3.14)$$

as equation (3.11) forms an overdetermined equation system [19]. To incorporate constraints to the state vector  $\mathbf{x}$  the reduced state vector  $\mathbf{x}_R$  can also be determined by means of a constrained least squares approximation given by

$$\begin{aligned} \hat{\mathbf{x}}_{R,2} = \arg \min_{\mathbf{x}_R} \|\mathbf{P}_{N_R} \mathbf{x}_R - \mathbf{x}\|_2^2 \\ \text{s.t } \mathbf{x}_{\min} \leq \mathbf{P}_{N_R} \mathbf{x}_R \leq \mathbf{x}_{\max}. \end{aligned} \quad (3.15)$$

Hereby  $\mathbf{x}_{\min}$  denotes the lower constraint and  $\mathbf{x}_{\max}$  denotes the upper constraint of the state vector  $\mathbf{x}$ .

### 3.4 Linear Back Projection Type Algorithms

In this section linear, non-iterative back projection (BP) type reconstruction methods are presented. These algorithms are given by a simple matrix vector multiplication of the form

$$\hat{\mathbf{x}} = \mathbf{P} \tilde{\mathbf{d}}, \quad (3.16)$$

where  $\hat{\mathbf{x}}$  denotes the estimated state vector and  $\tilde{\mathbf{d}}$  denotes a vector holding the measurement data.  $\mathbf{P}$  is referred to as reconstruction matrix.

There are different principles for the derivation of  $\mathbf{P}$  [20]. The first algorithm considered in this section uses a sample based technique for the construction of  $\mathbf{P}$ , termed optimal approximation (OA) [21].

The second BP type algorithm provided here is constructed by means of the posterior distribution  $\pi(\mathbf{x}|\tilde{\mathbf{d}})$  and a linear approximation of the forward map  $\mathbf{F}(\mathbf{x})$ , leading to the so called linearised maximum a posteriori (MAP) estimator.

### 3.4.1 Sample based Back Projection Algorithms

In this subsection a sample based BP type reconstruction of form (3.16) is discussed. In particular the so called optimal first order approximation (OFOA) and the optimal second order approximation (OSOA) techniques [21]. After the derivation of those algorithms the application of the sample based state reduction approach presented in 3.3 is discussed.

The concept of the methods termed optimal approximation is the incorporation of explicit prior knowledge in the construction of the matrix  $\mathbf{P}$ . This is done in a way that the expectation of the error between the reconstructed material distribution and the real material distribution becomes a minimum in a quadratic sense. Therefore an optimization problem is formulated given by

$$\mathbf{P}^* = \arg \min_{\mathbf{P}} \mathcal{E} \left\{ \|\mathbf{P}\tilde{\mathbf{d}}_a - \mathbf{x}\|_2^2 \right\} \quad (3.17)$$

$$\text{s.t. } \pi(\mathbf{x}), \quad (3.18)$$

where  $\tilde{\mathbf{d}}_a$  denotes an augmented data vector. In the following paragraphs the assembly of the single components of equation (3.17) as well as the incorporation of the state reduction approach is discussed.

#### Augmented Data Vector $\tilde{\mathbf{d}}_a$

In the first step the construction of the augmented data vector  $\tilde{\mathbf{d}}_a$  is discussed. In both cases (OFOA and OSOA) the vector contains the measured capacitances. The vectors are given by

$$\tilde{\mathbf{d}}_{\text{OFOA}} = [1 \ C_1 \ C_2 \ \dots \ C_M]^T, \quad (3.19)$$

$$\tilde{\mathbf{d}}_{\text{OSOA}} = [1 \ C_1 \ C_2 \ \dots \ C_N \ C_1^2 \ C_2^2 \ \dots \ C_M^2]^T, \quad (3.20)$$

where  $\tilde{\mathbf{d}}_{\text{OFOA}}$  and  $\tilde{\mathbf{d}}_{\text{OSOA}}$  denote the augmented data vector for the OFOA algorithm and the OSOA algorithm respectively.  $C_1 \dots C_N$  are the measured inter-electrode capacitances.

#### Reconstruction Matrix $\mathbf{P}$

The second step concerns the assembly of the reconstruction matrix  $\mathbf{P}$  by means of the approach given by equation (3.17). It is possible to generate samples  $\mathbf{x}$  from a meaningful prior distribution  $\pi(\mathbf{x})$  like discussed in section

3.2. Given a set of random samples from  $\pi(\mathbf{x})$ , the approach (3.17) can be formulated as a least squares problem of the form

$$\tilde{\mathbf{D}}_a \mathbf{P}^T = \mathbf{X}. \quad (3.21)$$

The rows of  $\mathbf{X}$  and  $\tilde{\mathbf{D}}_a$  are given by the samples  $\mathbf{x}_i^T$  from the prior distribution  $\pi(\mathbf{x})$  and the corresponding augmented data vectors  $\tilde{\mathbf{d}}_a^T$  respectively. The solution of this least squares problem is given by

$$\mathbf{P}^T = \left( \tilde{\mathbf{D}}_a^T \tilde{\mathbf{D}}_a \right)^{-1} \tilde{\mathbf{D}}_a^T \mathbf{X}. \quad (3.22)$$

The incorporation of prior knowledge about the measurement noise can be done by taking multiple use of the sample  $\mathbf{x}_i$  in  $\mathbf{X}$  and using different noisy realizations of  $\tilde{\mathbf{d}}_a$  in  $\tilde{\mathbf{D}}_a$ .

### Incorporation of the State Reduction Technique

To apply the state reduction technique presented in section 3.3, equation (3.21) has to be solved for  $\mathbf{X}_R$ , resulting in the reconstruction matrix  $\mathbf{P}_R$  [19]

$$\mathbf{P}_R^T = \left( \tilde{\mathbf{D}}_a^T \tilde{\mathbf{D}}_a \right)^{-1} \tilde{\mathbf{D}}_a^T \mathbf{X}_R. \quad (3.23)$$

The rows of  $\mathbf{X}_R$  are now given by the reduced representations  $\mathbf{x}_{R,i}^T$  of the samples. This reduced state vectors can be computed with the estimator given in equation (3.14) or (3.15) if the incorporation of state constraints is required. The reduced reconstruction matrix  $\mathbf{P}_R$  describes the relation between the measurements and the reduced state vector  $\mathbf{x}_R$ . To obtain the full state vector the projection matrix  $\mathbf{P}_{N_R}$  given by equation (3.13) has to be incorporated. The reconstruction matrix  $\mathbf{P}$ , describing the linear relation between the measurement and the full state vector  $\mathbf{x}$  is given by

$$\mathbf{P} = \mathbf{P}_{N_R} \mathbf{P}_R. \quad (3.24)$$

### 3.4.2 Linearised MAP and ML type Estimator

The MAP estimator is defined by maximizing the posterior distribution given by equation (3.1) [22]. Instead of maximizing  $\pi(\mathbf{x}|\tilde{\mathbf{d}})$  it is also possible to maximize the logarithm of the posterior distribution  $\ln(\pi(\mathbf{x}|\tilde{\mathbf{d}}))$ . This provides a more simple representation of the problem due to the exponential form of Gaussian distributions. Hence the MAP estimator can be formulated by

$$\hat{\mathbf{x}} = \arg \max_{\mathbf{x}} \ln \left( \pi \left( \mathbf{x} | \tilde{\mathbf{d}} \right) \pi(\mathbf{x}) \right). \quad (3.25)$$

Using the relations for the likelihood function (3.4) and the prior distribution (3.5) and skipping all terms, which do not depend on the optimization variables  $\mathbf{x}$  leads to the relation

$$\hat{\mathbf{x}} = \arg \min_{\mathbf{x}} \left( \mathbf{F}(\mathbf{x}) - \tilde{\mathbf{d}} \right)^T \Sigma_{\mathbf{V}}^{-1} \left( \mathbf{F}(\mathbf{x}) - \tilde{\mathbf{d}} \right) + (\mathbf{x} - \boldsymbol{\mu}_{\mathbf{X}})^T \Sigma_{\mathbf{X}}^{-1} (\mathbf{x} - \boldsymbol{\mu}_{\mathbf{X}}). \quad (3.26)$$

This forms a nonlinear optimization problem as the forward map  $\mathbf{F}(\mathbf{x})$  of the ECT sensor is of nonlinear nature. Since the aim is the derivation of a linear BP type estimator a linear Taylor-Series approximation

$$\mathbf{F}(\mathbf{x}_0 + \Delta \mathbf{x}) \approx \mathbf{F}(\mathbf{x}_0) + \mathbf{J}(\mathbf{x}_0) \Delta \mathbf{x}, \quad (3.27)$$

is applied to the forward map. Thereby  $\mathbf{x}_0$  is referred to as linearisation point and  $\mathbf{J}(\mathbf{x}_0)$  denotes the Jacobian in this point given by

$$\mathbf{J}(\mathbf{x}_0) = [J_{i,j}(\mathbf{x}_0)] = \left[ \left. \frac{\partial C_i}{\partial x_j} \right|_{\mathbf{x}_0} \right]. \quad (3.28)$$

With this the linearized MAP estimator becomes

$$\Delta \hat{\mathbf{x}} = \arg \min_{\Delta \mathbf{x}} \left( \mathbf{F}(\mathbf{x}_0) + \mathbf{J} \Delta \mathbf{x} - \tilde{\mathbf{d}} \right)^T \Sigma_{\mathbf{V}}^{-1} \left( \mathbf{F}(\mathbf{x}_0) + \mathbf{J} \Delta \mathbf{x} - \tilde{\mathbf{d}} \right) + (\mathbf{x}_0 + \Delta \mathbf{x} - \boldsymbol{\mu}_{\mathbf{X}})^T \Sigma_{\mathbf{X}}^{-1} (\mathbf{x}_0 + \Delta \mathbf{x} - \boldsymbol{\mu}_{\mathbf{X}}). \quad (3.29)$$

The estimation result is now the change in the material values  $\Delta \hat{\mathbf{x}}$  with respect to the linearisation point  $\mathbf{x}_0$ . An obvious choice for the linearisation point is the mean of the prior distribution  $\mathbf{x}_0 = \boldsymbol{\mu}_{\mathbf{X}}$ . Due to the linearisation it is possible to derive an analytical solution for this unconstrained optimization problem given by

$$\hat{\mathbf{x}} = \boldsymbol{\mu}_{\mathbf{X}} + \left( \mathbf{J}^T \Sigma_{\mathbf{V}}^{-1} \mathbf{J} + \Sigma_{\mathbf{X}}^{-1} \right)^{-1} \left( \mathbf{J}^T \Sigma_{\mathbf{V}}^{-1} \left( \tilde{\mathbf{d}} - \mathbf{F}(\boldsymbol{\mu}_{\mathbf{X}}) \right) \right). \quad (3.30)$$

To incorporate state constraints the optimization problem (3.29) has to be solved with subject to  $\mathbf{x}_{\min} \leq \mathbf{x} \leq \mathbf{x}_{\max}$ . Due to the fact that  $\mathbf{F}(\boldsymbol{\mu}_{\mathbf{X}})$  and  $\tilde{\mathbf{d}}$  are constant the problem can be written as

$$\Delta \hat{\mathbf{x}} = \arg \min_{\Delta \mathbf{x}} \Delta \mathbf{x}^T \left( \mathbf{J}^T \Sigma_{\mathbf{V}}^{-1} \mathbf{J} + \Sigma_{\mathbf{X}}^{-1} \right) \Delta \mathbf{x} - 2 \left( \tilde{\mathbf{d}} - \mathbf{F}(\boldsymbol{\mu}_{\mathbf{X}}) \right)^T \Sigma_{\mathbf{V}}^{-1} \mathbf{J} \Delta \mathbf{x} \quad (3.31)$$

$$\text{s.t. } \mathbf{x}_{\min} - \boldsymbol{\mu}_{\mathbf{X}} \leq \Delta \mathbf{x} \leq \mathbf{x}_{\max} - \boldsymbol{\mu}_{\mathbf{X}},$$

which is a simple quadratic programming problem. As the estimation result is again the change of the material values  $\Delta \hat{\mathbf{x}}$  with respect to the linearisation point  $\boldsymbol{\mu}_{\mathbf{X}}$ , the material values are given by

$$\hat{\mathbf{x}} = \boldsymbol{\mu}_{\mathbf{X}} + \Delta \hat{\mathbf{x}}. \quad (3.32)$$

### Incorporation of the State Reduction Technique

To incorporate the state reduction approach presented in section 3.3 to the linearised MAP estimator, equation (3.29) has to be considered. Replacing  $\Delta \mathbf{x}$  with  $\mathbf{P}_{N_R} \Delta \mathbf{x}_R$  and performing the same derivation steps as before leads to [20]

$$\hat{\mathbf{x}} = \boldsymbol{\mu}_{\mathbf{X}} + \mathbf{P}_{N_R} \left( \mathbf{P}_{N_R}^T \mathbf{J} \boldsymbol{\Sigma}_{\mathbf{V}}^{-1} \mathbf{J} \mathbf{P}_{N_R} + \mathbf{P}_{N_R}^T \boldsymbol{\Sigma}_{\mathbf{X}}^{-1} \mathbf{P}_{N_R} \right)^{-1} \cdot \left( \mathbf{P}_{N_R}^T \mathbf{J}^T \boldsymbol{\Sigma}_{\mathbf{V}}^{-1} \left( \tilde{\mathbf{d}} - \mathbf{F}(\boldsymbol{\mu}_{\mathbf{X}}) \right) \right). \quad (3.33)$$

The incorporation of state constraints leads again to a quadratic programming problem of the form

$$\begin{aligned} \Delta \hat{\mathbf{x}}_R = \arg \min_{\Delta \mathbf{x}_R} & \Delta \mathbf{x}_R^T \left( \mathbf{P}_{N_R}^T \mathbf{J}^T \boldsymbol{\Sigma}_{\mathbf{V}}^{-1} \mathbf{J} \mathbf{P}_{N_R} + \mathbf{P}_{N_R}^T \boldsymbol{\Sigma}_{\mathbf{X}}^{-1} \mathbf{P}_{N_R} \right) \Delta \mathbf{x}_R \\ & - 2 \left( \tilde{\mathbf{d}} - \mathbf{F}(\boldsymbol{\mu}_{\mathbf{X}}) \right)^T \boldsymbol{\Sigma}_{\mathbf{V}}^{-1} \mathbf{J} \mathbf{P}_{N_R} \Delta \mathbf{x}_R \\ \text{s.t. } & \mathbf{x}_{\min} - \boldsymbol{\mu}_{\mathbf{X}} \leq \mathbf{P}_{N_R} \Delta \mathbf{x}_R \leq \mathbf{x}_{\max} - \boldsymbol{\mu}_{\mathbf{X}}. \end{aligned} \quad (3.34)$$

Since the estimation result is the change of the reduced state vector  $\Delta \hat{\mathbf{x}}_R$  with respect to the linearisation point  $\boldsymbol{\mu}_{\mathbf{X}}$ , the full state vector is given by

$$\hat{\mathbf{x}} = \boldsymbol{\mu}_{\mathbf{X}} + \mathbf{P}_{N_R} \Delta \hat{\mathbf{x}}_R. \quad (3.35)$$

### Linearized ML Type Estimator for a Reduced State Representation

If the state reduction technique is applied to the estimation task, the size of the state vector is reduced from the original size  $N$  to  $N_R$ . Since the projection matrix  $\mathbf{P}_{N_R}$  is assembled from random samples of the prior distribution  $\pi(\mathbf{x})$ , the state reduction approach is an alternative way for incorporating prior information. By choosing the size of the reduced state space to be  $N_R < M$ , it is possible to set the prior distribution to

$$\pi(\mathbf{x}) = 1. \quad (3.36)$$

Given this approach the estimation problem can be formulated as

$$\hat{\mathbf{x}}_R = \arg \max_{\mathbf{x}_R} \ln \left( \pi \left( \mathbf{P}_{N_R} \mathbf{x}_R | \tilde{\mathbf{d}} \right) \right). \quad (3.37)$$

Estimators given by maximizing the likelihood function are usually referred to as maximum likelihood (ML) estimators. Due to the incorporation of

prior information by means of  $\mathbf{P}_{N_R}$  the resulting algorithm will be termed ML type estimator. Doing the same derivation steps as before leads to

$$\Delta \hat{\mathbf{x}}_R = \arg \min_{\Delta \mathbf{x}_R} \left( \mathbf{F}(\boldsymbol{\mu}_{\mathbf{X}}) + \mathbf{J}\mathbf{P}_{N_R}\Delta \mathbf{x}_R - \tilde{\mathbf{d}} \right)^T \boldsymbol{\Sigma}_{\mathbf{V}}^{-1} \cdot \left( \mathbf{F}(\boldsymbol{\mu}_{\mathbf{X}}) + \mathbf{J}\mathbf{P}_{N_R}\Delta \mathbf{x}_R - \tilde{\mathbf{d}} \right). \quad (3.38)$$

Again the linearisation point is chosen to be  $\mathbf{x}_0 = \boldsymbol{\mu}_{\mathbf{X}}$ . The analytic result for this linear ML type estimator is given by

$$\hat{\mathbf{x}} = \boldsymbol{\mu}_{\mathbf{X}} + \mathbf{P}_{N_R} \left( \mathbf{P}_{N_R}^T \mathbf{J}^T \boldsymbol{\Sigma}_{\mathbf{V}}^{-1} \mathbf{J} \mathbf{P}_{N_R} \right)^{-1} \mathbf{P}_{N_R}^T \mathbf{J}^T \boldsymbol{\Sigma}_{\mathbf{V}}^{-1} \left( \tilde{\mathbf{d}} - \mathbf{F}(\boldsymbol{\mu}_{\mathbf{X}}) \right). \quad (3.39)$$

For the incorporation of state constraints, the problem can again be formulated as a simple quadratic programming problem given by

$$\begin{aligned} \Delta \hat{\mathbf{x}}_R = \arg \min_{\Delta \mathbf{x}_R} & \Delta \mathbf{x}_R^T \mathbf{P}_{N_R}^T \mathbf{J}^T \boldsymbol{\Sigma}_{\mathbf{V}}^{-1} \mathbf{J} \mathbf{P}_{N_R} \Delta \mathbf{x}_R \\ & - 2 \left( \tilde{\mathbf{d}} - \mathbf{F}(\boldsymbol{\mu}_{\mathbf{X}}) \right)^T \boldsymbol{\Sigma}_{\mathbf{V}}^{-1} \mathbf{J} \mathbf{P}_{N_R} \Delta \mathbf{x}_R \\ \text{s.t. } & \mathbf{x}_{\min} - \boldsymbol{\mu}_{\mathbf{X}} \leq \mathbf{P}_{N_R} \Delta \mathbf{x}_R \leq \mathbf{x}_{\max} - \boldsymbol{\mu}_{\mathbf{X}}. \end{aligned} \quad (3.40)$$

The full state vector  $\hat{\mathbf{x}}$  is again obtained with the relation given by equation (3.35).

## 3.5 Non-linear Iterative Methods

In this section two iterative methods are presented, which are able to deal with the non-linear forward map of the ECT sensor. The first algorithm considered, is the so called Kalman Filter, which belongs to the class of recursive Bayesian algorithms. The second algorithm presented in this section is the Gibbs Sampler, which is a Markov Chain Monte Carlo sampling method.

### 3.5.1 Kalman Filter

The Kalman Filter belongs to the class of recursive Bayesian algorithms [23]. The Kalman Filter was usually thought of as an estimator for a signal embedded in noise, which is represented by means of a linear discrete time state space model [22]

$$\mathbf{x}_{k+1} = \boldsymbol{\Phi}_k \mathbf{x}_k + \mathbf{w}_k, \quad (3.41)$$

$$\mathbf{y}_k = \mathbf{H}_k \mathbf{x}_k + \mathbf{v}_k. \quad (3.42)$$

Hereby the system matrix  $\Phi_k$  describes the dynamic evolution of the state vector  $\mathbf{x}_k \in \mathbb{R}^N$ . The variable  $\mathbf{w}_k \in \mathbb{R}^N$  is referred to as process noise and forms a random input for the system. Equation (3.42) is termed measurement equation. It describes the dependence of the measurement vector  $\mathbf{y}_k \in \mathbb{R}^M$  on the current state vector  $\mathbf{x}_k$  by means of the matrix  $\mathbf{H}_k$ . The measurement vector  $\mathbf{y}_k$  is corrupted by additive measurement noise  $\mathbf{v}_k \in \mathbb{R}^M$ . The Kalman Filter is a recursive filter scheme that provides an estimator  $\hat{\mathbf{x}}$  for the state vector in such a way that

$$\arg \min_{\hat{\mathbf{x}}} \mathcal{E} \left( (\mathbf{x} - \hat{\mathbf{x}})^2 \right), \quad (3.43)$$

holds [24]. The filter equations are given by

$$\mathbf{x}_k^* = \Phi_k \hat{\mathbf{x}}_{k-1}, \quad (3.44)$$

$$\mathbf{P}_k^* = \Phi_k \mathbf{P}_{k-1} \Phi_k^T + \mathbf{Q}_k, \quad (3.45)$$

$$\mathbf{K}_k = \mathbf{P}_k^* \mathbf{H}_k^T (\mathbf{H}_k \mathbf{P}_k^* \mathbf{H}_k^T + \mathbf{R}_k)^{-1}, \quad (3.46)$$

$$\hat{\mathbf{x}}_k = \mathbf{x}_k^* + \mathbf{K}_k (\mathbf{y}_k - \mathbf{H}_k \mathbf{x}_k^*), \quad (3.47)$$

$$\mathbf{P}_k = (\mathbf{I} - \mathbf{K}_k \mathbf{H}_k) \mathbf{P}_k^*. \quad (3.48)$$

It is assumed, that the process- and the measurement noise as well as the state vector are Gaussian distributed random variables. This means, that the variables can be described by a mean and a covariance matrix. For the noise processes  $\mathbf{v}_k$  and  $\mathbf{w}_k$  zero mean is assumed. With this assumption the noise processes are fully described by their covariance matrices. They are given by the covariance matrix  $\mathbf{R}_k$  for the measurement noise and the covariance matrix  $\mathbf{Q}_k$  of the process noise.

In the first two Kalman Filter equations (3.44) and (3.45) the predicted state is calculated, where  $\mathbf{x}_k^*$  denotes the mean and  $\mathbf{P}_k^*$  the covariance matrix of the prediction. The state vector  $\hat{\mathbf{x}}_k$  in equation (3.47) is the mean of the final estimation result. The matrix  $\mathbf{P}_k$  in equation (3.48) denotes the covariance matrix, which provides information about the quality of the estimation result.

Although the Kalman Filter was designed for the task of state estimation in dynamic systems of the form (3.41) and (3.42), it can also be used to solve the ill-posed inverse Problem of ECT. However some adaptations of the original Kalman Filter equations are necessary to deal with the non-linearity and the ill-posed nature of ECT.

### Adaptations for the Incorporation of the Regularization Matrix $\mathbf{L}$

One possible way to apply the Kalman Filter to the non-linear ill-posed inverse problem of ECT is the incorporation of a regularization matrix  $\mathbf{L}$  to obtain stable solutions [25]. To do so, a few adaptations of the Kalman Filter equations are necessary.

In the first step the measurement vector is augmented by

$$\mathbf{y}_k = \begin{bmatrix} \tilde{\mathbf{d}} \\ \mathbf{0} \end{bmatrix}, \quad (3.49)$$

where  $\tilde{\mathbf{d}} \in \mathbb{R}^M$  is a vector holding the inter-electrode capacitances of the ECT sensor. Given this measurement vector  $\mathbf{y}_k$ , also the measurement equation has to be adapted by

$$\mathbf{H}_k = \begin{bmatrix} \mathbf{J}_k(\mathbf{x}_k^*) \\ \alpha \mathbf{L} \end{bmatrix}. \quad (3.50)$$

$\mathbf{J}_k(\mathbf{x}_k^*)$  denotes the Jacobian of the model output. The individual gradients of the Jacobian  $\nabla C_i$  are computed with respect to the predicted state vector  $\mathbf{x}_k^*$ . The parameter  $\alpha$  is a regularization parameter and  $\mathbf{L}$  is referred to as regularization matrix. With this regularization term it is possible to obtain a stable solution for the ill-posed inverse problem. The augmentation of equation (3.49) by  $\mathbf{0}$  effects a minimization of the regularization term. One possible choice of the matrix  $\mathbf{L}$  is a discrete version of the Laplace operator. Therefore the minimization of the regularization term results in a smooth material distribution. Because of the adaptation of the measurement vector in equation (3.49) also the covariance matrix  $\mathbf{R}_k$  has to be augmented to obtain a positive definite matrix of correct dimension. This can be done by

$$\mathbf{R}_k = \begin{bmatrix} \Sigma_{\mathbf{v}} & \mathbf{0} \\ \mathbf{0} & \sigma^2 \mathbf{I} \end{bmatrix}, \quad (3.51)$$

where  $\sigma^2$  is chosen to be the mean of the variances of the measurements [26]. To deal with the non-linearity of the ECT problem the update equation of the Kalman Filter (3.46) has to be extended by

$$\hat{\mathbf{x}}_k = \mathbf{x}_k^* + \mathbf{K}_k \left( \mathbf{y}_k - \begin{bmatrix} \mathbf{F}(\mathbf{x}_k^*) \\ \alpha \mathbf{L} \mathbf{x}_k^* \end{bmatrix} \right), \quad (3.52)$$

which is the form of the so called extended Kalman Filter [7].  $\mathbf{F}(\mathbf{x}_k^*)$  denotes the simulation of the non-linear forward problem of the ECT sensor for the predicted state vector  $\mathbf{x}_k^*$ . As the system matrix  $\Phi_k$  describes the dynamic behaviour of the system it is chosen to be the identity matrix  $\mathbf{I}$  for this estimation task, what is referred to as random walk.

For many applications the incorporation of state constraints is reasonable. To incorporate physical constraints to the state vector the so called maximum probability method can be used [27]. This method seeks for an estimation result by maximizing its probability with respect to certain constraints. As the probability of the estimation result is given by the covariance matrix  $\mathbf{P}_k$  the correct result is found by solving the following optimization problem

$$\begin{aligned} \arg \min_{\mathbf{x}_k} (\mathbf{x}_k - \hat{\mathbf{x}}_k)^T \mathbf{P}_k^{-1} (\mathbf{x}_k - \hat{\mathbf{x}}_k) \\ \text{s.t. } \mathbf{x}_{\min} \leq \mathbf{x}_k \leq \mathbf{x}_{\max}. \end{aligned} \quad (3.53)$$

Hereby  $\mathbf{x}_{\min}$  and  $\mathbf{x}_{\max}$  denotes the lower and the upper constraint for the state vector. As  $\hat{\mathbf{x}}_k$  is constant for this optimization problem, it can be written as

$$\begin{aligned} \arg \min_{\mathbf{x}_k} \mathbf{x}_k^T \mathbf{P}_k^{-1} \mathbf{x}_k - 2\hat{\mathbf{x}}_k^T \mathbf{P}_k^{-1} \mathbf{x}_k \\ \text{s.t. } \mathbf{x}_{\min} \leq \mathbf{x}_k \leq \mathbf{x}_{\max}, \end{aligned} \quad (3.54)$$

which forms a simple quadratic programming problem.

### Adaptations for the Incorporation of a Gaussian Prior

In a similar way the regularization can be done by the incorporation of a Gaussian prior to this estimation task. The Gaussian summary statistic is given by its probability density function  $\pi(\mathbf{x})$ , parametrized by means of the mean  $\boldsymbol{\mu}_{\mathbf{X}}$  and the covariance matrix  $\boldsymbol{\Sigma}_{\mathbf{X}}$  like already mentioned in section 3.1.

To properly achieve this the measurement equation (3.42) has to be augmented by

$$\mathbf{y}_k = \begin{bmatrix} \tilde{\mathbf{d}} \\ \boldsymbol{\mu}_{\mathbf{X}} \end{bmatrix}, \quad (3.55)$$

and

$$\mathbf{H}_k = \begin{bmatrix} \mathbf{J}_k(\mathbf{x}_k^*) \\ \mathbf{I} \end{bmatrix}, \quad (3.56)$$

where  $\mathbf{I}$  denotes the identity matrix. The covariance matrix  $\mathbf{R}_k$  is adapted by

$$\mathbf{R}_k = \begin{bmatrix} \boldsymbol{\Sigma}_{\mathbf{V}} & \mathbf{0} \\ \mathbf{0} & \boldsymbol{\Sigma}_{\mathbf{X}} \end{bmatrix}. \quad (3.57)$$

Given this approach, the update equation (3.46) has the following form

$$\hat{\mathbf{x}}_k = \mathbf{x}_k^* + \mathbf{K}_k \left( \mathbf{y}_k - \begin{bmatrix} \mathbf{F}(\mathbf{x}_k^*) \\ \mathbf{x}_k^* \end{bmatrix} \right). \quad (3.58)$$

This augmentation causes the estimation result to be drawn towards the mean of the prior distribution, which results in a stable solution for the ill-posed inverse problem.

The incorporation of state constraints can be done by means of the maximum probability method [27] shown in equation (3.54).

### Adaptations for the Incorporation of the State Reduction Approach

Another possible approach for the solution of the non-linear ill-posed inverse problem of ECT is an extended Kalman Filter in combination with the state reduction approach presented in section 3.3. For a proper choice of the reduced state space size by  $N_R < M$  a solution for the ill-posed estimation task can be found, as already mentioned in subsection 3.4.2. In this case the prior is incorporated by the projection matrix  $\mathbf{P}_{N_R}$ , which is constructed by means of random samples from the prior distribution  $\pi(\mathbf{x})$ .

Given this approach, the full state vector  $\mathbf{x}$  is replaced by the reduced state vector  $\mathbf{x}_R$ . The relation between the reduced state vector and the full state vector is given by equation (3.11). The system matrix  $\Phi$  is chosen to be an  $N_R \times N_R$  identity matrix, what is referred to as random walk. Hence the first Kalman Filter equation is given by

$$\mathbf{x}_{R,k}^* = \Phi \hat{\mathbf{x}}_{R,k-1}. \quad (3.59)$$

The measurement equation is again approximated by means of a Taylor series linearisation leading to the measurement matrix

$$\mathbf{H} = \mathbf{J}(\mathbf{P}_{N_R} \mathbf{x}_{R,k}^*). \quad (3.60)$$

To overcome the non-linearity of the ECT forward map, the update equation (3.47) is replaced by

$$\hat{\mathbf{x}}_{R,k} = \mathbf{x}_{R,k}^* + \mathbf{K}_k (\mathbf{y}_k - \mathbf{F}(\mathbf{P}_{N_R} \mathbf{x}_{R,k}^*)). \quad (3.61)$$

In this case  $\mathbf{y}_k$  is given by the data vector  $\tilde{\mathbf{d}}$  since no regularization term is required due to the state reduction.

The incorporation of physical constraints to the estimated state vector is done by the maximum probability method [27]. Since the constraints for the

reduced state vector  $\mathbf{x}_R$  are usually not known the projection matrix  $\mathbf{P}_{N_R}$  has to be incorporated to the approach shown in equation (3.54). Therefore

$$\begin{aligned} \min_{\mathbf{x}_{R,k}} \mathbf{x}_{R,k}^T \mathbf{P}_{N_R}^T \mathbf{P}_k^{-1} \mathbf{P}_{N_R} \mathbf{x}_{R,k} - 2\hat{\mathbf{x}}_{R,k}^T \mathbf{P}_k^{-1} \mathbf{P}_{N_R} \mathbf{x}_{R,k} \\ \text{s.t. } \mathbf{x}_{\min} \leq \mathbf{P}_{N_R} \mathbf{x}_{R,k} \leq \mathbf{x}_{\max}, \end{aligned} \quad (3.62)$$

has to be solved.

Since the Kalman Filter is an iterative algorithm a starting point for the state vector  $\hat{\mathbf{x}}_{R,0}$  is necessary. An obvious choice is the mean  $\boldsymbol{\mu}_{\mathbf{X}}$  of the generated samples from the prior distribution  $\pi(\mathbf{x})$ , which were used to generate the projection matrix  $\mathbf{P}_{N_R}$ . The computation of the reduced representation of  $\boldsymbol{\mu}_{\mathbf{X}}$  can be done in an least squares sense

$$\hat{\mathbf{x}}_{R,0} = (\mathbf{P}_{N_R}^T \mathbf{P}_{N_R})^{-1} \mathbf{P}_{N_R}^T \boldsymbol{\mu}_{\mathbf{X}}. \quad (3.63)$$

For estimation tasks with known physical constraints, it has to be verified if no constraints are violated by  $\hat{\mathbf{x}}_{R,0}$ . To guarantee  $\hat{\mathbf{x}}_{R,0}$  to be within the boundaries, also a constraint least squares approximation can be applied.

### 3.5.2 Gibbs Sampler

The Gibbs sampler belongs to the class of Markov chain Monte Carlo (MCMC) techniques. MCMC algorithms are a class of random sampling methods, suitable for the generation of independent random samples of the posterior distribution  $\pi(\mathbf{x}|\mathbf{d})$  [9]. Before going into a detailed description of the algorithm the basic idea about Markov chains and Monte Carlo integration are explained.

#### Markov Chains

The essential element within MCMC techniques are the so called Markov chains. Let  $\mathcal{M} = \{X_n\}_{n=0}^{\infty}$  be a sequence of random variables in the state space  $\mathcal{X}$ . A Markov chain is a process  $\mathcal{M} = \{X_n\}_{n=0}^{\infty}$  with the property

$$P_r(X_{n+1} = x_{n+1} | X_n = x_n, \dots, X_0 = x_0) = P_r(X_{n+1} = x_{n+1} | X_n = x_n) \quad (3.64)$$

referred to as Markov condition. In words, the probability of  $X_{n+1}$  conditioned on  $X_1 = x_1, \dots, X_n = x_n$  is equals the probability conditioned on  $X_n = x_n$ . This means that the state  $X_{n+1}$  only depends on the previous state  $X_n$  [9]. The transition kernel  $K(x_n, x_{n+1})$  describes the transition probability between the two consecutive states  $X_n$  and  $X_{n+1}$ . This will be part of the

algorithm to generate new candidates.

A detailed description of the properties Markov chains offer can be found in [28] and [29]. In particular two properties of Markov Chains are of special interest to apply them for Monte Carlo integration, which are briefly described in the following paragraph.

The first important property of the chain is given by the irreducibility. For discrete state spaces, the property of irreducibility is given by the fact that the transition kernel  $K$  has a non zero transition probability between each combination of states.

The second important property is the so called periodicity of Markov chains. If the state  $x_{n+j}$  can become the state  $x_n$  for  $j > 2$  a Markov Chain is called periodic. The kernel is aperiodic if  $x_{n+1} = x_n$  is allowed.

If the properties of irreducibility and aperiodicity are fulfilled by the Markov chain, the sequence  $\mathcal{M}$  converges against the target distribution  $\pi$  for sufficient large  $n$ . Hence Monte Carlo Integration can be applied [29].

### Monte Carlo Integration

A Markov Chain provides a set of random samples from the probability density function  $\pi(\mathbf{x})$ . These samples  $\mathbf{x}_i$  of  $\pi(\mathbf{x})$  can be used to approximate integrals of a function  $f(\mathbf{x})$  by

$$\int_{\mathbb{R}^N} f(\mathbf{x}) \pi(\mathbf{x}) d\mathbf{x} \approx \frac{1}{N} \sum_{i=1}^N f(\mathbf{x}_i), \quad (3.65)$$

which is referred to as Monte Carlo integration. With this method it is possible to compute complex integrals by the mean of the samples generated by the Markov chain. This can be useful, to compute the so called conditional mean (CM)

$$\mathbf{x}_{\text{CM}} = \int_{\mathbb{R}^N} \mathbf{x} \pi(\mathbf{x} | \tilde{\mathbf{d}}) d\mathbf{x}, \quad (3.66)$$

and the conditional covariance

$$\text{cov}(\mathbf{x}, \tilde{\mathbf{d}}) = \int_{\mathbb{R}^N} (\mathbf{x} - \mathbf{x}_{\text{CM}})^T (\mathbf{x} - \mathbf{x}_{\text{CM}}) \pi(\mathbf{x} | \tilde{\mathbf{d}}) d\mathbf{x}. \quad (3.67)$$

The MAP or ML estimator are also termed as point estimates, since the solution is always one point given by the maxima of the posterior distribution. The CM instead uses information of the whole posterior distribution. This property makes the CM also suitable for multi-modal distributions. MCMC techniques offers an efficient tool for the solution of those, often high dimensional integrals [9]. The evaluation of the conditional covariance given by equation (3.67) enables also access to uncertainty information about the estimation result.

### The Algorithm

Given the concept of Markov chains and Monte Carlo integration a method is needed to generate the samples from the posterior distribution  $\pi(\mathbf{x}|\tilde{\mathbf{d}})$ . One possible algorithm for this task is the so called Gibbs sampler.

Detailed information about the Gibbs sampler can be found in [30]. The main steps of the algorithm are given by:

1. The current state  $\mathbf{x} = \mathbf{X}_n$  is selected.
2. For every element  $i$  of the state vector  $\mathbf{x}$  the following steps are performed:
  - (a) All elements of  $\mathbf{x}$  instead of  $x_i$  are fixed.
  - (b) A sample from the conditional distribution

$$\pi(x_i|x_1, x_2, \dots, x_{i-1}, x_{i+1}, \dots, x_N), \quad (3.68)$$

is generated.

3. The new state is set to  $\mathbf{X}_{n+1} = \mathbf{x}$ .

Since the element  $x_i$  is the only variable of the conditional distribution given by (3.68), a one dimensional sampling method is required. An efficient scheme for this task is rejection sampling [30]. There are different versions for rejection sampling. For this task a version is chosen, which provides the possibility to work on the logarithm of the posterior distribution. This provides numerical advantages [10], if the condition holds that the target density  $g(x)$  offers logarithmically concave behaviour [31]. The rejection sampler works on the logarithm of the target density function  $h(s) = \ln(g(x))$ . The algorithm requires an upper  $u(x)$  and a lower  $l(x)$  bound of the  $h(x)$  so that  $l(x) \leq h(x) \leq u(x)$  holds. The upper and the lower bound can be assembled by piecewise linear functions and  $M$  supporting points of the conditional

distribution. Given this, a sample of  $g(x)$  can be generated by the following steps:

1. Sample a point  $x$  from  $u(x)$  and generate an uniform distributed sample  $w \propto \mathcal{U}([0, 1])$ .
2. Accept  $x$  if  $w \leq \exp(l(x) - u(x))$  holds.
3. If not,  $x$  is accepted in the case of  $w \leq \exp(h(x) - u(x))$ , or else repeat this steps.

Given the exact fast low rank update approach presented in subsection 2.4.6, the one dimensional sampling can be done in an efficient way. This enables the solution of the ill-posed inverse problem within an appropriate time.

### Gibbs Sampling for Bimodal Material Distributions

The most simple case is given by bimodal material distributions. In this case the Gibbs sampler simplifies to the following scheme [10]:

1. Flip the value of one element  $x_i$  of the state vector  $\mathbf{x}$  to generate the proposal  $\mathbf{x}'$ .
2. Evaluate  $\alpha = \min \left[ 1, \frac{\pi(\mathbf{x}'|\tilde{\mathbf{d}})}{\pi(\mathbf{x}|\tilde{\mathbf{d}})} \right]$ .
3. The proposal  $\mathbf{x}'$  is accepted with the probability  $\alpha$ .

The selection of the element  $i$  can be done by a loop, to update all elements of  $\mathbf{x}$  consecutively. For a small difference between the two material values, the evaluation of  $\pi(\mathbf{x}'|\tilde{\mathbf{d}})$  can be done by means of the Jacobian approximation.

# 4 Flow Parameter Estimation

This chapter discusses the application of electrical capacitance tomography for flow parameter estimation in pneumatic conveying systems.

In the first section the prevailing flow patterns in pneumatic conveying systems are investigated for horizontal and vertical pipe systems. Out of this flow patterns, random sample generators are constructed to obtain a sample based prior for the reconstruction algorithms presented in chapter 3.

In the second section the intrinsic information of the random samples from the different prior distributions is analysed by means of a principle component analysis. This is also used to make a proper choice for the size of the reduced state space presented in section 3.3. Also an intuitive approach for the construction of basis vectors for a reduced state representation is presented for flow patterns.

The third section discusses the different flow parameters in pneumatic conveying systems and the definition of the solid volume concentration, which is the process quantity of interest.

The last section of this chapter is intended to give an overview of the implemented reconstruction algorithms and a detailed declaration of the setup used for the implementation. Lastly the notation and the abbreviations are explained, which are used for the different algorithms.

## 4.1 Flow Regimes in Pneumatic Conveying Systems

This section is intended to provide an overview about the occurring spatial concentrations of the material distributions in pneumatic conveying systems, also referred to as flow regimes. The flow regimes in pneumatic conveying

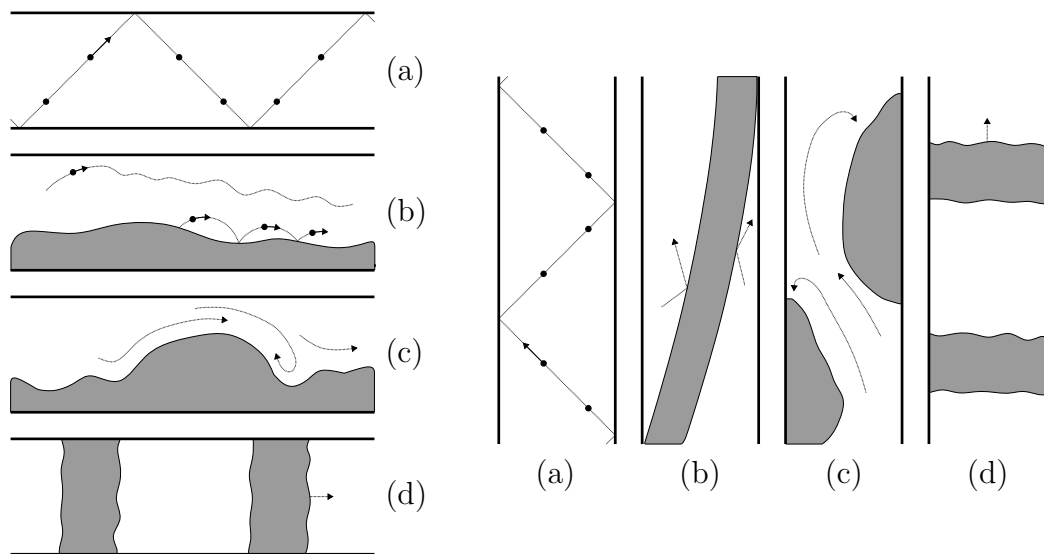


**Figure 4.1:** Flow regimes in horizontal and vertical pneumatic conveying systems [32] [33].

systems depend on several process parameters such as the pressure drop  $\Delta p$  (or the pressure gradient  $\Delta p/L$ ) along the length of the pipe  $L$  and the gas velocity  $v_g$ . Given these parameters a rough classification of the flow regimes for horizontal and vertical upward conveying is depicted in figure 4.1 [32] [33].

For horizontal pneumatic conveying systems the different flow regimes are given by [33]

- (a) *Dispersive flow*: For high gas velocities  $v_g$  the particles are moving homogeneously distributed over the whole cross-section of the process pipe. The particles are occasionally colliding with other particles and the pipe wall.
- (b) *Stratified flow*: With decreasing gas velocities a part of the particles is settling down and sliding along the bottom of the pipe. Only a part of the solid particles is conveyed as dilute flow above the solid bottom layer.
- (c) *Slug Flow and unstable flow*: For a further decrease of the gas velocity slugs are formed, which are slowly conveyed along the bottom of the pipe. A repeated reduction of  $v_g$  leads to dormant deposits on the bottom of the tube sheet so that only a fraction of the whole cross-section is used for conveying. This flow regime is greatly unstable since uncontrolled plug formations can occur.

- (d) *Plug flow*: For very low gas velocities but high pressure drops the so called plug flow can occur. Here, solid plugs are conveyed along the pipe, occupying the whole diameter of the pipe. This is the characteristic flow regime for the so called dense flow conveying.

For vertical upwards conveying analogous flow regimes as for horizontal conveying are occurring [33]. For high gas velocities the solid particles are homogeneous distributed over the cross-section and conveyed along the pipe. For lower gas velocities the dispersive flow merges to the stratified flow. Due to the formation of strands a local reverse flow of the particles can occur in the opposite direction of the gas flow until the strands are again dissolving. For this reason installation positions of the ECT sensor were vertical upward conveying is present are not suitable since the solid particles are possibly moving in two directions. This complicates the estimation of flow parameters significantly and is therefore not further considered in this thesis.

A further case considered is vertical downwards conveying, termed gravity-driven flow. For a sufficient long straight process pipe ahead of the ECT sensor the occurring flow pattern is given by a concentration of the bulk material in the center of the pipe with an decreasing density towards the pipe wall [34].

#### 4.1.1 Random Samples for Flow Patterns

Given the prevailing flow regimes in pneumatic conveying systems the task is now to generate random patterns, which are covering the possible states of the conveying process. These samples for flow type material distributions forming a sample based prior information. To incorporate this information to the reconstruction algorithms a Gaussian summary statistic of a set of random samples is computed, as presented in 3.2.

##### Random Samples for Horizontal Conveying Flow Patterns

Figure 4.2 depict exemplary samples for horizontal conveying flow regimes. Since the samples are cross sectional representations of the prevailing flow regimes, they can be summarized for this task by four cases. The first case is a dilute flow with homogeneous distributed particles over the whole cross section of the pipe depict in figure 4.2(a). This dilute flow is modeled by means of a randomly selected constant material value in the region of interest. The second case is also dilute flow but with a concentration of the particles on the bottom of the pipe depict in 4.2(b). Therefore a random

height  $h$  is generated, which divides the region of interest into two domains. The randomly selected material value  $\varepsilon_{r,1}$  is assigned to the lower domain and  $\varepsilon_{r,2}$  is assigned to the upper domain where  $\varepsilon_{r,1} > \varepsilon_{r,2}$  holds. The third case is given by solid deposits on the bottom of the pipe and dilute flow in the upper domain depict in 4.2(c). Therefore again a height  $h$  is randomly generated and the material value  $\varepsilon_{r,\max}$  is assigned to the lower domain and the randomly generated value  $\varepsilon_r$  is assigned to the upper domain, where  $\varepsilon_r < \varepsilon_{r,\max}$  holds. The fourth case is given by solid deposits on the bottom only depict in 4.2(d). In this case the material value of the upper domain is set to  $x = 1$  and the material value of the lower domain is again set to  $\varepsilon_{r,\max}$ . For the generation of the samples the four different regimes are selected randomly. Given the flow regime and the parameters, the inclusion is mapped onto the finite element mesh, providing the random sample  $\mathbf{x}$ . The pseudo code for this pattern generator is given by algorithm 4.1.

---

**Algorithm 4.1** Algorithm to obtain random samples for horizontal conveying flow patterns.

---

```

1:   Pick number  $\#_{\text{regime}}$  between 1 : 4 by random
2:   if  $\#_{\text{regime}} = 1$ 
3:       Draw  $\varepsilon_r \propto \mathcal{U}(\varepsilon_{r,\min}, \varepsilon_{r,\max})$ 
4:       Set whole ROI to  $\varepsilon_r$ 
5:   else if  $\#_{\text{regime}} = 2$ 
6:       Draw  $h \propto \mathcal{U}(h_{\min}, h_{\max})$ 
7:       Draw  $\varepsilon_{r,1} \propto \mathcal{U}(\varepsilon_{r,\min}, \varepsilon_{r,\max})$  and  $\varepsilon_{r,2} \propto \mathcal{U}(\varepsilon_{r,\min}, \varepsilon_{r,1})$ 
8:       Set ROI domain  $< h$  to  $\varepsilon_{r,1}$  and  $> h$  to  $\varepsilon_{r,2}$ 
9:   else if  $\#_{\text{regime}} = 3$ 
10:      Draw  $h \propto \mathcal{U}(h_{\min}, h_{\max})$ 
11:      Draw  $\varepsilon_r \propto \mathcal{U}(\varepsilon_{r,\min}, \varepsilon_{r,\max})$ 
12:      Set domain  $< h$  to  $\varepsilon_{r,\max}$  and domain  $> h$  to  $\varepsilon_r$ 
13:   else if  $\#_{\text{regime}} = 4$ 
14:      Draw  $h \propto \mathcal{U}(h_{\min}, h_{\max})$ 
15:      Set domain  $< h$  to  $\varepsilon_{r,\max}$  and the domain  $> h$  to  $\varepsilon_{r,\min}$ 
16:   end
17:   Map the inclusion onto the finite element mesh  $\rightarrow \mathbf{x}$ 

```

---

### Random Samples for Vertical Downwards Conveying Flow Patterns

Figure 4.3 depict exemplary samples for vertical downwards conveying flow patterns. These samples are generated by means of a centred Gaussian inclusion. Since the center coordinate of the ECT sensor model is given by the

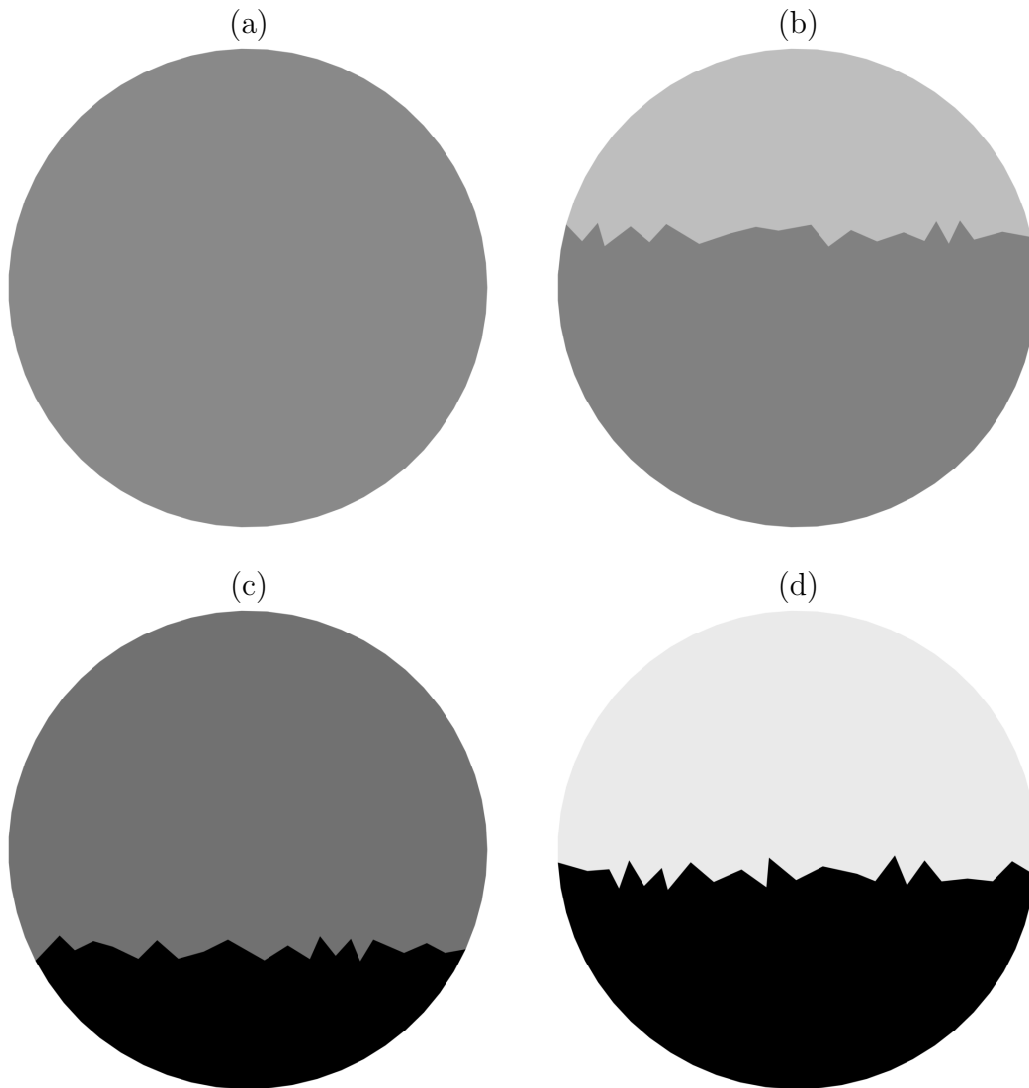


**Figure 4.2:** Exemplary random samples for the different flow regimes in horizontal pneumatic conveying systems. (a) dilute flow, (b) dilute flow with concentration on the bottom, (c) solid bottom layer and dilute flow in the upper layer, (d) solid bottom layer only.

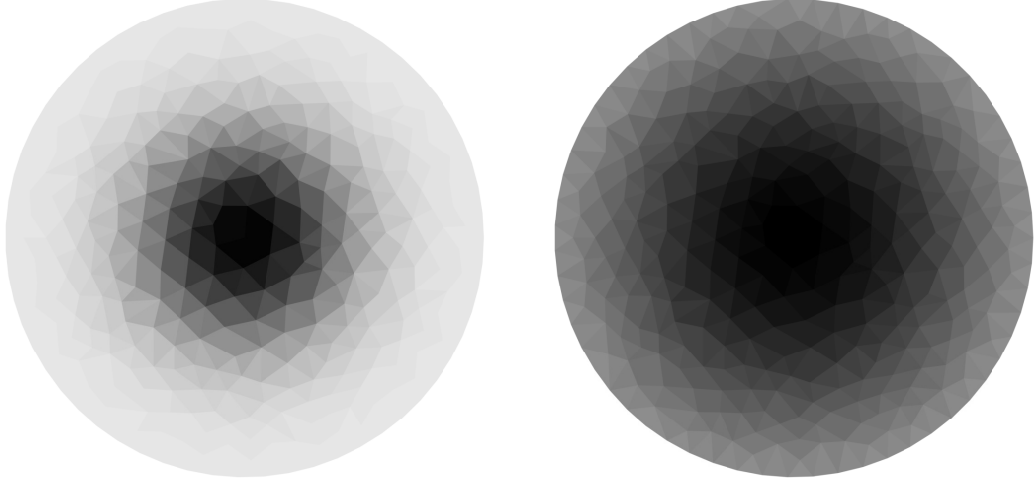


**Figure 4.3:** Exemplary random samples for vertical downwards conveying flow patterns.

point  $[0, 0]$ , the center point of the Gaussian inclusion is also chosen to be  $[\mu_x, \mu_y] = [0, 0]$ . The standard deviation  $\sigma$  and the material value  $\varepsilon_r$  of the inclusion are randomly selected by means of an uniform distribution. The mapping of the inclusion onto the finite element mesh is again done by equation (3.7), providing the sample  $\mathbf{x}$ . A pseudo code for the generation of this samples is given by algorithm 4.2.

---

**Algorithm 4.2** Algorithm to obtain random samples for vertical downwards conveying flow patterns.

---

- 1: Center point  $[c_x, c_y] = [0, 0]$
  - 2: Draw  $\sigma \propto \mathcal{U}(\sigma_{\min}, \sigma_{\max})$
  - 3: Draw  $\varepsilon_r \propto \mathcal{U}(\varepsilon_{r,\min}, \varepsilon_{r,\max})$
  - 4: Create the inclusion out of the parameters
  - 5: Map the inclusion onto the finite element mesh  $\rightarrow \mathbf{x}$
- 

## 4.2 Analysis of the Intrinsic Information of the Prior Samples

In this section an investigation of the random samples from the different prior distributions is done by means of an singular value decomposition given by equation (3.12). Since the state reduction approach presented in section 3.3 is based on a principle component analysis of the random samples, the re-

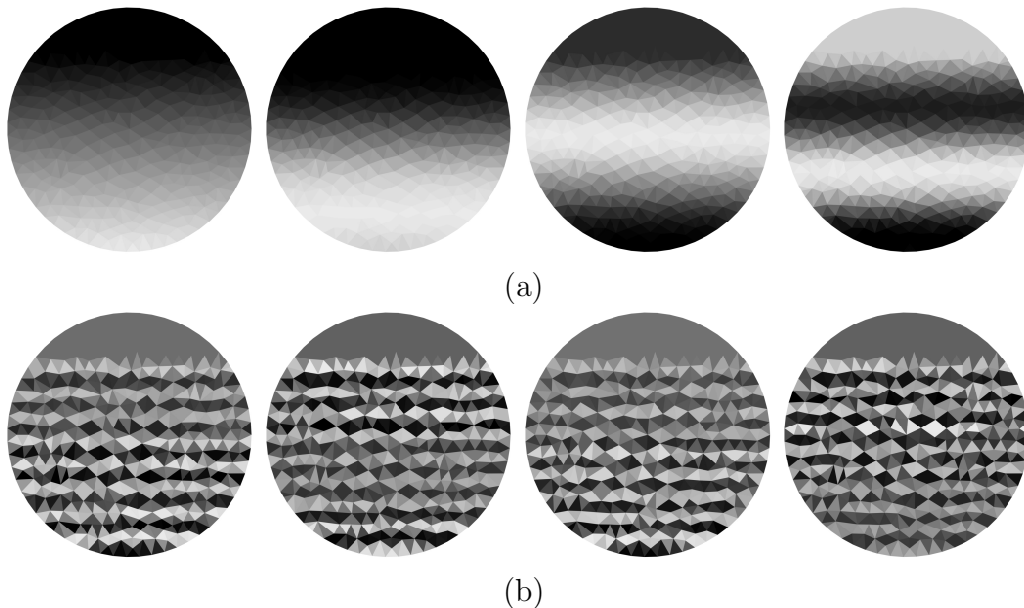


**Figure 4.4:** PCA basis vectors for horizontal conveying flow patterns, (a) for low index numbers, (b) for high index numbers.

sults achieved in this sections are used to choose a proper size of the reduced state representation  $N_R$ . It should be mentioned that only the samples from prior distributions for flow patterns are analysed here in detail. Detailed investigations about the samples from arbitrary Gaussian and rod type prior distributions can be found in [19]. Nevertheless the Gaussian and rod type samples are mentioned here to draw a comparison between the prior information for flow patterns and arbitrary material distributions.

The analysis of the intrinsic information of flow type random samples leads to an intuitive approach for the construction of basis vectors  $\mathbf{u}_i$  for a reduced state space. Therefore the construction of those basis vectors and the assembly of the projection matrix  $\mathbf{P}_{N_R}$  is discussed in detail. The concept of state reduction is presented in section 3.3.

### 4.2.1 Principle Component Analysis

In this subsection the intrinsic information of a set of random samples from an prior distribution is analysed. Therefore a principle component analysis by means of a singular value decomposition is implemented providing the basis vectors  $\mathbf{u}_i$ . The procedure to accomplish this is explained in detail in section 3.3. The focus in this subsection lies especially in the investigation

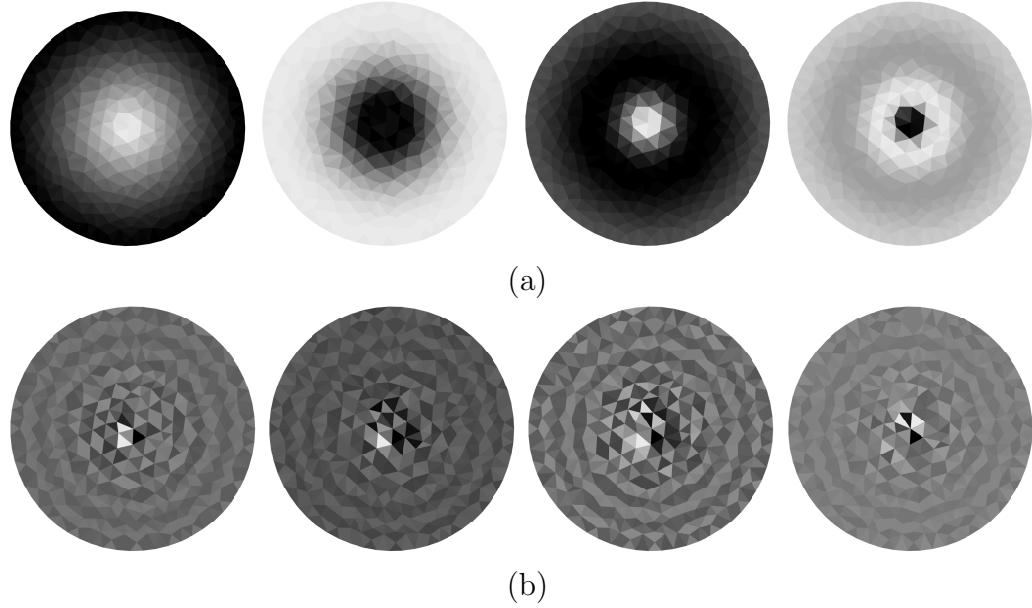


**Figure 4.5:** PCA basis vectors for vertical downwards conveying flow patterns, (a) for low index numbers, (b) for high index numbers.

of flow type samples.

In figure 4.4 and 4.5 some basis vectors for horizontal and vertical downwards conveying flow samples are depicted. The subfigures (a) exemplarily depict the basis vectors for low index numbers  $i$ . The subfigures (b) exemplarily depict the basis vectors for high index numbers. The index numbers  $i$  of the basis vectors correspond to the columns of the matrix  $\mathbf{U}$ . It is evident, that the basis vectors behave smooth for low index numbers and become more oscillating for higher index numbers. The same characteristics are shown for Gaussian and rod type samples in [19]. Although plotting the basis vectors provides information about their behaviour it is not suitable for making a proper decision for the size of the reduced state representation  $N_R$ . Since the singular values given by the diagonal matrix  $\mathbf{\Sigma}$  can be seen as an importance weight of the basis vectors, they are a more appropriate indicator for the choice of  $N_R$ . Figure 4.6 depicts the trend of the singular values for different sets of random samples. Note that the singular vectors are normalized to make a meaningful comparison between the different sets of samples. The singular values are decreasing in every case for higher index numbers. This fact corresponds to the behaviour of the basis vectors since they become more oscillating for high index numbers. These oscillating basis vectors have a lower importance for the representation of the prevailing patterns. Although

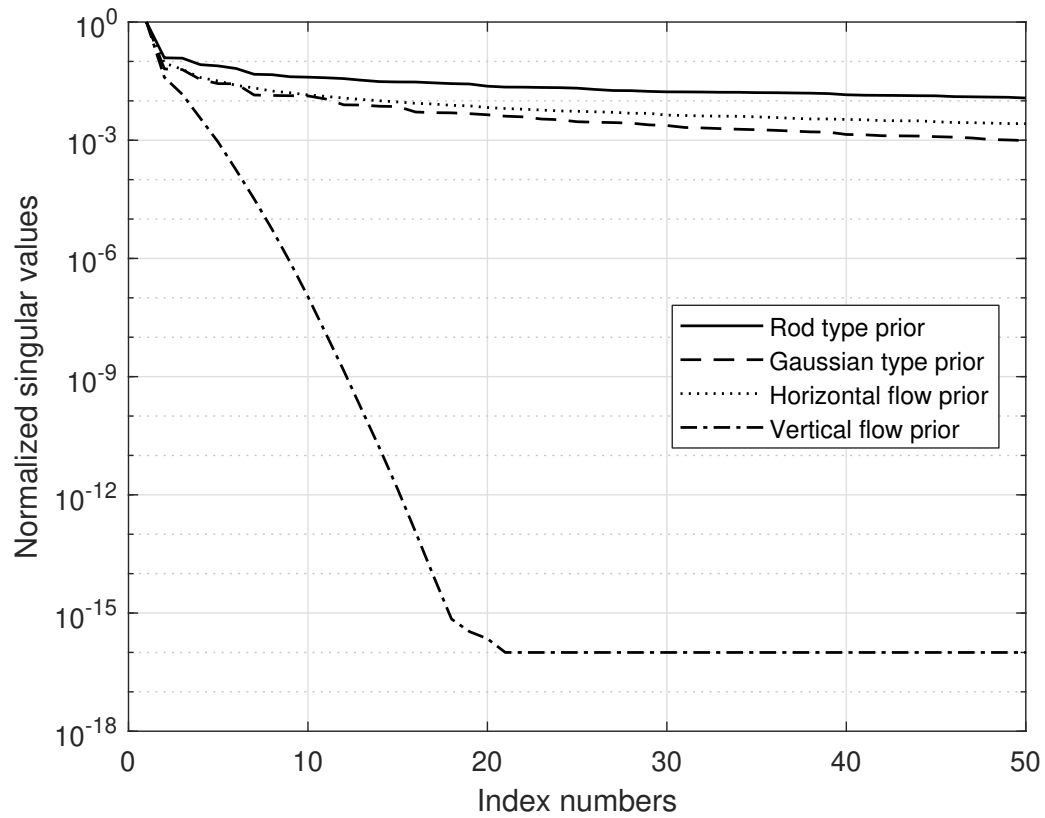


**Figure 4.6:** Trend of the singular values of matrices holding random samples from different prior distributions.

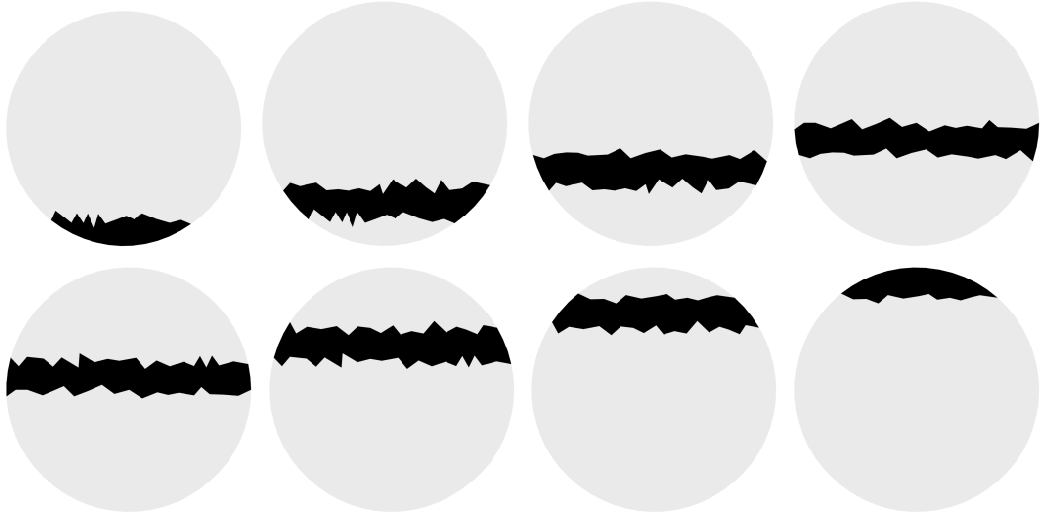


**Figure 4.7:** Intuitive basis vectors for horizontal conveying flow patterns.

a lot of structure is incorporated by means of the flow patterns, the decrease of the singular values for the horizontal conveying flow patterns is in the same scale as for the arbitrary Gauss and rod type patterns. This is explained due to the smooth behaviour of the basis vectors. The sharp change in the material values in the transition between the top and the bottom layer of the horizontal conveying flow patterns is hard to reconstruct by means of this smooth basis vectors. However the vertical downwards conveying flow patterns are modeled by means of centred Gaussian material distributions, which are smooth functions. For this reason the singular values decrease much faster since this patterns can be easily represented by means of a few basis vectors.

#### 4.2.2 An Intuitive Approach for the Reduced State Representation for Flow Patterns

Since the structure of the flow patterns in the horizontal conveying as well as in the vertical downwards conveying case is well known, this subsection is intended to discuss an intuitive approach for the construction of basis vectors  $\mathbf{u}_i$  for a reduced state representation.

The horizontal conveying flow patterns are modeled by means of different layers with constant material values. Therefore one reasonable approach for the basis vectors would be the use of non overlapping horizontal layers. This basis vectors are exemplary depict in figure 4.7 for a reduced state space size

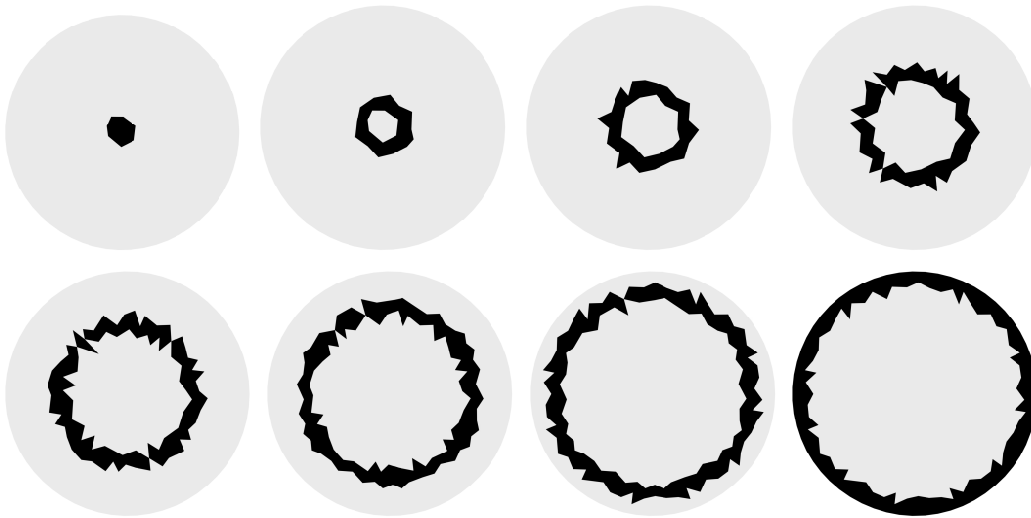


**Figure 4.8:** Intuitive basis vectors for vertical downwards conveying flow patterns.

of  $N_R = 8$ . The main advantage of this intuitive basis vectors is given by the fact, that non overlapping layers are suitable to model sharp material transitions. A lower limit for the thickness of the layers is given by the size of the finite elements of the ECT model. Therefore the size of the reduced state space  $N_R$  is also limited to certain values.

In a similar way it is possible to construct basis vectors for vertical downwards conveying flow patterns. Since the vertical downwards flow is modeled by means of centred Gaussian material distributions, an intuitive approach for the basis vectors is given by non overlapping concentric rings with constant material values. This basis vectors are exemplary depict in figure 4.8 for a reduced state space size of  $N_R = 8$ . The number of basis vectors relates to the width of the rings, which represents the basis vectors. The minimal width is limited by the size of the finite elements of the ECT model. In the case of vertical downwards conveying flow patterns the intuitive approach may not yield to more precise results than the state reduction approach by means of a principle component analysis. Though due to the non overlapping basis vectors of the intuitive approach the incorporation of state constraints can be done more easily. In this case the constraints for the reduced state vector are the same as for the original state vector. This fact may be advantageous for several reconstruction algorithms, to easily incorporate constraints to the estimation result.

The basis vectors  $\mathbf{u}_i$  are now given by vectors holding the value of 1 for the finite elements corresponding to the layers or the rings. The projection matrix  $\mathbf{P}_{N_R}$  for the mapping between the reduced and the original state space given by equation (3.11) can be constructed by

$$\mathbf{P}_{N_R} = [\mathbf{u}_1 \quad \mathbf{u}_2 \quad \dots \quad \mathbf{u}_{N_R}]. \quad (4.1)$$

With respect to equation (3.13), the leading vector  $\mathbf{1}$  is not necessary in this case, as a constant material distribution can be constructed by a simple combination of the basis vectors  $\mathbf{u}_i$ .

### 4.3 Estimation of the Volume Concentration by means of ECT

Since the aim of this thesis is the estimation of the average solid volume concentration  $\bar{\beta}_S(t)$ , this section is intended to provide the taken approach to accomplish this. In general the mass flow rate is given by

$$\dot{m}(t) = \iint_{\Gamma_{\text{ROI}}} \rho(x, y, t) v(x, y, t) dx dy, \quad (4.2)$$

where  $\rho(x, y, t)$  denotes the instantaneous density at position  $(x, y)$  and time instant  $t$  in  $\text{kg}/\text{m}^3$  and  $v(x, y, t)$  denotes the instantaneous velocity at the same position and time instant in  $\text{m}/\text{s}$  [1].  $\Gamma_{\text{ROI}}$  denotes the cross section of the process pipe in  $\text{m}^2$ . Given a constant density of the solid particles  $\rho_S$ , the instantaneous density can be expressed by

$$\rho(x, y, t) = \rho_S \beta_S(x, y, t), \quad (4.3)$$

with the unitless instantaneous solid volume concentration  $\beta_S(x, y, t)$  at position  $(x, y)$ . For uniform flows, where the particles moves along their flow lines with constant velocity, equation (4.2) is simplified to [4]

$$\dot{m}(t) = \rho_S \Gamma_{\text{ROI}} \bar{v}(t) \bar{\beta}_S(t). \quad (4.4)$$

Here  $\bar{v}(t)$  denotes the average velocity of the solid particles and  $\bar{\beta}_S(t)$  denotes the average solid volume concentration.

The reconstruction result of the inverse problem of ECT is given by the instantaneous spatial distribution of the relative permittivity  $\varepsilon_r(x, y, t)$  within the sensor. For this reason a relation between the electrical material parameter  $\varepsilon_r(x, y, t)$  and the parameter of interest  $\bar{\beta}_S(t)$  is required. The estimation

### 4.3. Estimation of the Volume Concentration by means of ECT 59

of the solid volume concentration is based on the assumption that the instantaneous density  $\rho(x, y, t)$  is related to the reconstructed electrical material parameters by

$$\rho(x, y, t) \propto \varepsilon(x, y, t) - 1 = \chi(x, y, t). \quad (4.5)$$

Here  $\chi(x, y, t)$  denotes the instantaneous susceptibility. Due to the assumption of a constant density of the solid particles  $\rho_S$  given by equation (4.3), the relation (4.5) can also be stated as

$$\beta_S(x, y, t) \propto \chi(x, y, t). \quad (4.6)$$

The taken approach to describe this relation is the assumption of a linear dependence of  $\beta_S(x, y, t)$  on  $\chi(x, y, t)$  of the form [1]

$$\beta_S(x, y, t) = \frac{\chi(x, y, t)}{\chi_{\max}}, \quad (4.7)$$

where  $0 \leq \beta_S \leq 1$  holds and  $\chi_{\max}$  denotes the true susceptibility of the solid particles. Since  $\chi_{\max}$  has to be known for this approach, the material value used for the prior samples is used. The cross-sectional average of the solid volume concentration is given by

$$\bar{\beta}_S(t) = \frac{1}{\Gamma_{\text{ROI}}} \iint_{\Gamma_{\text{ROI}}} \frac{\chi(x, y, t)}{\chi_{\max}} dx dy. \quad (4.8)$$

Since the simulation model of the ECT sensor is based on a finite element discretization of the problem domain no continuous distribution of  $\chi(x, y, t)$  is available. Instead the material values of the single finite elements are obtained by the reconstruction algorithms. For this reason the integral shown in equation (4.8) can be approximated by means of a sum given by

$$\bar{\beta}_S(t) \approx \frac{1}{\Gamma_{\text{ROI}}} \sum_{i=1}^{N_{\text{ROI}}} \frac{\chi_i(t)}{\chi_{\max}} \Gamma_i, \quad (4.9)$$

where  $\chi_i(t)$  denotes the susceptibility of the  $i^{\text{th}}$  finite element at the time instant  $t$  and  $\Gamma_i$  is the corresponding area of the finite element.  $N_{\text{ROI}}$  denotes the number of finite elements within the cross-section  $\Gamma_{\text{ROI}}$ . Given this approach at least the two extremal values of  $\chi$  results in the true solid volume concentration. Since the susceptibility of air is given by  $\chi_{\min} = 0$ . The solid volume concentration of the domain of the  $i^{\text{th}}$  finite element with the material value  $\chi_i = \chi_{\min}$  yield a value of  $\bar{\beta}_{S,i} = 0$ . If the material value of the  $i^{\text{th}}$  finite element is given by  $\chi_i = \chi_{\max}$  the solid volume concentration for the corresponding domain results in a value of  $\bar{\beta}_{S,i} = 1$ .

## 4.4 Reconstruction Algorithm Setup and Notation

This section is intended to provide a detailed description of the setups of the different reconstruction algorithms. Also the notation used for the algorithms and their setup is explained in detail.

### 4.4.1 Algorithm Setup

The following subsections discuss the particular implementations of the individual algorithms in detail.

#### Optimal Approximation Algorithms

The optimal approximation algorithms (OA) are presented in subsection 3.4.1. The random samples required for the assembly of the matrix  $\mathbf{X}$  are provided by the random sample generators presented in subsection 3.2.1 and 4.1.1. A number of  $N_{\text{sample}} = 5000$  samples is used for the implementation of the optimal approximation algorithms.

The matrix  $\tilde{\mathbf{D}}_a$  is obtained by simulating the forward map  $\mathbf{F}(\mathbf{x})$  of the ECT sensor presented in chapter 2 for the single random samples.

To take measurement noise into account, respectively 5 noisy realizations of  $\tilde{\mathbf{d}}_a$  are generated to assembly  $\tilde{\mathbf{D}}_a$ .

For the incorporation of the state reduction approach the computation of the reduced state vector  $\mathbf{x}_R$  is done by the estimator given in equation (3.15). The incorporation of a lower constraint is reasonable as the estimation result is given by relative permittivity values which, have an lower physical boundary of 1.

#### Linearised MAP and ML Type Estimators

The linearised MAP and ML type algorithms are presented in subsection 3.4.2. An explicit noise model is necessary to implement these algorithms. Therefore the covariance matrix  $\Sigma_{\mathbf{v}}$  is assembled by

$$\Sigma_{\mathbf{v}} = \text{diag}(\sigma_i^2), \quad (4.10)$$

where the variance  $\sigma_i^2$  is given by the noise power of the corresponding measurement.

The parameters  $\boldsymbol{\mu}_{\mathbf{x}}$  and  $\boldsymbol{\Sigma}_{\mathbf{x}}$  of the Gaussian prior distribution  $\pi(\mathbf{x})$  are obtained by the procedure given in subsection 3.2.2. The random samples needed for the construction of  $\pi(\mathbf{x})$  are provided by the random sample generators presented in subsection 3.2.1 and subsection 4.1.1. A number of  $N_{\text{sample}} = 5000$  random samples is used to compute the Gaussian summary statistic.

The Jacobian required for the linearisation of the forward map is obtained by the procedure presented in subsection 2.4.5.

To ensure valid solutions a lower constraint of 1 is incorporated to the solution vector  $\mathbf{x}$  since  $\varepsilon_r \geq 1$  has to hold. To do so the optimization problem of the LMAP and LML estimator is solved in each case by means of a constraint quadratic programming problem given by equation (3.31), (3.34) and (3.40).

To investigate the impact of the state constraints also a linear MAP estimator without constraints is implemented given by equation (3.30).

### Kalman Filter

The Kalman filter is presented in subsection 3.5.1. The same noise model as described for the linearised MAP and ML type estimators is used. The covariance matrix of the noise  $\boldsymbol{\Sigma}_{\mathbf{v}}$  is given by equation (4.10).

The construction of an Gaussian prior pdf  $\pi(\mathbf{x})$  by means of the mean  $\boldsymbol{\mu}_{\mathbf{x}}$  and the covariance matrix  $\boldsymbol{\Sigma}_{\mathbf{x}}$  is done with the procedure presented in subsection 3.2.2. The samples needed for this approach are provided by the sample generators presented in 3.2.1 and 4.1.1 whereby a number of  $N_{\text{sample}} = 5000$  random samples are used.

The Jacobian required for the adaptation of the measurement matrix  $\mathbf{H}_k$  is obtained by the procedure presented in subsection 2.4.5. The forward map  $\mathbf{F}(\mathbf{x})$  of the ECT sensor used in the measurement equation of the Kalman filter is derived in chapter 2.

In each of the different Kalman filter implementations the maximum probability method is applied given by equation (3.54) to guarantee that  $\varepsilon_r \geq 1$  holds for the estimation result.

Since the Kalman filter is an iterative algorithm, initial values for the state

vector  $\hat{\mathbf{x}}_0$  and for the covariance matrix  $\mathbf{P}_0$  are necessary. One obvious choice for  $\hat{\mathbf{x}}_0$  is given by the mean of the prior distribution  $\boldsymbol{\mu}_{\mathbf{x}}$ . The initial value for  $\mathbf{P}_0$  is chosen to be the the covariance matrix of the prior distribution  $\boldsymbol{\Sigma}_{\mathbf{x}}$ .

### Gibbs Sampler

The Gibbs sampler is presented in subsection 3.5.2. The posterior distribution used for the generation of the samples is constructed by means of Bayes law shown in equation (3.1) with the likelihood function (3.4) and the Gaussian prior distribution presented in subsection 3.2.2. The bimodal version of the Gibbs sampler uses only the likelihood function (3.4). The prior information in this case is given by the use of only two material values.

The noise model is described by the covariance matrix  $\boldsymbol{\Sigma}_{\mathbf{v}}$  given by equation (4.10).

The required random samples for the Gaussian summary statistic used as prior information are provided by the random sample generators presented in subsection 3.2.1 and 4.1.1.

Since the Gibbs sampler is an iterative algorithm a starting point for the Markov chain is necessary. One obvious choice is the mean of the prior distribution  $\mathbf{x}_0 = \boldsymbol{\mu}_{\mathbf{x}}$ .

### 4.4.2 Summary and Notation of the Algorithms

Table 4.1 depict the abbreviations used for the different reconstruction algorithms, the different prior informations and the different state reduction techniques.

Here the term prior is referred to the incorporation of an prior distribution  $\pi(\mathbf{x})$  to the algorithm. If no prior knowledge by means of  $\pi(\mathbf{x})$  is incorporated, a proper state reduction technique is applied. The prior distribution  $\pi(\mathbf{x})$  as well as the projection matrix  $\mathbf{P}_{N_R}$  are assembled by means of the same random samples. Therefore the state reduction approach is an alternative way for the incorporation of prior knowledge. One exception is the bimodal Gibbs sampler. In this case the prior knowledge is given by the use of only two material values.

The construction of the Gaussian prior obtained from random samples is explained in detail in subsection 3.2.2. The state reduction approach based

Reconstruction algorithms	
OFOA	Optimal first order approximation
OSOA	Optimal second order approximation
LMAP	Linearized MAP estimator
LMAPnc	Non-constrained linearized MAP estimator
LML	Linearized ML type estimator
KF	Kalman filter
GS	Gibbs sampler
BGS	Bimodal Gibbs sampler
Prior	
Random samples	sample based prior used for the OA algorithms
Gaussian: $\boldsymbol{\mu}_{\mathbf{x}}, \boldsymbol{\Sigma}_{\mathbf{x}}$	Gaussian summary statistic from random samples
-	no prior by means of $\pi(\mathbf{x})$ is incorporated
State reduction (SR)	
-	no state reduction is applied
PCA	principle component analysis approach
INT	intuitive approach

**Table 4.1:** Abbreviations for the different reconstruction algorithms, the priors and the state reduction techniques.

on an principle component analysis (PCA) is presented in section 3.3 and the intuitive approach for a reduced state representation (INT) is shown in subsection 4.2.2. The same set of random samples is used for the PCA based state reduction, the assembly of the reconstruction matrix of the optimal approximation algorithms as well as for the construction of the Gaussian prior pdf. The available pattern generators are given by

- Pattern generators for arbitrary material distributions presented in subsection 3.2.1:
  - Rod type patterns.
  - Gauss type patterns.
- Pattern generators for pneumatic conveying flow patterns presented in subsection 4.1.1:
  - Horizontal conveying flow patterns.
  - Vertical downwards conveying flow patterns.

# 5 Case Studies for the Reconstruction Behaviour

In this chapter case studies for the reconstruction behaviour are presented. The different methods presented in the previous chapters are compared with respect to their capability of estimating the solid volume concentration discussed in section 4.3.

- The first section provides an overview about the implemented reconstruction algorithms and their specific setups.
- In the second section the simulation setup is explained in detail. This discussion contains issues such as the parameters of the forward map, the generation of the measurement data, the noise model and the prior knowledge incorporated to the reconstruction algorithms.
- The third section provides a detailed statistical analysis of the estimation results obtained with linear back projection type algorithms.
- In the next section estimation results of some particular non-linear iterative algorithms are presented in order to show their capability to reconstruct different material distributions.
- The last section of this chapter contains selected parameter studies. Here the influence of variations in parameters such as the number of electrodes, the measurement noise, the material value and the flow profile is analysed.

## 5.1 Reconstruction Algorithm Overview

This section is intended to provide an overview about the implemented reconstruction algorithms and their specific setups used for the case studies presented in this chapter. The available algorithms are listed in table 5.1.

Nr.	Algorithm	State reduction	Prior
1	OFOA	–	Random samples
2	OFOA	PCA	Random samples
3	OFOA	INT	Random samples
4	OSOA	–	Random samples
5	OSOA	PCA	Random samples
6	OSOA	INT	Random samples
7	LMAP	–	Gaussian: $\boldsymbol{\mu}_{\mathbf{X}}, \boldsymbol{\Sigma}_{\mathbf{X}}$
8	LMAP <sub>nc</sub>	–	Gaussian: $\boldsymbol{\mu}_{\mathbf{X}}, \boldsymbol{\Sigma}_{\mathbf{X}}$
9	LMAP	PCA	Gaussian: $\boldsymbol{\mu}_{\mathbf{X}}, \boldsymbol{\Sigma}_{\mathbf{X}}$
10	LMAP	INT	Gaussian: $\boldsymbol{\mu}_{\mathbf{X}}, \boldsymbol{\Sigma}_{\mathbf{X}}$
11	LML	PCA	–
12	LML	INT	–
13	KF	–	Gaussian: $\boldsymbol{\mu}_{\mathbf{X}}, \boldsymbol{\Sigma}_{\mathbf{X}}$
14	KF	PCA	–
15	KF	INT	–
16	GS	–	Gaussian: $\boldsymbol{\mu}_{\mathbf{X}}, \boldsymbol{\Sigma}_{\mathbf{X}}$
17	BGS	–	–

**Table 5.1:** Reconstruction algorithm overview.

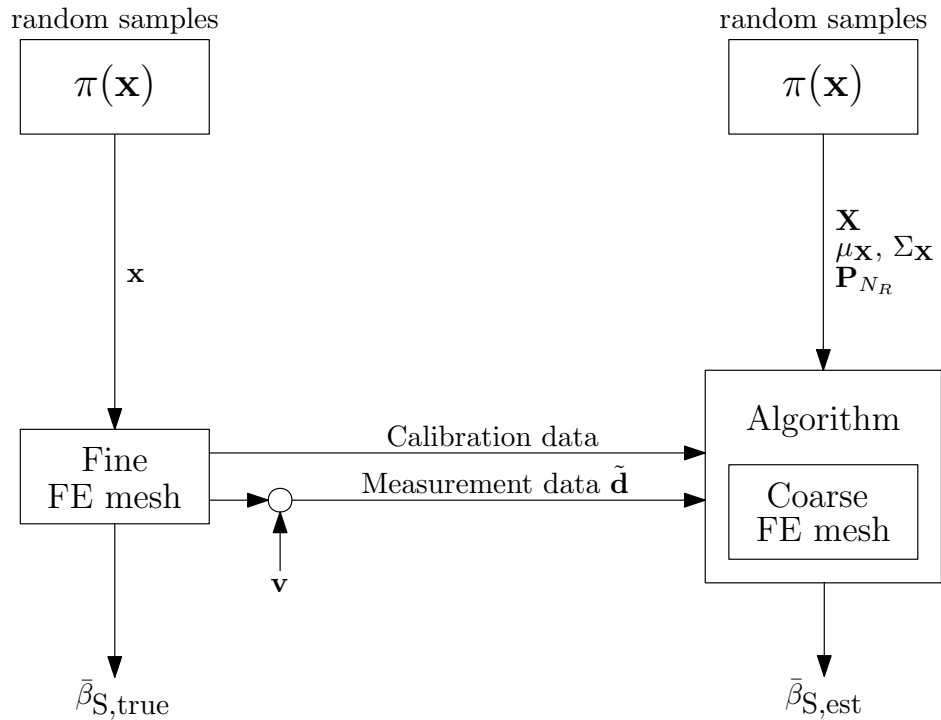
The table also lists information about the prior and the state reduction technique applied to the algorithm. Note that the abbreviations introduced in subsection 4.4.2 are used in this chapter.

An example for the notation used in this chapter is given by OSOA/PCA30. The first letters denote the algorithm by means of the abbreviations listed in table 4.1. The abbreviation after the slash denotes the applied state reduction approach. The number at the end indicates the size of the reduced state representation  $N_R$ . For this example the notation would stand for the optimal second order approximation algorithm using the PCA based state reduction approach with  $N_R = 30$ . If no state reduction approach is applied, the notation is given by OSOA/–.

## 5.2 Simulation Setup

In this section the general simulation setup is discussed in detail. Unless otherwise indicated, this specific setup is used for the simulation studies. In the later section 5.5 some particular parameter will differ from the setup presented here.

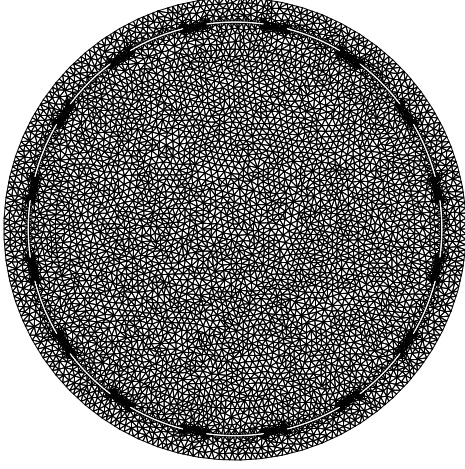
### 5.2.1 Simulation Procedure



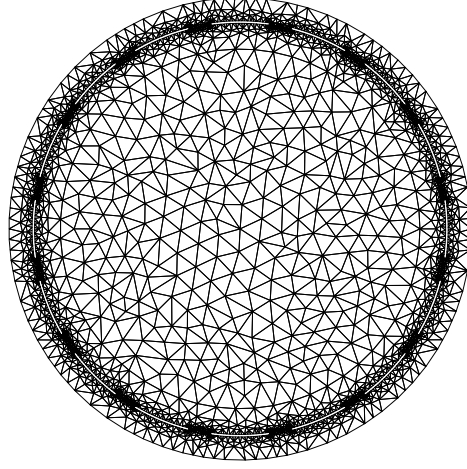
**Figure 5.1:** Flow chart of the simulation procedure.

Figure 5.1 depict the flow chart of the simulation procedure. The random sample generators presented in subsection 3.2.1 and 4.1.1 are used to generate the measurement data as well as the prior information.

To obtain the measurement data  $\tilde{\mathbf{d}}$ , a random sample  $\mathbf{x}$  is generated with the material value  $\varepsilon_{r,\text{true}} \propto \mathcal{U}(\varepsilon_{r,\text{min,true}}, \varepsilon_{r,\text{max,true}})$ . This sample is simulated by means of the forward map  $\mathbf{F}(\mathbf{x})$  presented in chapter 2. In this case a fine finite element (FE) mesh is used, depict in figure 5.2. This mesh uses a high number of finite elements to reduce the discretization error. The measurement data  $\tilde{\mathbf{d}}$  is given by the model output corrupted by additive white



**Figure 5.2:** Fine FE mesh used for the generation of the measurement data.



**Figure 5.3:** Coarse FE mesh used for the reconstruction algorithms.

Gaussian measurement noise  $\mathbf{v}$  with a certain signal to noise ratio (SNR). The indicated SNR is referred to the measurements for an empty ECT sensor.

Out of the random sample  $\mathbf{x}$  on the fine FE mesh, the true average solid volume concentration  $\bar{\beta}_{S,\text{true}}$  is calculated by means of equation (4.9). Here the material value  $\chi_{\max} = \varepsilon_{r,\max,\text{true}} - 1$  is used.

Given the calibration approach presented in section 2.5, also the measurements  $\tilde{\mathbf{d}}_{\text{empty}}$  and  $\tilde{\mathbf{d}}_{\text{full}}$  are generated on the fine FE mesh.

The random samples used as prior information for the algorithms are provided by the same random sample generators used to generate the measurement data. A material value of  $\varepsilon_{r,\text{prior}} \propto \mathcal{U}(\varepsilon_{r,\min,\text{prior}}, \varepsilon_{r,\max,\text{prior}})$  is used to generate the samples. This prior information contains:

- The matrix  $\mathbf{X}$  holding random samples to assemble the reconstruction matrix  $\mathbf{P}$  of the optimal approximation algorithms.
- The Gaussian summary statistic of the random samples given by  $\boldsymbol{\mu}_{\mathbf{X}}$  and  $\boldsymbol{\Sigma}_{\mathbf{X}}$ .
- The projection matrix  $\mathbf{P}_{N_R}$  of the prior based state reduction approach.

The forward map  $\mathbf{F}(\mathbf{x})$  used for the reconstruction algorithms is implemented by means of the coarse finite element mesh depict in figure 5.3. The use of a

reduced number of finite elements is necessary to reduce the computational costs. Hence the solution of the inverse problem can be done within an appropriate time.

Given the measurement data  $\tilde{\mathbf{d}}$  and the prior information, the reconstruction algorithms provide the estimate of the true material distribution  $\hat{\mathbf{x}}$ . The estimated average solid volume concentration  $\bar{\beta}_{S,\text{est}}$  is obtained by applying equation (4.9) on  $\hat{\mathbf{x}}$ . Here the material value  $\chi_{\text{max}} = \varepsilon_{r,\text{max,prior}} - 1$  is used.

### 5.2.2 Simulation Parameters

Considering the simulation procedure depict in figure 5.1 several parameters have to be specified. Figure 1.2 depict the scheme of the ECT sensor. The geometric dimensions of the ECT sensor used in this simulation study are given by:

- Radius of the shield:  $r_{\text{shield}} = 45$  mm.
- Outer radius of the process pipe:  $r_{\text{o,pipe}} = 40$  mm.
- Inner radius of the process pipe:  $r_{\text{i,pipe}} = 35$  mm.
- Thickness of the electrodes:  $d_{\text{elec}} = 0,5$  mm.

In general the number of electrodes is chosen to be  $N_{\text{elec}} = 16$  and they are equidistant arranged around the circumference of the ECT sensor.  $N_{\text{elec}}$  is varied for some particular simulations in the later section 5.5. For this reason it is mentioned at this point, that the cover angle  $\Delta\varphi_{\text{elec}}$  of the electrodes is given by

$$\Delta\varphi_{\text{elec}} = 0,7 \frac{360}{N_{\text{elec}}}, \quad (5.1)$$

for arbitrary  $N_{\text{elec}}$ .

Since the simulated measurement data  $\tilde{\mathbf{d}}$  is corrupted by additive white Gaussian noise the SNR has to be specified. For the standard simulation setup a signal to noise ratio of SNR= 60 dB is chosen.

The material values used for the generation of the random samples are chosen to be  $\varepsilon_{r,\text{min,true}} = \varepsilon_{r,\text{min,prior}} = 1$  and  $\varepsilon_{r,\text{max,true}} = \varepsilon_{r,\text{max,prior}} = 2$ .

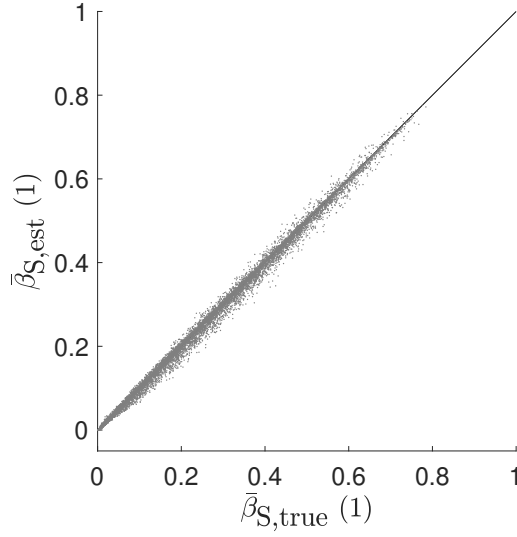


**Figure 5.4:** Exemplary scatter plot.

### 5.2.3 Representation of the Simulation Results

Given the procedure to obtain the true and the estimated value of  $\bar{\beta}_S$  the representation of the simulation results has to be discussed. Figure 5.4 depict a exemplary scatter plot holding the estimation results for the individual samples. Here  $\bar{\beta}_{S,true}$  is depict on the axis of abscissas and  $\bar{\beta}_{S,est}$  is depict on the axis of ordinates. In the case of  $\bar{\beta}_{S,est} = \bar{\beta}_{S,true}$  the samples would lie on a straight line with an angle of  $45^\circ$  and zero offset. This line is additionally depict in the scatter plots to indicate the nominal values.

For a statistical analysis of the estimation results the normalized mean square error (MSE) is calculated for the results. The normalized estimation error of the individual samples is given by

$$e_i = \frac{\bar{\beta}_{S,true} - \bar{\beta}_{S,est,i}}{\bar{\beta}_{S,true}}. \quad (5.2)$$

The normalized MSE is given by

$$\text{MSE} = \mathcal{E} \{e^2\} \approx \frac{1}{N} \mathbf{e}^T \mathbf{e}, \quad (5.3)$$

with the column vector  $\mathbf{e}$  holding the individual normalized estimation errors of the samples and the number of samples  $N$ . The normalization by means of  $\bar{\beta}_{S,true}$  is required to draw a comparison between the results for different material distributions. The true value  $\bar{\beta}_{S,true}$  can accept low values near to zero.

This causes large normalized errors  $e_i \gg$  for this particular samples. Thus, only samples with  $\bar{\beta}_{S,\text{true}} \geq 0,01$  are taken into account for the evaluation of the normalized MSE.

### 5.3 Simulation Study for Different Material Distributions

The following subsections depict the simulation results for some selected linear back projection type reconstruction algorithms with different configurations. Note, that not all available combinations of reconstruction algorithms and state reduction techniques are investigated since this would exceed the scope of this section. However the selected set of algorithms is chosen to provide a meaningful overview of the behaviour of the available techniques.

The following subsections present the simulation results for different material distributions. The title of each subsection indicates the material distribution used to generate the measurements. The random samples used as prior information corresponds in each case to the measurement data. The description of each plot shown in the following subsections indicates the reconstruction algorithm and the state reduction technique used to generate the particular plot. Therefore the notation discussed in section 5.1 is used.

#### 5.3.1 Simulation Results for Rod Type Samples

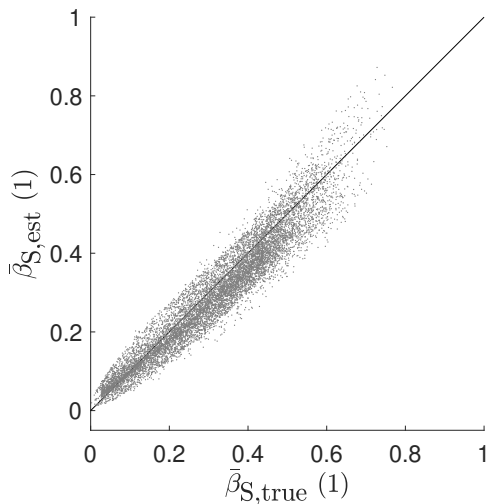


Figure 5.5: OFOA/—.

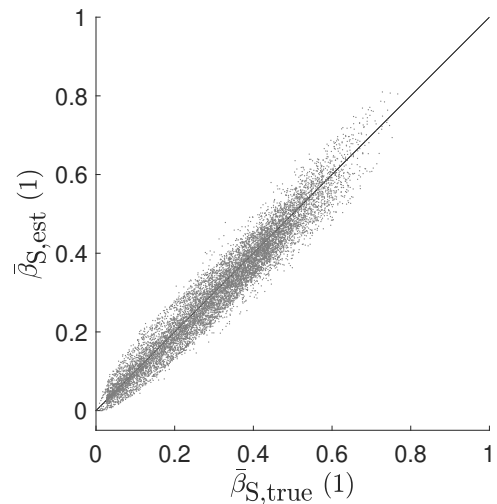


Figure 5.6: OSOA/—.

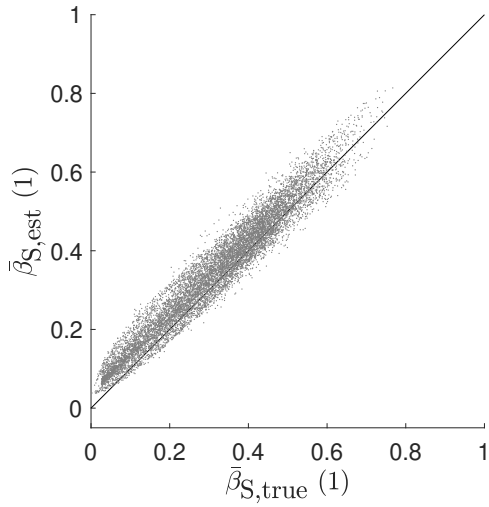


Figure 5.7: OSOA/PCA30.

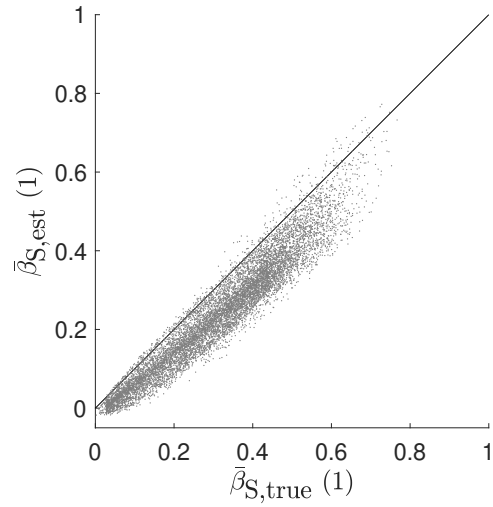


Figure 5.8: LMAPnc/-.

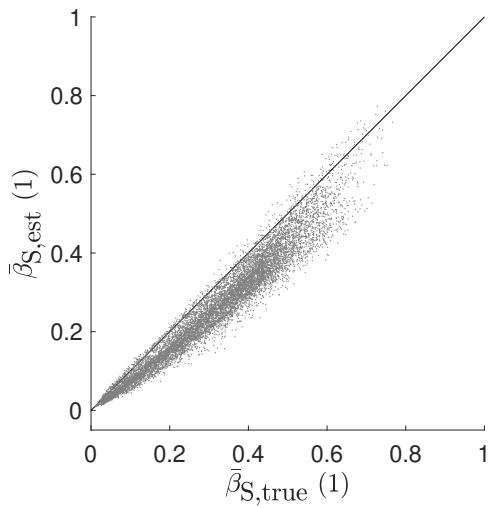


Figure 5.9: LMAP/-.

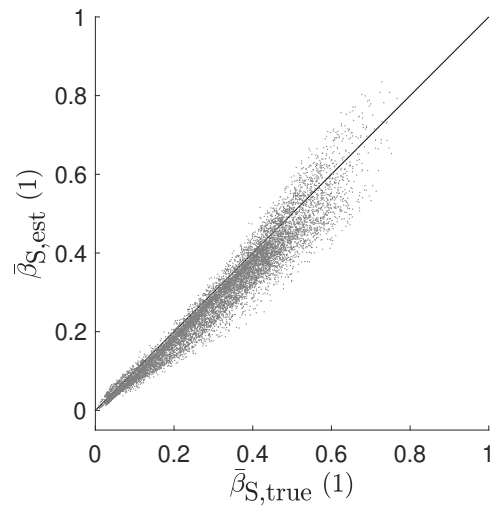


Figure 5.10: LMAP/PCA30.

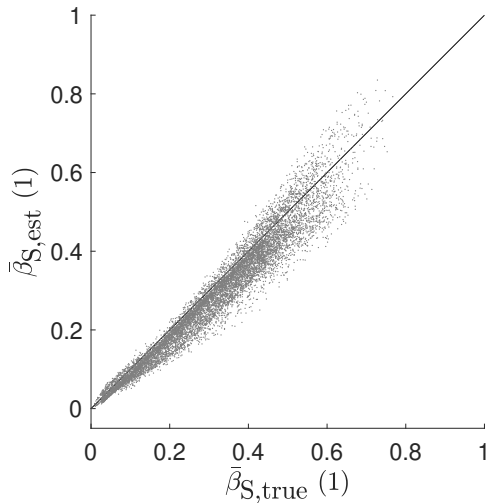


Figure 5.11: LML/PCA30.

Algorithm	MSE
OFOA/-	4,975e-02
OSOA/-	4,005e-02
OSOA/PCA30	1,654e-01
LMAPnc/-	1,270e-01
LMAP/-	5,041e-02
LMAP/PCA30	2,587e-02
LML/PCA30	2,586e-02

Table 5.2: Normalized mean square errors.

In this subsection the simulation results for rod type samples are provided. Figure 5.5 to 5.11 depict the scatter plots discussed in subsection 5.2.3 for different reconstruction algorithms. Table 5.2 depict the normalized MSE achieved with the individual algorithms. The following paragraphs discuss different issues regarding the simulation results.

### General Properties

Considering the simulation results presented in this subsection it becomes evident, that the samples are not covering the whole range of  $0 \leq \bar{\beta}_S \leq 1$ . Rod type samples are intended to provide a sample based prior for the reconstruction of rod type material distributions, as the name suggests. Since those rods are not filling the whole cross section of the ECT sensor, the true solid volume concentration  $\bar{\beta}_{S,\text{true}}$  is limited to certain values whereby  $\bar{\beta}_{S,\text{true}} < 1$  holds.

### Mean and Variance of the Samples

Rod type samples exhibit a large variance of the estimation results, especially for higher values of  $\bar{\beta}_{S,\text{true}}$ . The different LMAP and LML implementations show a lower variance for small values of  $\bar{\beta}_{S,\text{true}}$  compared to the OFOA and OSOA implementations. These high variances are caused by several reasons. For arbitrary material distribution the construction of a meaningful prior is difficult due to the large amount of possible material patterns within the ECT sensor. A further issue is given by the sharp material boundaries of the rod type samples. Due to the soft field behaviour of ECT, these sharp transitions between different materials are difficult to reconstruct.

Despite the large variance, the mean of the samples is approximately following the trend of the nominal values indicated by means of the straight line. Considering the LMAP and LML algorithms a slightly non linear course of the mean is evident.

The simulation results obtained by means of the OSOA/PCA30 algorithm depict in figure 5.7 exhibit a larger deviation from the nominal value for small values of  $\beta_S$ . The course of the mean converges to the nominal value for increasing volume concentrations. This circumstance is also evident by considering table 5.2, where the normalized mean square errors are depicted. Due to the larger deviation of the estimation result for small volume concentrations the MSE for the OSOA/PCA30 algorithm show the largest mean square errors due to the normalization of the MSE by  $\beta_{S,\text{true}}$ .

### Impact of State Constraints

Regarding the estimation results obtained with the LMAPnc/None algorithm depict in figure 5.8 it becomes obvious, that the incorporation of state constraints is reasonable. Estimation results with volume concentrations  $\beta_{S,\text{est}} < 0$  are obtained with this specific algorithm, which are not valid results. The incorporation of state constraints prevents the estimated material values to be  $\varepsilon_r < 1$  since  $\varepsilon_r = 1$  is the lower physical boundary of the relative permittivity. For estimates where  $\varepsilon_r < 1$  holds, the susceptibility  $\chi$  becomes negative. Considering equation (4.9), this circumstance can result in negative estimates for  $\bar{\beta}_{S,\text{est}}$ . This negative estimates are also the reason for the high value of the normalized MSE of the LMAPnc/– algorithm depict in table 5.2, since they occur for small values of  $\beta_{S,\text{true}}$ .

The optimal approximation algorithms are given by a simple matrix vector multiplication. For this reason it is not possible to incorporate state constraints to this kind of algorithms. Therefore optimal approximation algorithms are also able to achieve negative estimates for  $\bar{\beta}_{S,\text{est}}$ . Although this behaviour is possible, the simulation showed no negative results in this study.

### Impact of a Reduced State Space

Considering the different LMAP implementations, the PCA based state reduction approach involve an improvement of the estimation result. For an applied state reduction approach, the variance of the samples is significantly decreased for low values of  $\beta_{S,\text{true}}$ . The difference between the the LMAP/PCA30 and the LML/PCA30 algorithm is only given by the prior distribution  $\pi(\mathbf{x})$ , as discussed in subsection 3.4.2. Considering table 5.2 it is obvious, that these algorithms achieved very similar results. Therefore excluding the prior distribution  $\pi(\mathbf{x})$  from the algorithm has only a minor impact on the estimation results in the case of rod type random samples.

Although the application of the PCA based state reduction approach brings improvements for the LMAP estimator, the opposite effect occurs for the OSOA algorithm. Considering table 5.2 a significantly increased normalized MSE is obvious for the OSOA/PCA30 algorithm compared to the OSOA/– implementation. This increased error is given due to the fact, that the samples obtained with the OSOA/PCA30 algorithm show a large deviation from the nominal value for low volume concentrations  $\bar{\beta}_{S,\text{true}}$ .

## 5.3.2 Simulation Results for Gaussian Type Samples

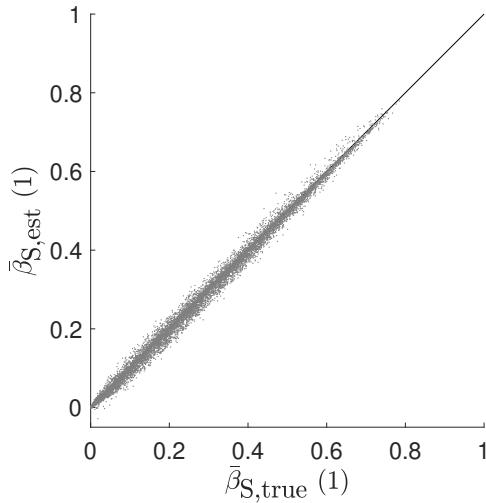


Figure 5.12: OFOA/—.

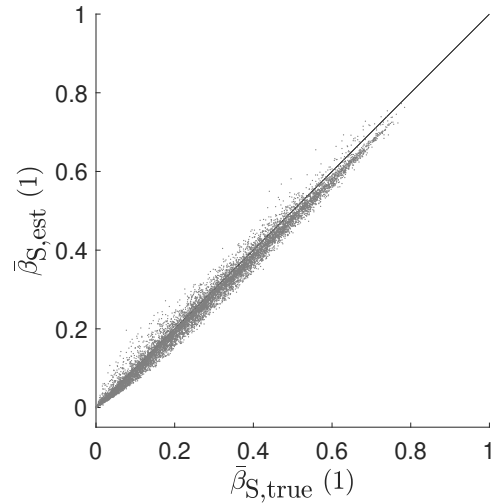


Figure 5.13: OSOA/—.

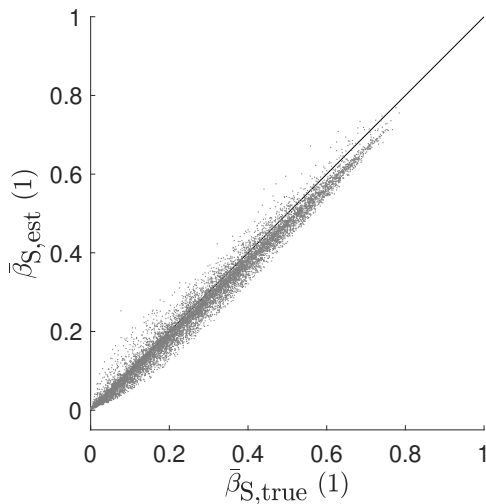


Figure 5.14: OSOA/PCA30.

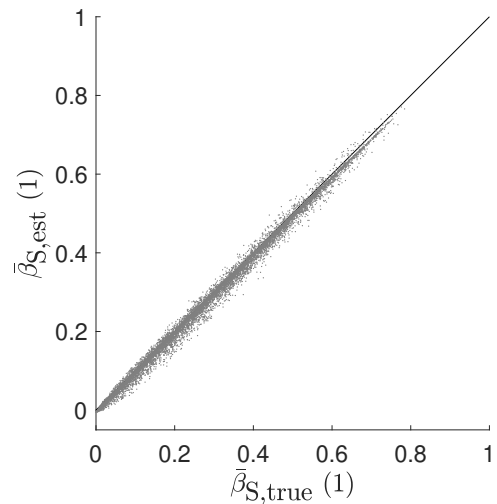


Figure 5.15: LMAPnc/—.

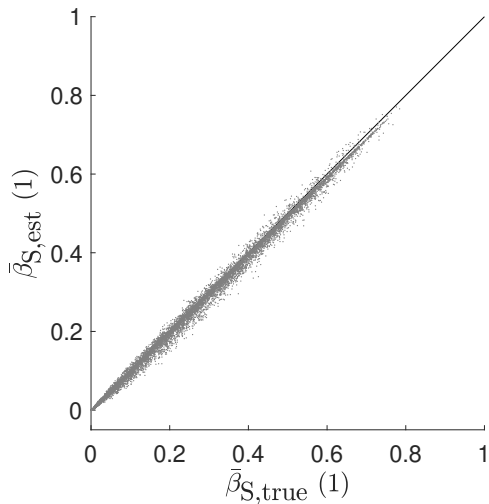


Figure 5.16: LMAP/–.

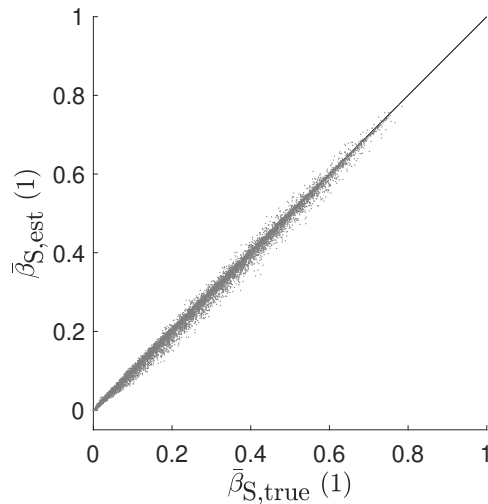


Figure 5.17: LMAP/PCA30.

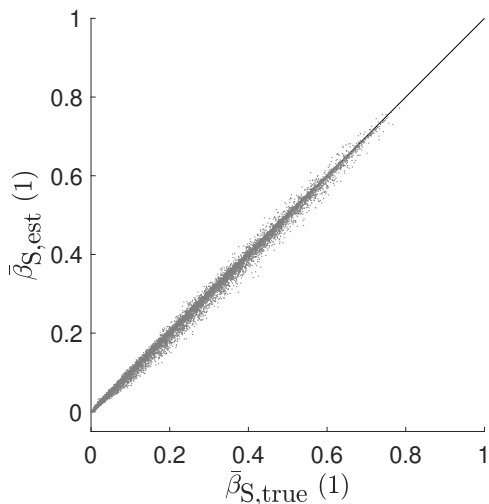


Figure 5.18: LML/PCA30.

Algorithm	MSE
OFOA/–	1,230e–02
OSOA/–	2,149e–02
OSOA/PCA30	3,729e–02
LMAPnc/–	1,338e–02
LMAP/–	6,005e–03
LMAP/PCA30	5,367e–03
LML/PCA30	5,373e–03

Table 5.3: Normalized mean square errors.

This subsection contains the simulations for Gaussian type samples. The simulation results obtained with the individual reconstruction algorithms are depict in figure 5.12 to 5.18. The normalized MSE for each algorithm is shown in table 5.3. Again the discussion is subdivided into different paragraphs, each dealing with different issues regarding the simulation results.

### General Properties

Also the Gaussian type samples are not covering the whole possible range of  $0 \leq \bar{\beta}_S \leq 1$ . This circumstance has the same reason like already explained for rod type samples in subsection 5.3.1.

### Mean and Variance of the Samples

Considering the simulation results it becomes obvious, that the variance of the samples is significantly decreased compared to the reconstruction results for rod type samples presented in subsection 5.3.1. Gaussian type samples also exhibit a multitude of possible material distributions. Though the smooth material transitions of the Gaussian samples are easier to reconstruct by means of the ECT. Considering the normalized MSE, this circumstance results in lower values compared to the results obtained for rod type samples.

Also the non linear course of the mean of the samples is significantly decreased compared to the results presented in 5.3.1. In this case the mean of the samples is following the trend of the nominal value over the whole range of  $\beta_S$ . Only the results of the OSOA algorithms are starting to differ from the nominal value for higher volume concentrations.

### Impact of State Constraints

For this simulation the LMAPnc/– algorithm as well as the OFOA/– and OSOA/– algorithms achieved negative estimation results with  $\beta_{S,est} < 0$ . This is given by the fact, that no state constraints are incorporated to these algorithms, like discussed in subsection 5.3.1. For this reason the OFOA/– and the LMAPnc/– algorithm achieved the highest MSE values for the reconstruction of Gaussian type material distributions.

### Impact of a Reduced State Space

Regarding the PCA based state reduction approach, the behaviour is similar to the results presented in subsection 5.3.1. The application of the reduced state space to the OSOA algorithm caused an increased normalized MSE compared to the OSOA/– algorithm. For the LMAP algorithms the state reduction involves a slightly improvement of the estimation result. In comparing the LMAP/PCA30 and LML/PCA30 algorithm it becomes obvious that the errors are again in the same scale.

### 5.3.3 Simulation Results for Horizontal Conveying Flow Samples

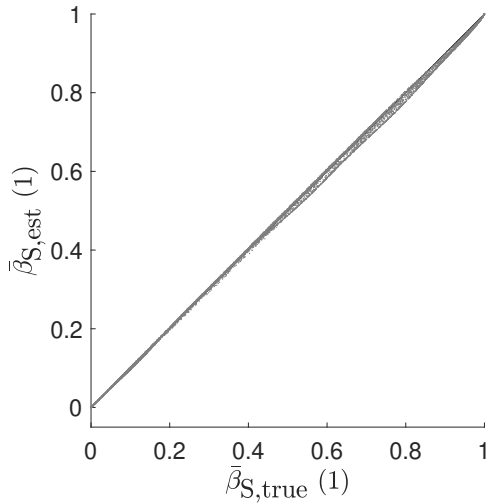


Figure 5.19: OSOA/—

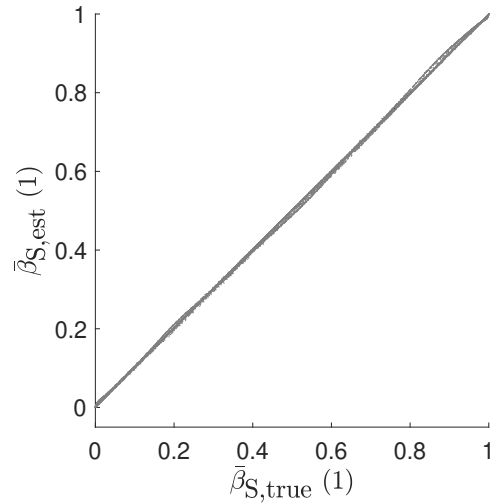


Figure 5.20: OSOA/PCA30

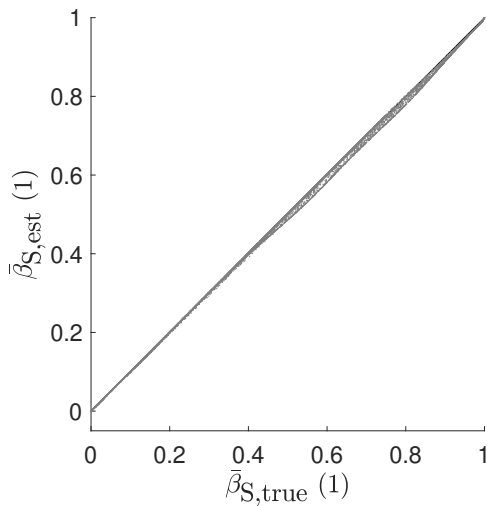


Figure 5.21: OSOA/INT30

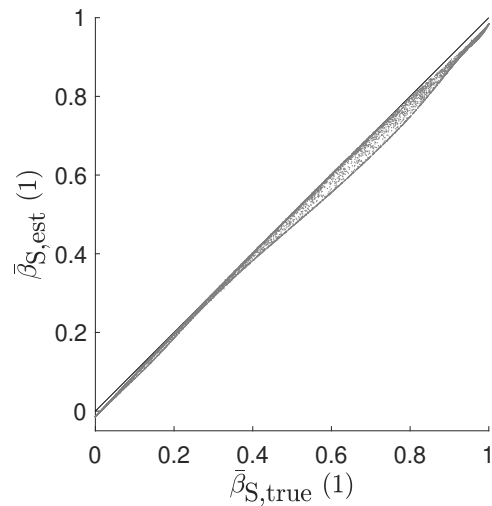


Figure 5.22: LMAPnc/—

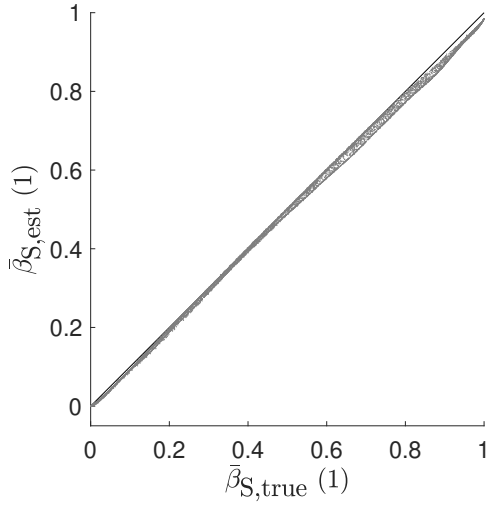


Figure 5.23: LMAP/-

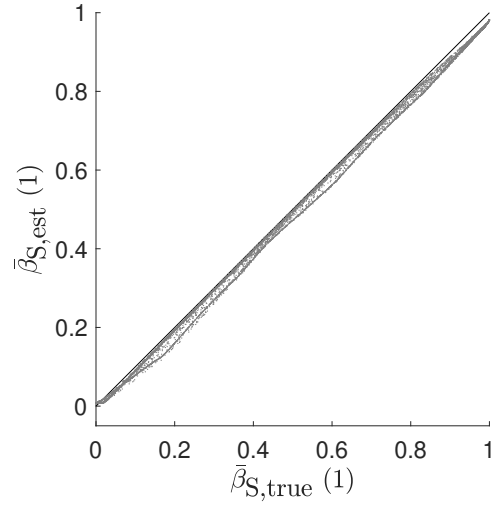


Figure 5.24: LMAP/PCA30

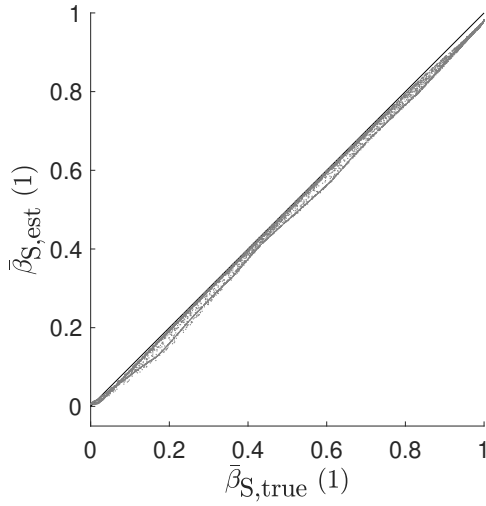


Figure 5.25: LMAP/INT30

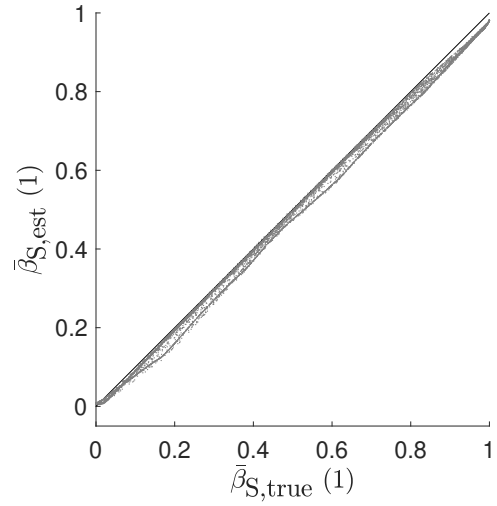


Figure 5.26: LML/PCA30

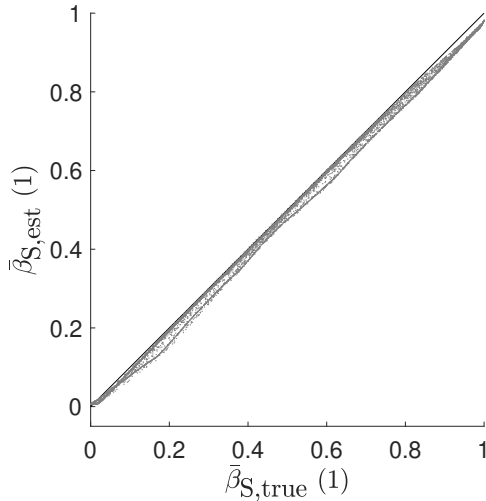


Figure 5.27: LML/INT30

Algorithm	MSE
OSOA/-	2,216e-04
OSOA/PCA30	2,114e-03
OSOA/INT30	1,835e-04
LMAPnc/-	2,120e-02
LMAP/-	6,299e-03
LMAP/PCA30	1,049e-02
LMAP/INT30	1,049e-02
LML/PCA30	1,041e-02
LML/INT30	1,041e-02

Table 5.4: Normalized mean square errors.

The simulation results for material patterns occurring in horizontal pneumatic conveying processes are discussed in this subsection. The individual results obtained with different algorithms are depicted in figure 5.19 to 5.27. The corresponding normalized MSE is depicted in table 5.4. In the following paragraphs different issues with respect to the simulation results are discussed in detail.

### **General Properties**

The prevailing material distributions in pneumatic conveying systems are reaching from dilute flow regimes to dense flow regimes like discussed in section 4.1. The random sample generators presented in subsection 4.1.1 were designed to simulate this occurring flow regimes. For this reason the volume concentration  $\bar{\beta}_{S,true}$  is covering the whole possible range of  $0 \leq \bar{\beta}_{S,true} \leq 1$  for this specific type of random samples.

### **Mean and Variance of the Samples**

By taking a look on the simulation results a further decrease of the variance is evident. This is given by the fact that meaningful prior knowledge is incorporated to the estimators since the structure of the flow regimes occurring in pneumatic conveying systems is well known.

The OSOA algorithms achieved remarkable results with respect to the normalized MSE. This is given by the circumstance that the multitude of possible material patterns is significantly reduced for flow patterns compared to arbitrary material patterns. For this reason the training of the optimal approximation algorithms for a set of data obtained from horizontal flow samples works especially well.

The mean of the samples is following in every case the nominal value of the volume concentration. For large values of  $\bar{\beta}_S$  the samples are starting to differ slightly from the nominal value for the different LMAP and LML implementations.

In each simulation result, more than one course with concentrated samples is evident. This is given by the fact that the same volume concentration can be achieved in different flow regimes. The volume concentration  $\bar{\beta}_S$  depends on the relative permittivity  $\varepsilon_r$  and the area of the domain. Therefore large areas with low permittivity values can exhibit the same  $\bar{\beta}_S$  then small areas with large permittivity values. The quality of the estimation result slightly de-

pends on the specific flow regime. A detailed investigation of the dependence of the estimation quality on the flow regime is done in subsection 5.3.5.

### Impact of State Constraints

Considering the results obtained with the LMAPnc/– algorithm, again negative estimates for  $\bar{\beta}_{S,\text{est}}$  are obtained for small values of  $\bar{\beta}_{S,\text{true}}$ . This is given by the fact that no state constraints are incorporated to the LMAPnc/– algorithm like already discussed in subsection 5.3.1. Although also no state constraints are incorporated to the OSOA algorithms, this estimators achieved valid results for this specific type of flow patterns.

### Impact of a Reduced State Space

The estimation results achieved by means of the algorithms using the intuitive state reduction approach are of comparative quality as the results achieved by means of the PCA state reduction approach. For the OSOA/INT30 algorithm the results are even more precise. This behaviour is given by the fact, that the PCA based basis vectors are showing smooth behaviour. The intuitive basis vectors in contrast can describe the sharp material transitions between the layers of the horizontal flow regimes.

### 5.3.4 Simulation Results for Vertical Downward Conveying Flow Samples

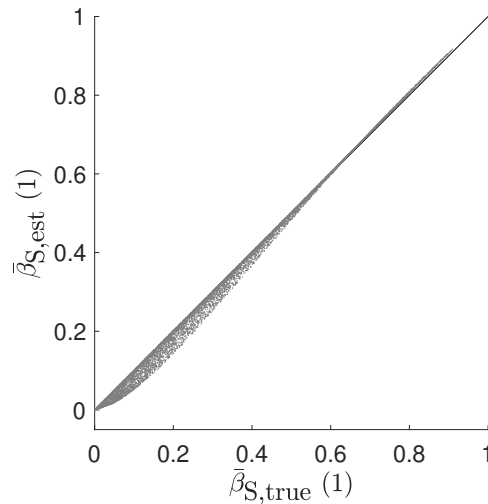


Figure 5.28: OSOA/–

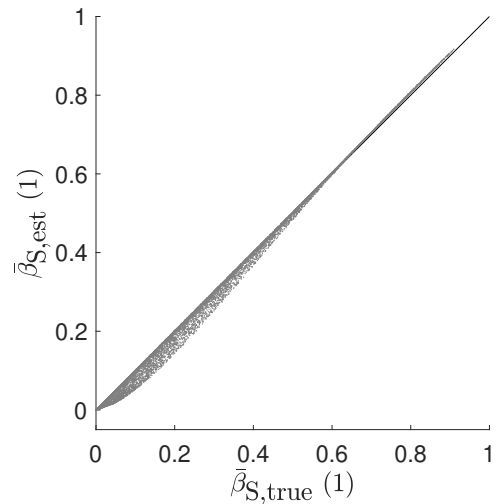
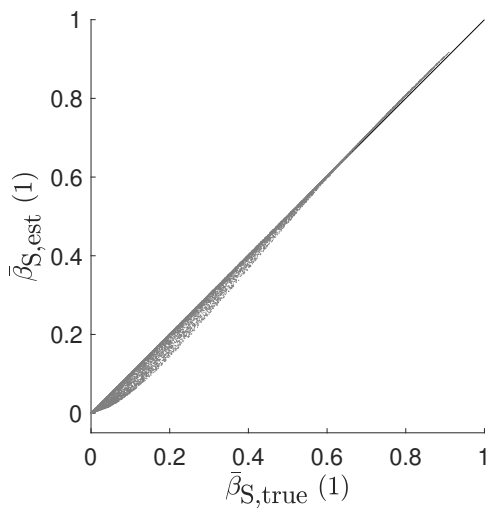
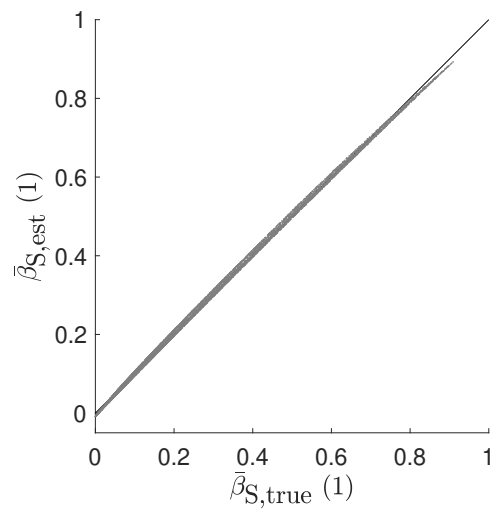
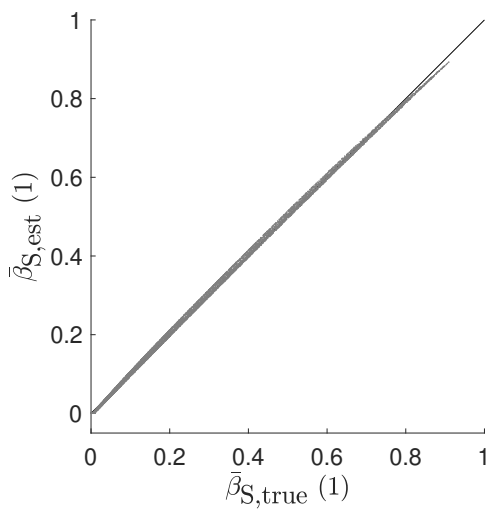
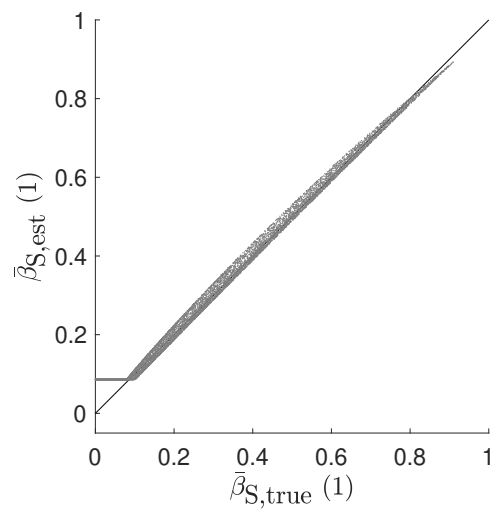
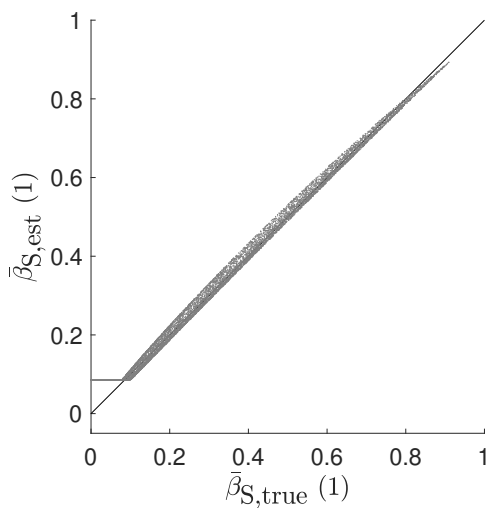
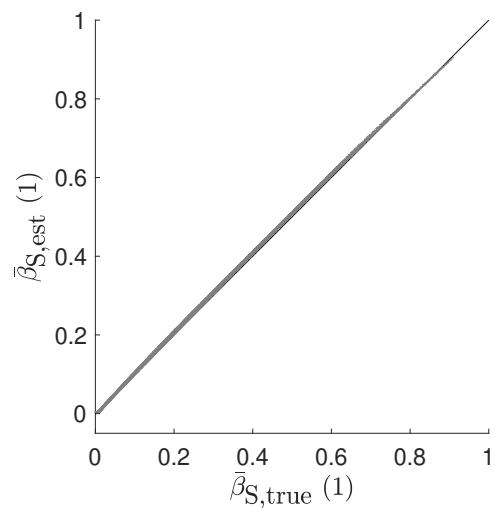
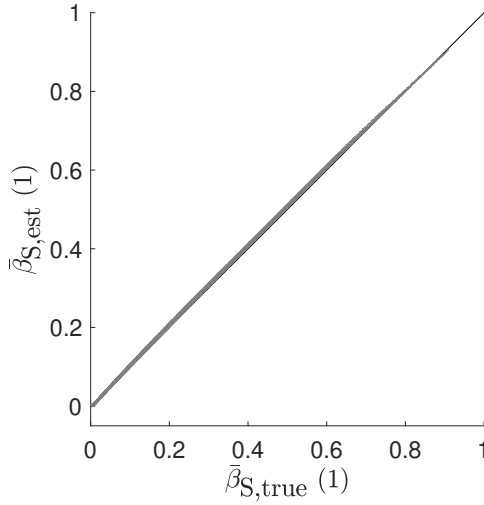


Figure 5.29: OSOA/PCA30

**Figure 5.30:** OSOA/INT30**Figure 5.31:** LMAPnc/-**Figure 5.32:** LMAP/-**Figure 5.33:** LMAP/PCA30**Figure 5.34:** LMAP/INT30**Figure 5.35:** LML/PCA30



**Figure 5.36:** LML/INT30

Algorithm	MSE
OSOA/–	3,194e–02
OSOA/PCA30	3,193e–02
OSOA/INT30	3,205e–02
LMAPnc/–	8,298e–03
LMAP/–	6,714e–03
LMAP/PCA30	1,016e+00
LMAP/INT30	1,016e+00
LML/PCA30	4,644e–03
LML/INT30	4,643e–03

**Table 5.5:** Normalized mean square errors.

In this subsection simulation results for material distributions occurring in vertical downward conveying are provided. The figures 5.28 to 5.36 depict the results achieved with different reconstruction algorithms. The normalized MSE achieved with each algorithm is depicted in table 5.5. The following discussion is subdivided into different paragraphs, each dealing with certain issues regarding the simulation results.

### General Properties

Also the random samples for vertical downward conveying material distributions are designed to simulate flow patterns. Still only approximately 90% of the range  $0 \leq \bar{\beta}_S \leq 1$  is covered by this specific type of random samples. This is due to the modeling of the material patterns by means of a centered Gaussian distribution. The range of the randomly selected standard deviation was chosen to generate samples approximately uniform distributed over the range of  $\bar{\beta}_{S,true}$ . This does not enable volume concentrations above a certain value.

### Mean and Variance of the Samples

The variance of the samples obtained by the OSOA algorithms is decreasing for higher values of  $\bar{\beta}_{S,true}$ . This behaviour is given by the fact, that the vertical downwards conveying flow patterns are modeled by means of centered Gaussian material distributions. The sensitivity within a ECT sensor is decreasing with the distance to the electrodes. Therefore a change of the material values in the center of the ECT sensor has only a small impact on the

measured capacitances. Due to the similarity of the measurement data for this samples, the matrix  $\tilde{\mathbf{D}}_a$  required for the assembly of the reconstruction matrix  $\mathbf{P}$  suffers from a poor condition number, given by equation (3.21). The normalization of the MSE by  $\bar{\beta}_{S,\text{true}}$  causes high errors for low values of  $\bar{\beta}_{S,\text{true}}$ . For this reason the estimation results exhibit higher mean square errors compared to the results for horizontal conveying flow samples presented in subsection 5.3.3 for this particular algorithm.

The difference between the LMAP/PCA30 and the LML/PCA30 or rather the LMAP/INT30 and the LML/INT30 is given by the prior distribution  $\pi(\mathbf{x})$  like discussed in subsection 3.4.2. For the LML implementations the prior pdf is given by  $\pi(\mathbf{x}) = 1$ . Therefore the prior distribution seems to cause a higher variance for this particular algorithms.

Considering the mean of the samples, a well matching with the nominal values is evident. Only the different LMAP implementation exhibit a small deviation from the nominal value for high values of  $\bar{\beta}_{S,\text{true}}$ .

### Impact of State Constraints

Considering the algorithms without state constraints, similar behaviour compared to the results presented in the previous subsections are evident. Again negative estimates for  $\bar{\beta}_{S,\text{est}}$  are obtained by means of the LMAPnc/- algorithm for low values of  $\bar{\beta}_{S,\text{true}}$ . Despite the absence of state constraints, the different OSOA implementations achieved valid results with  $\bar{\beta}_{S,\text{est}} > 0$  in every case.

### Impact of a Reduced State Space

The LMAP and LML algorithms with an applied state reduction approach are not able to provide estimation results for the volume concentration lower than an certain minimal value. This behaviour is given by the combination of lower state constrains and the reduced state representation. The basis vectors of the reduced state space are not able to describe material distributions with an low volume concentration without violating the state constraints. Obviously the incorporation of the prior distribution has an additional negative influence since this behaviour is significantly more pronounced for the LMAP algorithms. Due to the large errors for low values of  $\bar{\beta}_{S,\text{true}}$ , the LMAP/PCA30 and LMAP/INT30 algorithms exhibit the largest normalized MSE values.

Applying the intuitive as well as the PCA based state reduction approach provides results with a normalized MSE in the same scale. In this case PCA based basis vectors as well as the Gaussian material distributions exhibit smooth behaviour. Therefore the PCA based approach has no drawback with respect to the intuitive approach.

### 5.3.5 Detailed Error Analysis

In this section the estimation results for two particular simulation setups is analysed given by:

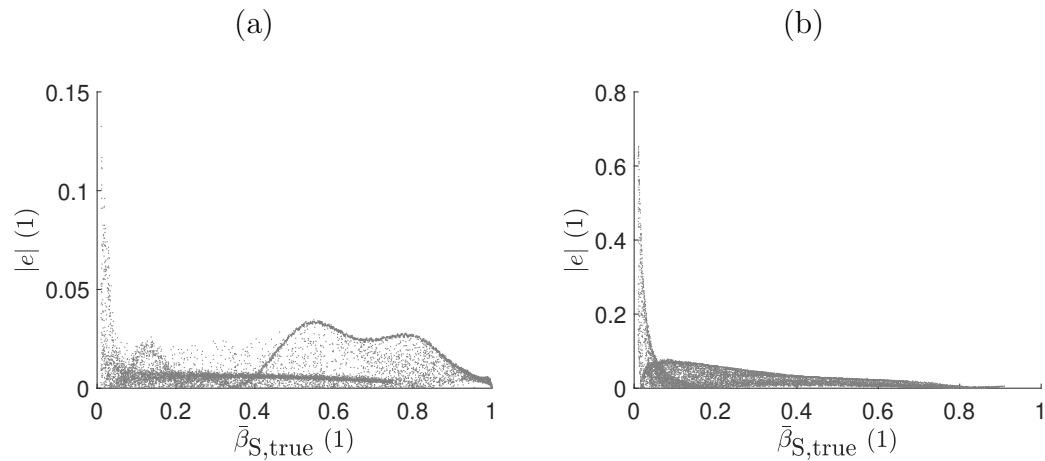
- OSOA/INT30 algorithm for horizontal conveying flow patterns depict in figure 5.21.
- LML/INT30 algorithm for vertical downwards conveying flow patterns depict in figure 5.36.

Considering this results it is evident, that the variance of the samples from the OSOA/INT30 algorithm seems to be slightly larger. The normalized mean square error depict in table 5.4 and 5.5 is still significantly lower for the OSOA/INT30. For this reason a detailed analysis of the normalized error  $e$  between the true and the estimated volume concentration  $\bar{\beta}_S$  given by equation (5.2) is done.

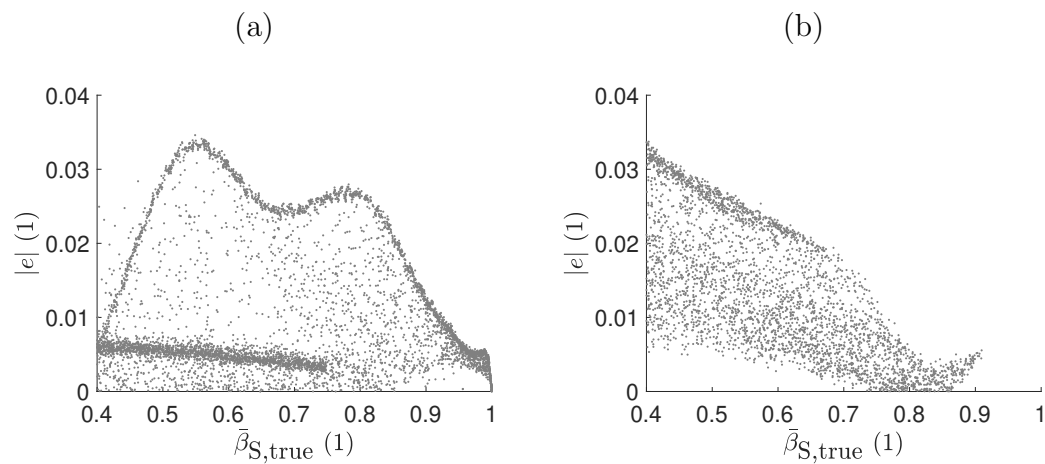
Figure 5.37 depict the absolute values of the errors for the individual samples obtained from the before mentioned algorithms. The error for low values of  $\bar{\beta}_{S,true}$  is for the LML/INT30 algorithm significantly larger compared to the OSOA/INT30 algorithm in the same range of  $\bar{\beta}_{S,true}$ .

Figure 5.38 depict a detailed view on the errors in the range  $0,4 \leq \bar{\beta}_{S,true} \leq 1$ . The errors of the LML/INT30 algorithm becomes smaller than those of the OSOA/INT30 algorithm from a certain value of  $\bar{\beta}_{S,true}$ . For this reason the variance of the LML/INT30 algorithm seems to be smaller. The large errors of this algorithm for low values of  $\bar{\beta}_{S,true}$  however have a large impact on the MSE.

Given the individual errors depict in figure 5.37 two different courses are evident in both cases, where the errors are concentrated. This can be attributed to the fact, that the same value of  $\bar{\beta}_S$  can be obtained by means of different flow regimes. The volume concentration depends on the relative permittivity and the area of the domain filled with the material, given by equation (4.9). The vertical downwards conveying flow patterns for example



**Figure 5.37:** Absolute values of  $e$ , (a) for horizontal conveying flow samples and the OSOA/INT30 algorithm, (b) for vertical downwards conveying flow samples and the LML/INT30 algorithm.



**Figure 5.38:** Detailed view on the absolute values of  $e$ , (a) for horizontal conveying flow samples and the OSOA/INT30 algorithm, (b) for vertical downwards conveying flow samples and the LML/INT30 algorithm.

are modeled by means of centred Gaussian material distributions with a random material value  $\varepsilon_r$  and a random standard deviation  $\sigma$ . Given this the same volume concentration  $\bar{\beta}_S$  can be achieved by an large value of  $\varepsilon_r$  and a small value of  $\sigma$  or reverse. Due to the spatial dependence of the sensitivity within the ECT sensor, this circumstance result in different estimation qualities for the same value of  $\bar{\beta}_S$  depending on the particular flow regime.

## 5.4 Simulations with Non-linear Iterative Algorithms

This section is indented to provide some reconstruction results obtained by means of non-linear iterative reconstruction algorithms. Due to the already remarkable results obtained with linear back projection type algorithms and the computational costs of non-linear, iterative algorithms, no comprehensive statistical analysis is implemented. Only the reconstruction results for a selected set of samples is presented in order to show the capability of these type of algorithms to reconstruct different material distributions.

### 5.4.1 Simulation Results

Figure 5.39 depict the reconstructed material distributions by means of the KF/– and the BGS/– algorithm as well as the true material distributions. One exemplary reconstruction result for each type of material distribution is shown. The different material distributions are given by:

- (a) A rod type sample.
- (b) A Gaussian type sample.
- (c) A horizontal conveying flow sample.
- (d) A vertical downward conveying flow sample.

In each case 20 iterations were performed by the algorithms to obtain the reconstructed material distributions presented in figure 5.39.

Considering the results it becomes evident, that the general pattern of the true material distribution was reconstructed in every case. Sharp transitions between materials are blurred due to the soft field behaviour of ECT.

Table 5.6 depict the resulting average volume concentrations given by equation (4.9). Since no comprehensive statistical analysis was implemented for

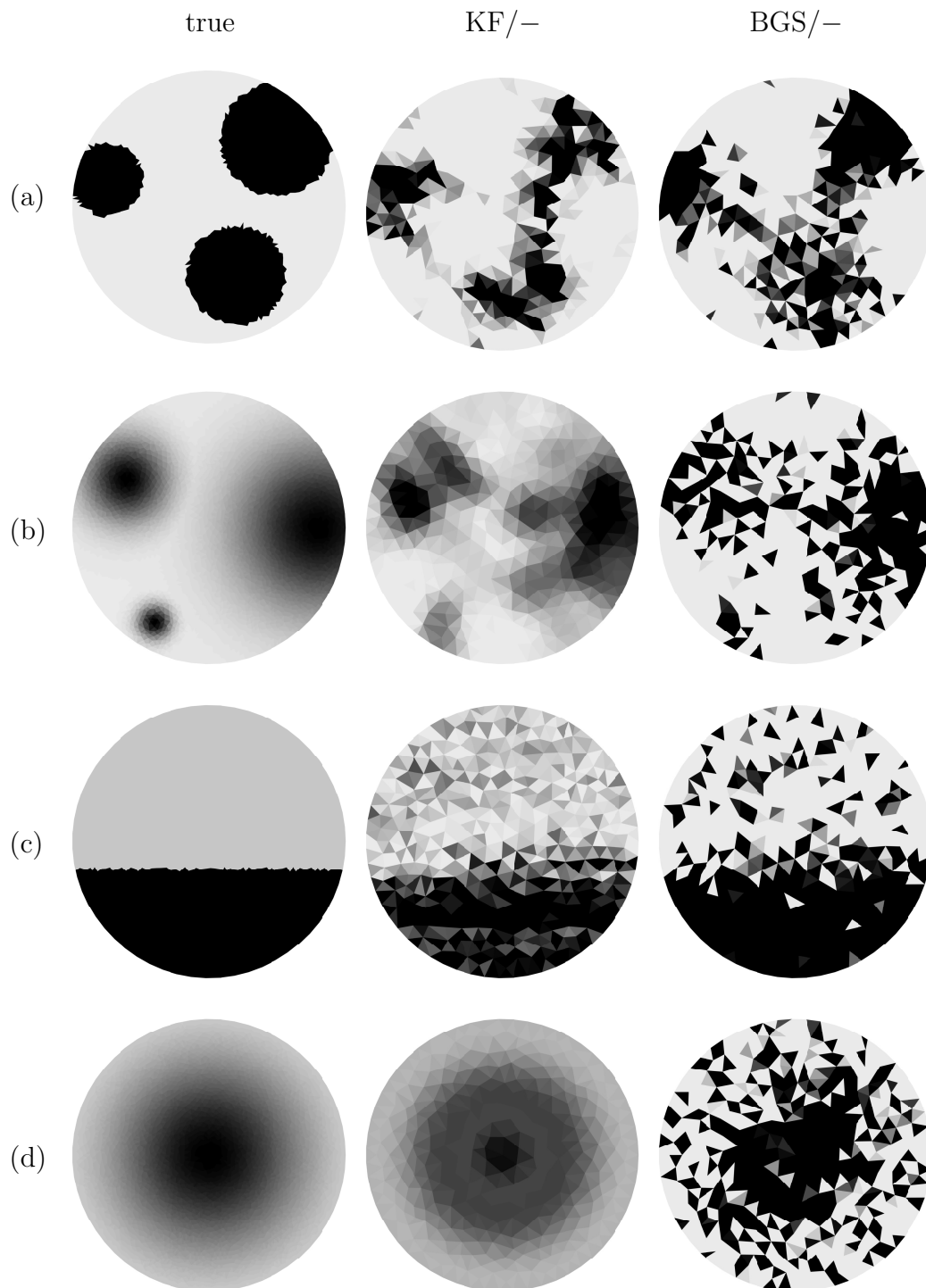


**Figure 5.39:** Reconstruction results for different material distributions obtained with non-linear iterative algorithms. (a) rod type samples, (b) Gaussian type sample, (c) horizontal conveying flow samples, (d) vertical downward conveying flow samples.

Pattern	$\bar{\beta}_{S,\text{true}}$	$\bar{\beta}_{S,\text{est}}$	
		KF/–	BGS/–
(a)	0,355	0,376	0,332
(b)	0,303	0,333	0,356
(c)	0,467	0,476	0,487
(d)	0,433	0,458	0,472

**Table 5.6:** True and estimated average volume concentrations for different material distribution.

non-linear iterative algorithms, comparing the results with those obtained by means of liner back projection type algorithms is not meaningful.

## 5.5 Selected Parameter Studies

This section contains selected case studies, where the influence of certain sensor and process parameters on the estimation result is investigated.

- In the first subsection the behaviour of ECT sensors with different numbers of electrodes is analysed.
- The second subsection contains an investigation of the impact of increased and decreased measurement noise on the estimated volume concentration  $\bar{\beta}_{S,\text{est}}$ .
- In the third section deviations of the material value  $\varepsilon_r$  are investigated. Therefore the material values used to generate measurements differ from the material values used as prior information.
- The last subsection provides an investigation of differing flow profiles with respect to the flow profiles used to generate the prior.

### 5.5.1 Variation of the Number of Electrodes

This subsection contains a study of the behaviour of the ECT sensor with different numbers of electrodes  $N_{\text{elec}}$ . The simulations are implemented for horizontal and vertical downward conveying flow samples with an selected set of reconstruction algorithms. The set of algorithms is chosen to provide a meaningful overview of the behaviour of the available techniques. Except the number of electrodes  $N_{\text{elec}}$ , the simulation setup discussed in section 5.2 is used for the studies in this subsection.

## Simulation Results

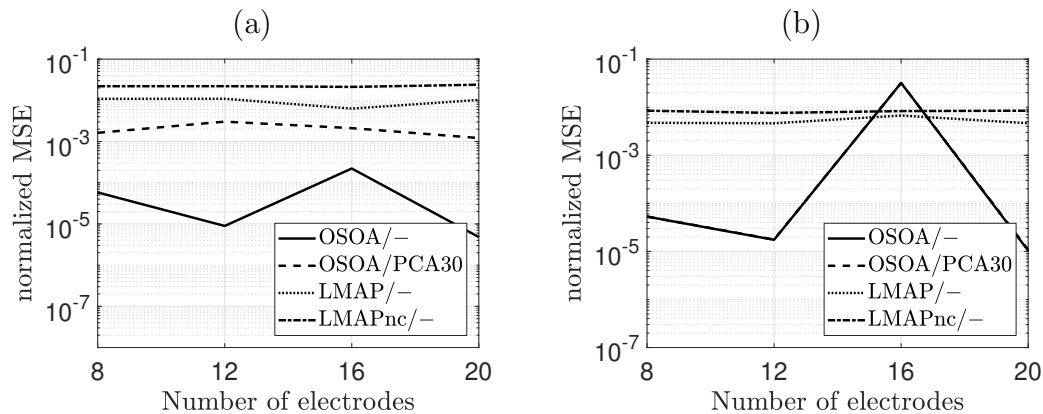


**Figure 5.40:** Normalized mean square errors for different numbers of electrodes, (a) horizontal conveying flow patterns, (b) vertical downward conveying flow patterns.

Figure 5.40 depicts the normalized mean square errors of a selected set of reconstruction algorithms for different numbers of electrodes. Figure 5.40(a) depict the results for horizontal conveying flow patterns and 5.40(b) depicts the simulation results for vertical downward conveying flow patterns. The simulation was implemented for  $N_{\text{elec}} = \{8, 12, 16, 20\}$ .

For horizontal conveying material patterns  $N_{\text{elec}}$  has a negligible small impact on the estimation results obtained with the different LMAP algorithm implementations. However the quality of the estimation result achieved with the OSOA/- algorithm show a dependence on  $N_{\text{elec}}$ . The largest MSE was obtained for  $N_{\text{elec}} = 16$ . For both, higher and smaller numbers than  $N_{\text{elec}} = 16$  the normalized MSE is decreasing for the OSOA/- algorithm. Applying the PCA based state reduction approach to the OSOA algorithm results in a similar behaviour like for the LMAP implementations. The dependence of the estimation result on  $N_{\text{elec}}$  is significantly decreased in the case of the the OSOA/PCA30 algorithm.

For vertical downward conveying flow patterns depict in figure 5.40(b), the different LMAP implementations show similar behaviour like for horizontal conveying flow patterns. The impact of  $N_{\text{elec}}$  on the estimation results is marginal. The trend of the normalized MSE with respect to  $N_{\text{elec}}$  achieved with the OSOA/- algorithm exhibit the same behaviour like for horizontal conveying flow patterns. Again the error shows a maxima for  $N_{\text{elec}} = 16$ .

This characteristic of the OSOA/– algorithm is even more pronounced for vertical downward conveying flow patterns. A further interesting circumstance is given by the fact, that the trends of the OSOA algorithms seems to be congruent in this case. This characteristic corresponds to the simulation results presented in subsection 5.3.4, since the OSOA/– and the OSOA/PKA30 algorithm achieved very similar results in the case of vertical downward conveying flow patterns.

### 5.5.2 Impact of Measurement Noise

In this subsection the influence of measurement noise on the estimation result is analysed. The simulation is implemented for horizontal and vertical downward conveying flow patterns for different signal to noise ratios. The results are provided for a meaningful set of reconstruction algorithms. Except for the value of the SNR, the simulation setup presented in 5.2 was used to obtain the simulation results provided in this subsection.

#### Simulation Results

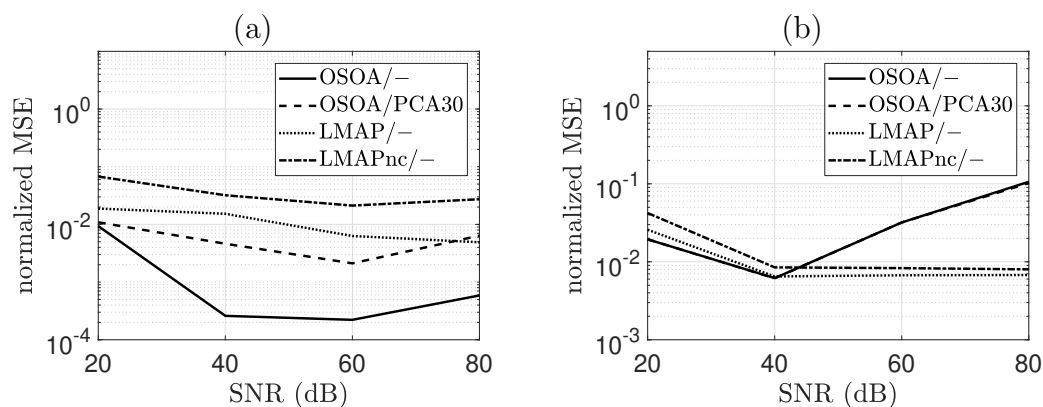


**Figure 5.41:** Normalized mean square errors for different signal to noise ratios, (a) horizontal conveying flow patterns, (b) vertical downward conveying flow patterns.

The normalized mean square errors of a selected set of reconstruction algorithms for different noise levels is depicted in figure 5.41. Figure 5.41(a) depicts the results for horizontal conveying flow patterns and 5.41(b) depicts the simulation results for vertical downward conveying flow patterns. The simulation was implemented for  $\text{SNR} = \{20, 40, 60, 80\}$  dB.

For horizontal conveying flow patterns, the achieved normalized MSE of all investigated algorithms are decreasing with increasing noise levels until a value of SNR = 60 dB. A further increase of the SNR to a value of 80 dB results in a increased MSE in the case of the OSOA/–, the OSOA/PCA30 and the LMAPnc/– algorithm. For the OSOA implementations, this behaviour can be traced back to the poor condition number of the matrix  $\tilde{\mathbf{D}}_a$  like discussed in subsection 5.3.4. These kind of algorithms require a certain variation in the measurement data.

For vertical downward conveying flow patterns, the MSE achieved with the different LMAP implementations is decreasing with an increasing SNR. However the decrease of the normalized MSE is negligible small for signal to noise ratios larger than 40 dB. Also in the case of vertical downward conveying flow patterns the different OSOA implementations exhibit the characteristic of an increasing error for SNR > 40 dB. This is again due to the before mentioned reason. Also in this case that the trend of the OSOA implementations seems to be congruent corresponding to the simulation results presented in subsection 5.3.4.

### 5.5.3 Variation of the Material Values

In this subsection the influence of a deviation of the true material value from the material value used as prior information is investigated. Two different cases are analysed:

- A constant true material value higher than the prior material value  $\varepsilon_{r,\max,\text{true}} = 2,5$  and  $\varepsilon_{r,\max,\text{prior}} = 2$ .
- A constant true material value lower than the prior material value  $\varepsilon_{r,\max,\text{true}} = 1,5$  and  $\varepsilon_{r,\max,\text{prior}} = 2$ .

The simulation results in this subsection are presented for a small set of reconstruction algorithms, chosen to provide a meaningful overview of the characteristics of different algorithm setups. The results are only presented for vertical downward conveying flow patterns. This is reasonable since the reconstruction algorithms are using the strongest prior information for this specific type of flow pattern. Therefore the variation of the material values should show the strongest impact on the estimation results.

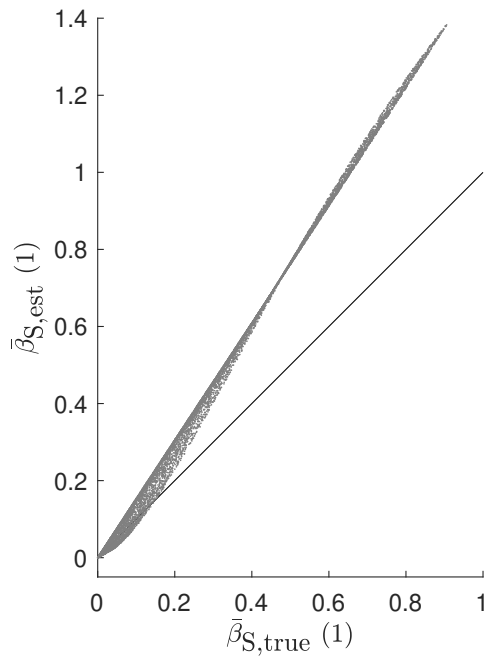


Figure 5.42: OSOA/–

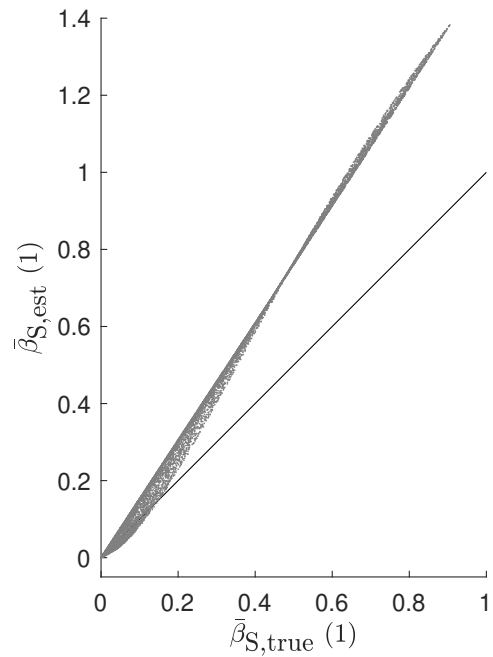


Figure 5.43: OSOA/PCA30

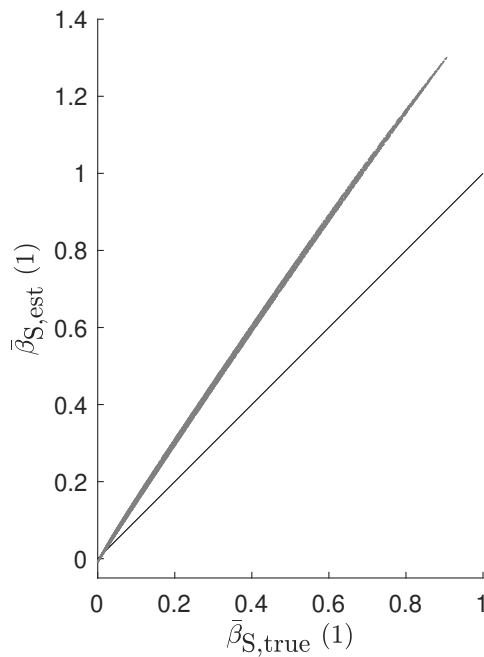


Figure 5.44: LMAPnc/–

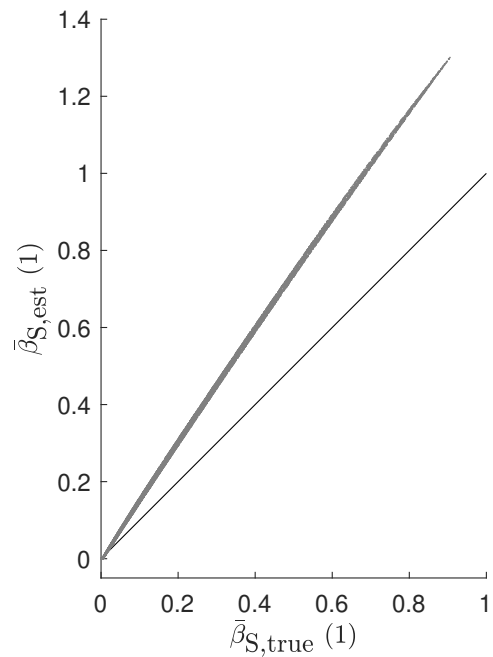


Figure 5.45: LMAP/–

### Simulation Results: Constant True Material Value Higher than the Prior Material Value

The figures 5.42 to 5.45 depict the simulation results for different reconstruction algorithms. In this case the true material value material value was

higher than the prior material value. The material values were chosen to be  $\varepsilon_{r,\max,\text{true}} = 2,5$  and  $\varepsilon_{r,\max,\text{prior}} = 2$  for this specific simulations.

Considering the results it is obvious that the true values of the volume concentration  $\bar{\beta}_{S,\text{true}}$  were overestimated due to the higher permittivity of the true material distributions. For this reason estimated volume concentrations with values of  $\bar{\beta}_{S,\text{est}} > 1$  were obtained.

The variance of the samples obtained with the different algorithms is very similar to the simulation results presented in subsection 5.3.4. The samples obtained with the LMAP implementations are following again a straight line with a low variance, but the slope is significantly larger. Due to the absence of state constraints, the LMAPnc/– algorithm achieved again estimation results lower than 0 for small values of  $\bar{\beta}_{S,\text{true}}$ . Despite the absence of state constraints, no negative estimates were obtained by means of the different OSOA implementations.

Considering the slopes of the courses it is obvious, that they are significantly larger with respect to the nominal values. Since the fundamental behaviour of the reconstruction algorithm is almost unchanged, the main reason for the overestimation of  $\bar{\beta}_{S,\text{true}}$  seems to be given by the use of the wrong material value in equation (4.9). To prove this statement two steps are necessary. Firstly the slope of the samples  $g$  is determined. Therefore a straight line is fitted to the samples in a least squares sense. Table 5.7 depict the slope  $g$  of the simulation results for the different reconstruction algorithms. For the second step equation (4.9) has to be considered. Due to the assumption that the overestimation is caused by the differing material values in the computation of  $\bar{\beta}_S$  the ratio

$$\frac{\chi_{\max,\text{true}}}{\chi_{\max,\text{prior}}} = \frac{\varepsilon_{r,\max,\text{true}} - 1}{\varepsilon_{r,\max,\text{prior}} - 1} = \frac{2,5 - 1}{2 - 1} = 1,5. \quad (5.4)$$

is evaluated. By considering the slopes of the samples, it becomes obvious that they are approximately given by this ratio. Therefore, the overestimation of the true values of  $\bar{\beta}_{S,\text{true}}$  is mainly caused by the use of the wrong material value in equation (4.9). The incorporation of a wrong material value in the prior information has only a minor impact on the estimation results.

Algorithm	$g$
OSOA/–	1,5655
OSOA/PCA30	1,5656
LMAPnc/–	1,4590
LMAP/–	1,4596

**Table 5.7:** Slopes of the samples for different algorithms.

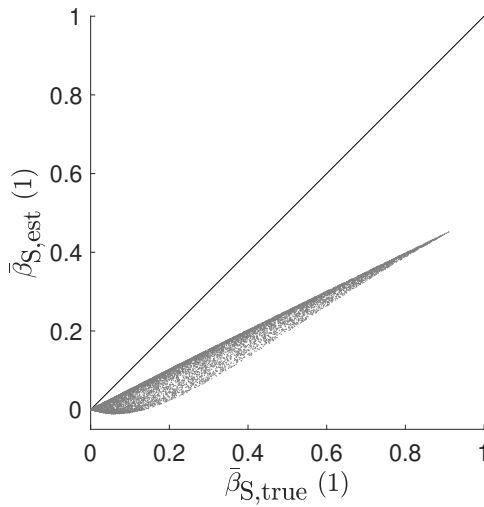


**Figure 5.46:** OSOA/–

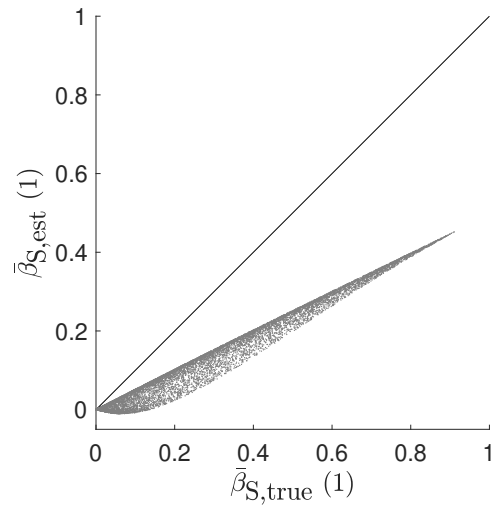


**Figure 5.47:** OSOA/PCA30

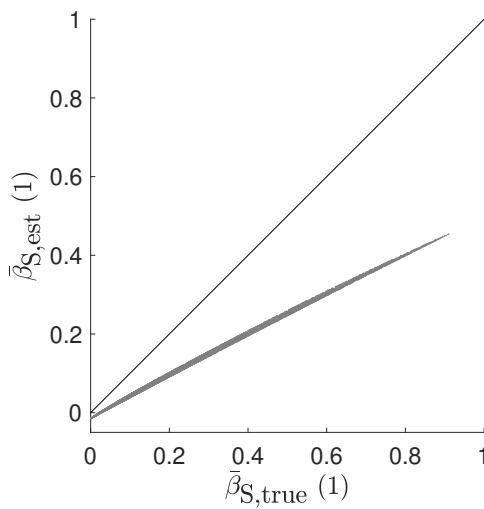


**Figure 5.48:** LMAPnc/–

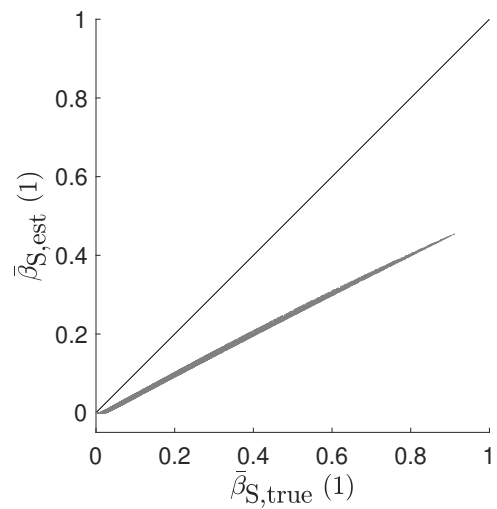


**Figure 5.49:** LMAP/–

Algorithm	$g$
OSOA/–	0,5107
OSOA/PCA30	0,5107
LMAP <sub>nc</sub> /–	0,5143
LMAP/–	0,5184

**Table 5.8:** Slopes of the samples for different algorithms.

### Simulation Results: Constant True Material Value Lower than the Prior Material Value

The simulation results for different reconstruction algorithms are depicted in figure 5.46 to 5.49. The provided results are obtained for a true material value lower than the prior material value. The maximal values were chosen to be  $\varepsilon_{r,\max,\text{true}} = 1,5$  and  $\varepsilon_{r,\max,\text{prior}} = 2$  for these specific simulations.

The single samples are following approximately a straight line with a variance in the same scale as the results presented in subsection 5.3.4. Though a true material value  $\varepsilon_{r,\max,\text{true}}$  lower than the prior material value  $\varepsilon_{r,\max,\text{prior}}$  results in an underestimation of  $\bar{\beta}_{S,\text{true}}$ . This is recognisable in a too small slope of the samples compared to the line indicating the nominal value of  $\bar{\beta}_{S,\text{est}} = \bar{\beta}_{S,\text{true}}$ .

Since no constraints are incorporated, the different OSOA implementations achieved negative estimates with  $\bar{\beta}_{S,\text{est}} < 0$ . An interesting characteristic of the optimal approximation algorithms is given by the non-linear course of the lower bound of the samples. Due to this non-linearity and the lower slope of the samples the estimated value  $\bar{\beta}_{S,\text{est}}$  is decreasing in a certain range for increasing values of  $\bar{\beta}_{S,\text{true}}$  for some specific samples.

The samples obtained with the different LMAP implementations are arranged in a straight line with a low variance. This behaviour is corresponding to the results presented in subsection 5.3.4. Due to the underestimation of the result the mean of the samples exhibit a negative offset. For this reason the LMAP<sub>nc</sub>/– algorithm achieved negative estimates with  $\bar{\beta}_{S,\text{est}} < 0$  for low values of  $\bar{\beta}_{S,\text{true}}$  due to the absence of state constraints. Because of the incorporation of state constraints the LMAP/– algorithm provides a constant estimate with  $\bar{\beta}_{S,\text{est}} = 0$  for a  $\bar{\beta}_{S,\text{true}}$  lower than a certain value.

There are minor differences in the characteristics of the reconstruction algorithms compared to the result presented in subsection 5.3.4. However the

main issue is given by the wrong slope of the samples. For this reason the main cause of the error seems to be given again by the use of the wrong material value in the calculation of  $\bar{\beta}_S$  given by equation (4.9). To prove this statement again the slopes of the samples  $g$  are determined in an least squares sense. The resulting slopes are depict in table 5.8 for different algorithms. In the next step the ratio

$$\frac{\chi_{\max, \text{true}}}{\chi_{\max, \text{prior}}} = \frac{\varepsilon_{r, \max, \text{true}} - 1}{\varepsilon_{r, \max, \text{true}} - 1} = \frac{1,5 - 1}{2 - 1} = 0,5, \quad (5.5)$$

is calculated, corresponding to the procedure applied to the previous results. Also in this case the slopes of the samples are approximately given by this ratio. Therefore the main issue in the estimation of  $\bar{\beta}_S$  is given by the use of the wrong material value in equation (4.9). The wrong material value in the prior information has again only a minor impact on the estimation results.

#### 5.5.4 Variations in the Flow Profile

This subsection provides an investigation of the impact of variations in the flow profile on the estimation result. Variations of both, horizontal conveying and vertical downward conveying flow patterns are implemented. Though the prior information is still given by means of the random samples presented in 4.1.1 to analyse the robustness of the algorithms against these variations. The results are presented for a subset of available reconstruction algorithms, chosen to provide a meaningful overview.

##### Variation of Horizontal Conveying Flow Patterns

Investigations of flow patterns in horizontal pneumatic conveying have shown, that the transition between the bottom layer and the dilute flow in the upper layer is often given by dune like shapes [35]. Figure 5.50 depicts two exemplary samples for those modified flow patterns. The general flow regimes are still given by those presented in section 4.1. The only difference is the shape of the transition between the layers. To randomly generate samples for those modified patterns also the transition curve is selected randomly. The transition is given by a curved section whereby the center and the radius of the corresponding circle is generated by random.

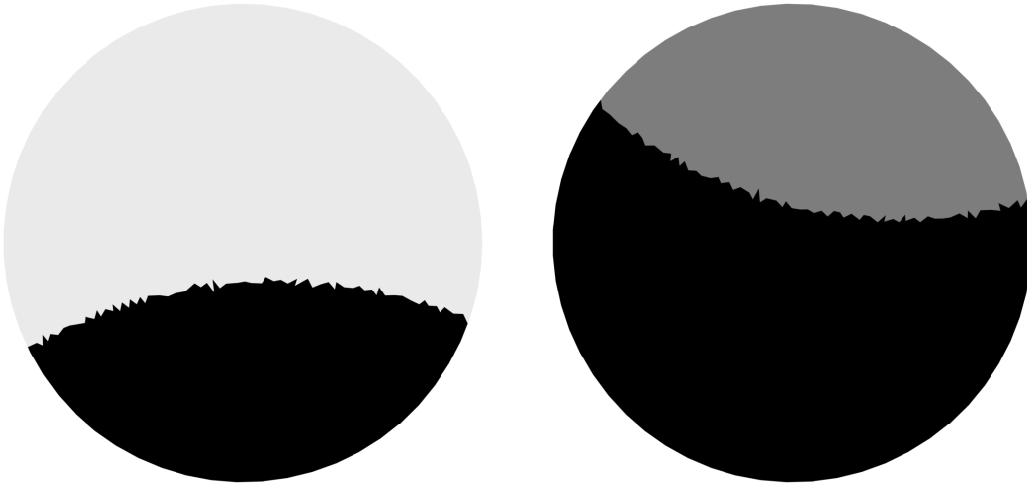


Figure 5.50: Exemplary samples for varied horizontal flow patterns.

### Simulation Results for Varied Horizontal Conveying Flow Patterns

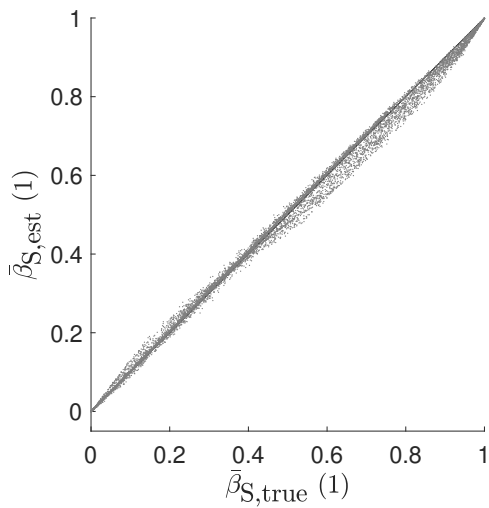


Figure 5.51: OFOA/—

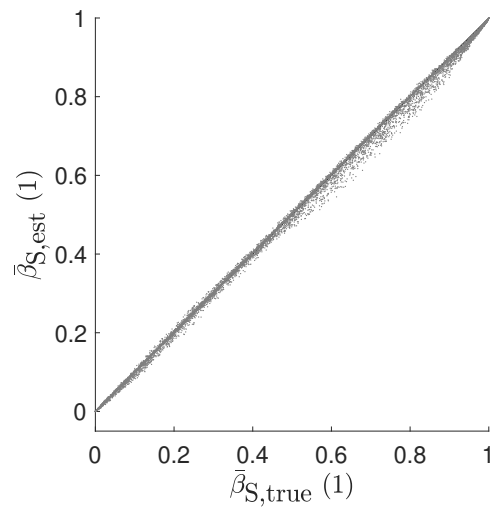
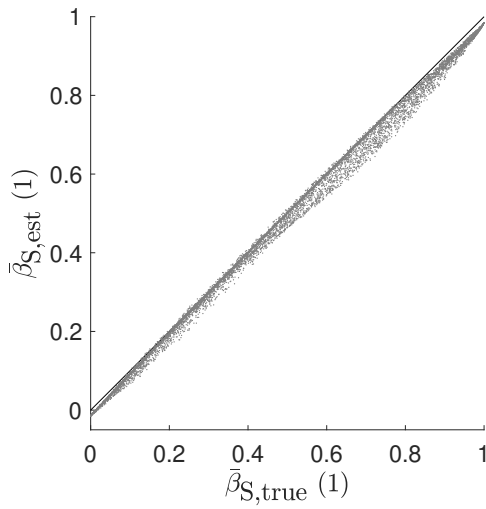
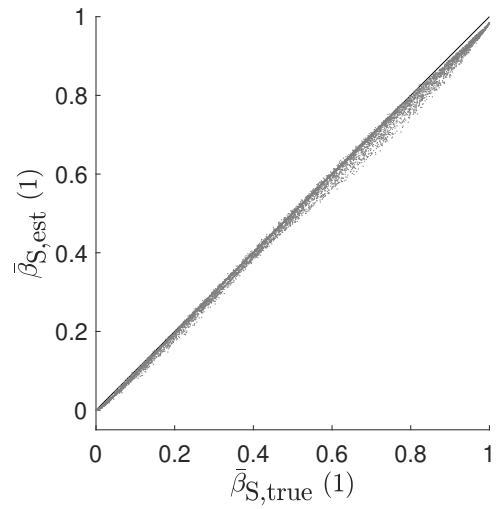
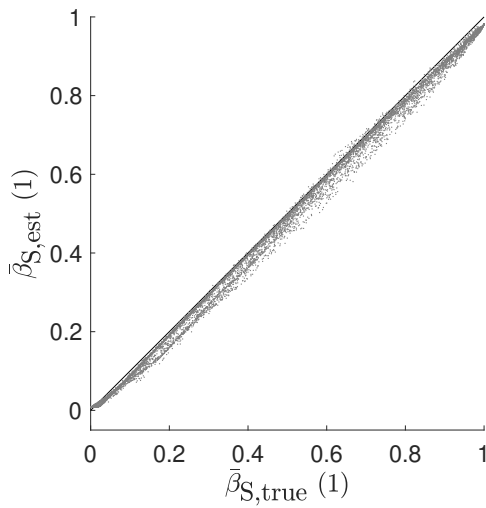
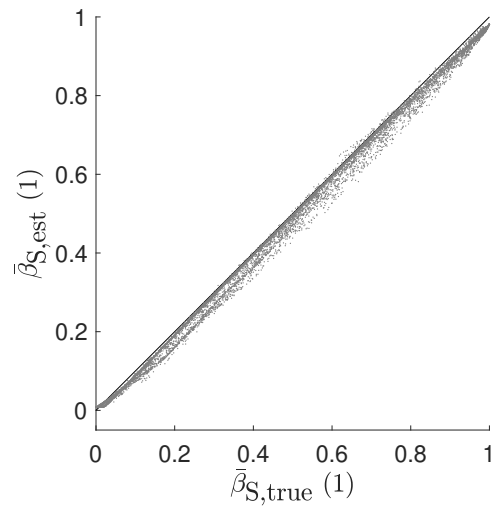
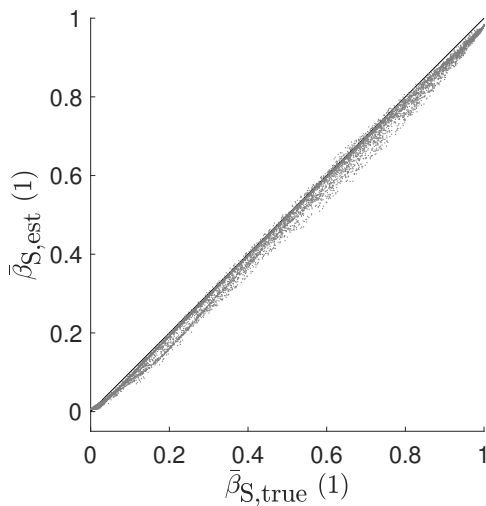
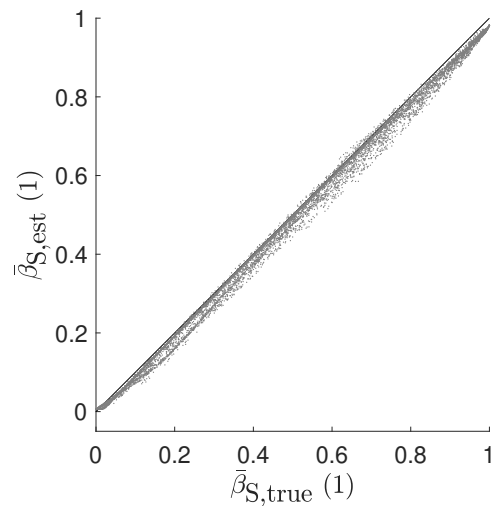


Figure 5.52: OSOA/—

**Figure 5.53:** LMAPnc/–**Figure 5.54:** LMAP/–**Figure 5.55:** LMAP/PCA30**Figure 5.56:** LMAP/INT30**Figure 5.57:** LML/PCA30**Figure 5.58:** LML/INT30

Algorithm	MSE	Algorithm	MSE
OFOA/–	2,328e–03	LMAP/PCA30	1,149e–02
OSOA/–	9,984e–04	LMAP/INT30	1,149e–02
LMAPnc/–	2,331e–02	LML/PCA30	1,135e–02
LMAP/–	7,340e–03	LML/INT30	1,135e–02

**Table 5.9:** Normalized mean square errors.

The simulation results for varied horizontal conveying flow patterns are depicted in figure 5.51 to 5.58. The corresponding normalized MSE is depicted in table 5.9. The results show a very similar behaviour compared to the simulations presented in subsection 5.3.3.

The modified flow samples cause a slightly increase of the variance since they do not correspond to the prior information incorporated to the algorithms. This circumstance is also evident by considering the MSE depicted in table 5.9. Here a slightly increased MSE is evident in every case compared to the results presented in 5.3.3. Though the OSOA implementations show a larger deterioration of the MSE than the different LMAP and LML algorithms. This behaviour is given by the fact that the OSOA algorithms are trained for a specific set of random samples, which do not correspond to the material patterns that have to be reconstructed. The LMAP and LML algorithms in comparison are given by an optimization problem. Indeed a wrong prior distribution  $\pi(\mathbf{x})$  is incorporated to the algorithms. However due to the likelihood function  $\pi(\tilde{\mathbf{d}}|\mathbf{x})$ , still the physics of the ECT sensor are incorporated to the problem. Therefore this kind of algorithm is more robust against variations in the flow profile.

Considering the LMAPnc/– algorithm, the absence of state constraints causes negative estimates for  $\bar{\beta}_{S,\text{est}}$ . The OSOA implementations however obtained valid results with  $0 \leq \bar{\beta}_{S,\text{est}} \leq 1$  in every case although also no state constraints are incorporated. The same behaviour of the algorithms with respect to state constraint was already shown in subsection 5.3.3.

Given this simulation results one can conclude, that the different LMAP and LML algorithms exhibit a more robust behaviour against variations in the flow profiles compared to the optimal approximation algorithms.

### Variation of Vertical Downward Conveying Flow Patterns

In the case of vertical downward conveying flow patterns the modified patterns are given by eccentric Gaussian material distributions. For gravity-driven flow of bulk materials so called density waves can occur, caused by interactions between the particles, the gas and the pipe wall [34]. A cross-sectional representation of those density waves is approximately given by an eccentric Gaussian material distribution.

Due to the eccentricity the particles will accumulate in the area of the pipe wall, in which the Gaussian distribution is displaced. This causes a higher density in this area, modeled by means of higher material values. Two exemplary samples for this flow profiles are depict in figure 5.59. The central point  $\boldsymbol{\mu}$  of the material distribution is selected randomly by

$$\mu_x \propto \mathcal{U}\left(-\frac{r_{i,\text{pipe}}}{2}, \frac{r_{i,\text{pipe}}}{2}\right), \quad (5.6)$$

$$\mu_y \propto \mathcal{U}\left(-\sqrt{\left(\frac{r_{i,\text{pipe}}}{2}\right)^2 - \mu_x^2}, \sqrt{\left(\frac{r_{i,\text{pipe}}}{2}\right)^2 - \mu_x^2}\right), \quad (5.7)$$

where  $\mu_x$  and  $\mu_y$  are the x- and y-coordinate of the central point and  $r_{i,\text{pipe}}$  denotes the inner radius of the ECT sensor. With this the maximum eccentricity is given by the value  $r_{i,\text{pipe}}/2$ .

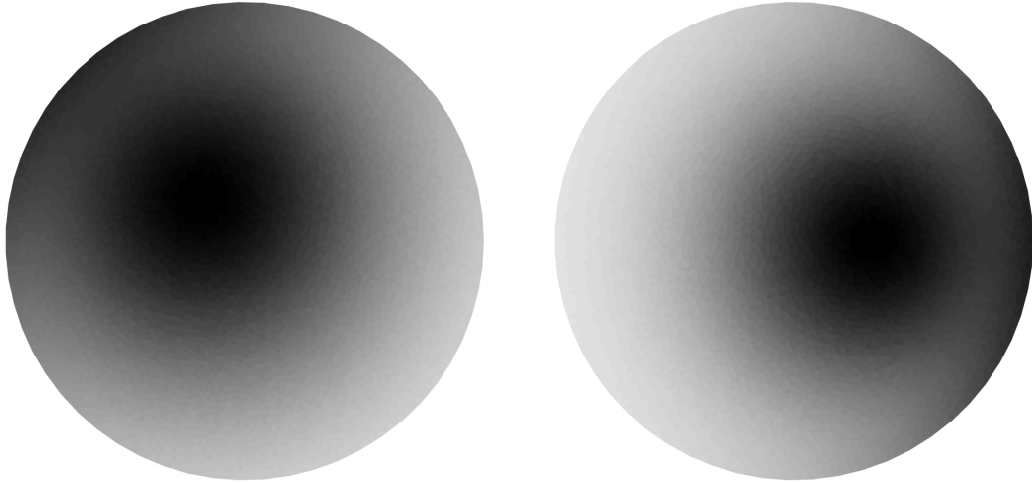


**Figure 5.59:** Exemplary samples for varied vertical downward conveying flow patterns.

## Simulation Results for the Modified Vertical Downward Conveying Flow Patterns

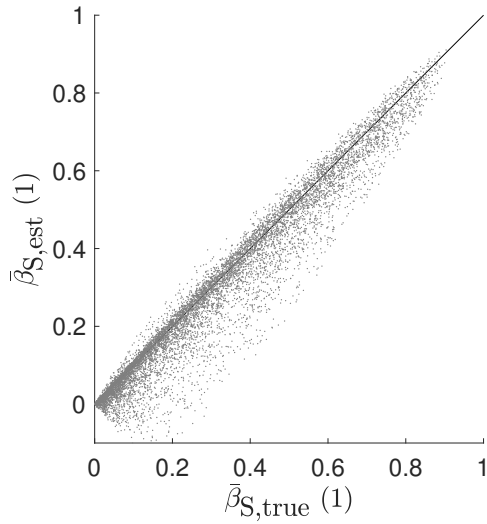


Figure 5.60: OFOA/–

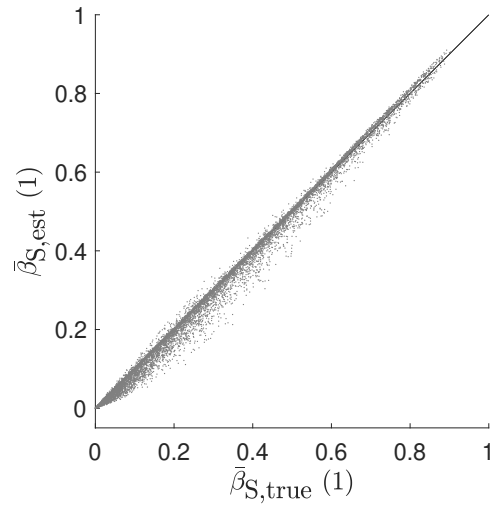


Figure 5.61: OSOA/–

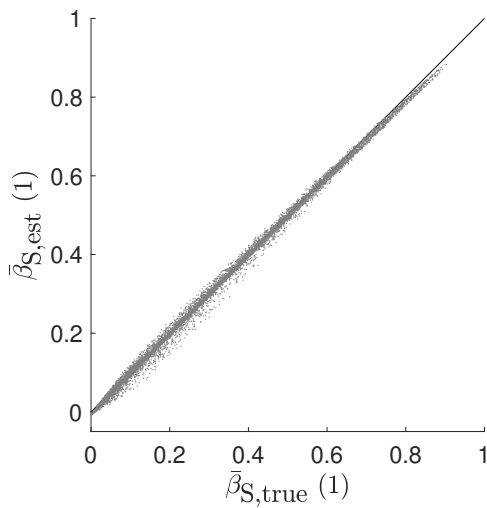


Figure 5.62: LMAPnc/–

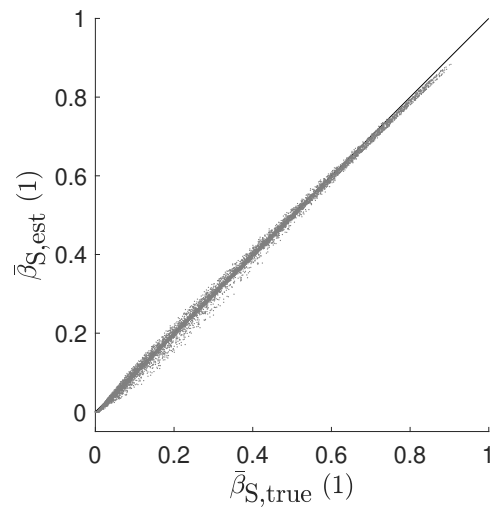


Figure 5.63: LMAP/–

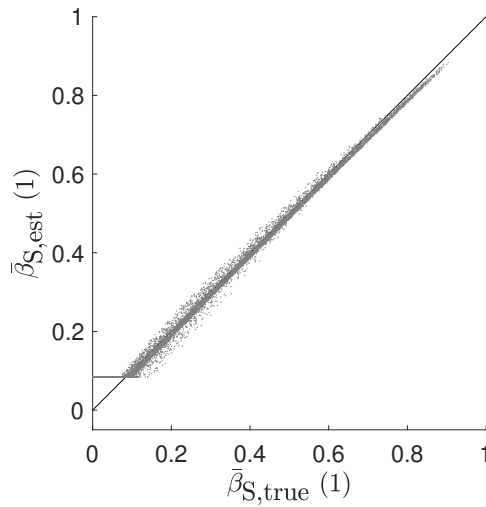


Figure 5.64: LMAP/PCA30

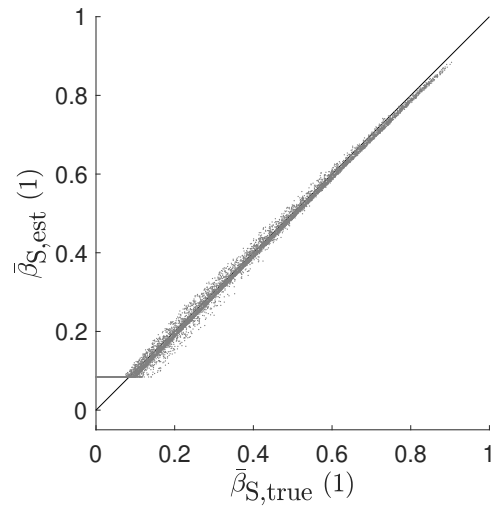


Figure 5.65: LMAP/INT30

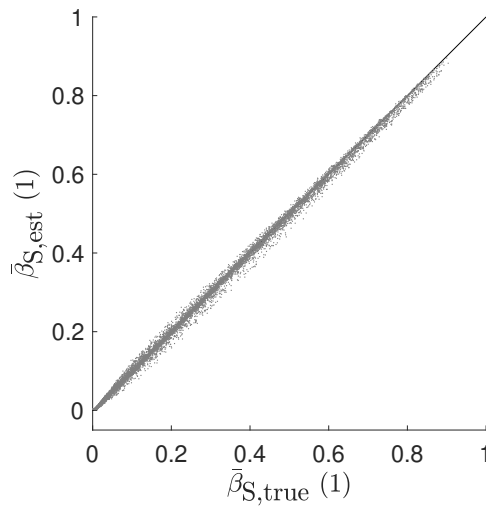


Figure 5.66: LML/PCA30

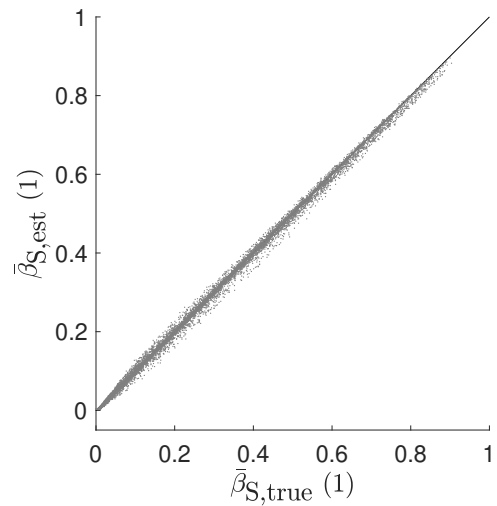


Figure 5.67: LML/INT30

Algorithm	MSE	Algorithm	MSE
OFOA/–	1,201e–01	LMAP/PCA30	9,132e–01
OSOA/–	1,837e–02	LMAP/INT30	9,132e–01
LMAPnc/–	1,488e–02	LML/PCA30	8,299e–03
LMAP/–	1,307e–02	LML/INT30	8,299e–03

Table 5.10: Normalized mean square errors.

Figure 5.60 to 5.67 depict the simulation results obtained with different reconstruction algorithms. The normalised MSE corresponding to the particular algorithms are depicted in table 5.10.

The variation of the flow pattern has a strong impact on the optimal approximation algorithms shown in figure 5.60 and 5.61. The estimation results obtained with the OFOA/– and the OSOA/– algorithm exhibit a large variance of the single samples. Also the variances of the samples obtained with the different LMAP and LML implementations is increased compared to the results presented in subsection 5.3.4. However the deterioration of the estimation results is significantly more pronounced for the optimal approximation algorithms. This is also evident when considering the MSE depicted in table 5.10. The same behaviour was already shown for a variation of the horizontal conveying flow profiles presented previously.

Since no constraints are incorporated by means of the optimal approximation algorithms as well as the LMAPnc/– algorithm negative estimation result with values  $\beta_{S,\text{est}} < 0$  were achieved. The described behaviour is most present for the OFOA/– algorithm.

The LMAP algorithm with an applied state reduction technique is not able to obtain estimation results below a certain value. This circumstance is resulting in large values for the normalised MSE. The same behaviour was already demonstrated and discussed in subsection 5.3.4 for this particular algorithms. The basis vectors of the reduced state representation do not correspond to the true material distributions. Despite this circumstance the LML/PCA30 and LML/INT30 algorithms achieved the lowest MSE values.

Given this simulation results one can conclude, that the different algorithms behave very similar to the results presented in 5.3.4. The variation in the flow profiles causes an increased variance of the sample in every case. Though the different LMAP and LML algorithms exhibit a more robust behaviour against variations in the flow profiles. Similar results are obtained for a variation of horizontal conveying flow samples presented previously.

## 6 Summary and Conclusion

In this thesis the application of ECT for volume concentration estimation in pneumatic conveying systems is analysed. The main subject of this thesis is the adaptation of ECT for this particular application. This covers several topics starting from an investigation of the flow processes within pneumatic conveying. Given this insight an approach is presented, to formulate this knowledge as prior information for different reconstruction algorithms. The estimation of flow parameters by means of ECT is based on the assumption, that the parameter of interest is proportional to the reconstructed permittivity distribution. Therefore an approach is presented to relate the electric material values provided by ECT with the volume concentration. Given this concept a framework is provided in order to implement comprehensive statistical analysis of the estimation performance. The contents of this thesis can be summarized by the following points

- Investigation of the flow processes in pneumatic conveying system and the formulation of meaningful prior information,
- Adaptations of ECT for flow parameter estimation and
- Analysis framework and statistical analyses of the estimation performance.

The first part of this thesis addresses the application of ECT for flow parameter estimation. Therefore the spacial material distributions within pneumatic conveying systems are investigated. Since the reconstruction results are given by a two dimensional material distribution within the sensor, the different flow regimes are summarized by their cross sectional representations. Given this knowledge an approach is presented to generate random samples, suitable to describe the different occurring flow regimes within the conveying process. The random samples are subsequently used as so called sample based prior.

The sample based prior information is incorporated to the reconstruction algorithms in different ways. The so called optimal approximation algorithms are directly trained on a set of random samples  $\mathbf{X}$ . For algorithms such as the MAP estimator, the Kalman filter or the Gibbs sampler in contrast, the prior information has to be formulated by means of a probability density function  $\pi(\mathbf{x})$ . Therefore a Gaussian summary statistic is computed for a set of random samples parametrized by its mean  $\boldsymbol{\mu}_{\mathbf{x}}$  and its covariance matrix  $\boldsymbol{\Sigma}_{\mathbf{x}}$ .

An alternative way for the incorporation of prior information is given by the concept of state reduction. Therefore an projection matrix  $\mathbf{P}_{N_R}$  is assembled in order to perform the mapping between a reduced state space  $\mathbf{x}_R$  and the original state vector  $\mathbf{x}$ . The construction of the projection matrix  $\mathbf{P}_{N_R}$  requires prior information. One known approach is based on a principle component analysis of a set of random samples. Due to the information obtained by the investigation of the spacial material distributions within pneumatic conveying systems also an intuitive way is presented in order to assemble  $\mathbf{P}_{N_R}$ .

To analyse the intrinsic information held by a set of random samples a principle component analysis is performed. Herby the random samples for flow type material distributions are compared to random samples for arbitrary material distributions. This is used to choose a reasonable size for a reduced state representation to incorporate a sufficient amount of prior information by means of the projection matrix  $\mathbf{P}_{N_R}$ .

The reconstruction algorithms provide an estimate for the material distribution within the ECT sensor by means of relative permittivity values  $\varepsilon_r$  of the finite elements. In order to estimate the volume concentration  $\bar{\beta}_S$ , the electrical material values  $\varepsilon_r$  have to be related to the flow parameter of interest. The approach in order to accomplish this estimation is based on the assumption, that the density is proportional to the susceptibility  $\chi = \varepsilon_r - 1$ . Under further assumptions such as a uniform flow and a constant density of the bulk material a linear relation between the volume concentration and the susceptibility is presented.

The second part of this thesis contains a variety of case studies concerning the estimation of the volume concentration  $\bar{\beta}_S$  by means of ECT. Therefore a framework is presented in order to implement comprehensive statistical analysis of the estimation performance. This analysis framework contains the simulation of measurement data using an accurate simulation model of the measurement process. Hereby random samples for different material dis-

tributions are generated and simulated on a fine discretization of the problem domain. This provides the corresponding inter electrode capacitances as well as the nominal volume concentration  $\bar{\beta}_{S,\text{true}}$ . The capacitances are corrupted by additive white Gaussian measurement noise to provide the reconstruction algorithms with realistic measurement data. Due to computational costs, the reconstruction algorithms are implemented on a less accurate simulation model of the measurement process based on a coarse discretization of the problem domain. Out of the reconstructed material distributions on the coarse discretization the estimate for the volume concentration  $\bar{\beta}_{S,\text{est}}$  is calculated. Given this concept a large number of samples is generated. In order to make a statement about the estimation performance, the samples are depicted in scatter plots. Additionally the normalized mean square error is used as a measure of quality for the estimation results. With this it is possible to compare the estimation results for different material distribution and reconstruction algorithms with each other.

Given the analysis framework firstly simulation results for different material distributions are provided. The advantageous use of a dedicated prior information for flow patterns is demonstrated. Statistical analyses of linear back projection type algorithms have shown, that these type of algorithms achieved remarkable results. Linear algorithms are preferable due to their computational efficiency. In addition also a selected number of non-linear and iterative methods have been studied.

Lastly selected parameter studies are implemented in order to investigate the impact of variations of particular process parameters. Thereby parameters such as the number of electrodes, the noise level, and the material values analysed. Additionally variations of the material patterns are implemented. Regarding the variation of the material value the reconstruction algorithms show sufficient robustness against prior material values differing from the true material values. Different material values result in an over- or underestimation of the true volume concentration  $\bar{\beta}_{S,\text{true}}$ . The mean of the samples however is still following a straight line. Therefore this error is easily to overcome by means of calibration. Regarding variation in the flow profiles a large impact on the estimation results provided by the different optimal approximation implementations is evident. The individual MAP and ML type implementations exhibit a more robust behaviour with respect to these variations of the flow profiles.

# References

- [1] Arthur J Jaworski and Tomasz Dyakowski. Application of electrical capacitance tomography for measurement of gas–solids flow characteristics in a pneumatic conveying system. *Meas. Sci. Technol.*, 12:1109–1119, 2001.
- [2] G.A. Jama, G.E. Klinzing, and F. Rizk. An investigation of the prevailing flow patterns and pressure fluctuation near the pressure minimum and unstable conveying zone of pneumatic transport system. *Powder Technology*, 112:87–93, 2000.
- [3] M. Neumayer and T. Bretterkieber. Reduced electrical capacitance tomography sensor for flow profile estimation. In *IEEE SENSORS 2014 Proceedings*, pages 1300–1303, 2014.
- [4] Y. Yan. Flow rate measurement of bulk solids in pneumatic pipelines—problems and solutions. *Bulk Solids Handling*, 6(3):447–456, 1995.
- [5] J. Hadamard. Sur les problèmes aux limites partielles et leur signification physique. *Bull. Univ. of Princeton*, pages 49–52, 1902.
- [6] Siegel W. *Pneumatische Förderung: Grundlagen, Auslegung, Anlagenbau, Betrieb*. Vogel Fachbuch-Verlag, Würzburg, 1991.
- [7] M. Neumayer, H. Zangl, D. Watzenig, and A. Fuchs. *New Developments and Applications in Sensing Technology*, volume 83, chapter Current Reconstruction Algorithms in Electrical Capacitance Tomography, pages 65–106. Springer, 2011.
- [8] W. Yang. Design of electrical capacitance tomography sensors. *Meas. Sci. Technol.*, 21(4), 2010.
- [9] J. Kaipio and E. Somersalo. *Statistical and Computational Inverse Problems*. Springer, 2004.

- 
- [10] M. Neumayer. *Accelerated Bayesian Inversion and Calibration for Electrical Tomography*. PhD thesis, Graz University of Technology, 2011.
- [11] R.P. Feynman. *Feynman Lectures On Physics (3 Volume Set)*. Addison-Wesley Longman, Amsterdam, 1998.
- [12] H. Wegleitner A. Fuchs G. Holler B. Kortschak. Analysis of hardware concepts for electrical capacitance tomography applications. In *Proceedings of the IEEE Sensor Conference*, volume 7, pages 436–519, 2005.
- [13] A.C. Polycarpou. Introduction to the finite element method in electromagnetics. *Synthesis Lectures on Computational Electromagnetics*, 5:1–126, 2006.
- [14] H. Yan F.Q. Shao S. Wang. Fast calculation of sensitivity distributions in capacitance tomography sensors. *Electronics Letters*, 34(20):1936–1937, October 1998.
- [15] B. Brandstätter. Jacobian calculation for electrical impedance tomography based on the reciprocity principle. *IEEE Transactions on Magnetics*, 39(3):1309 – 1312, May 2003.
- [16] N. Young. An introduction to hilbert space. *Cambridge University Press, New York, NY, USA*, 1988.
- [17] W. W. Hager. Updating the inverse of a matrix. *SIAM Review*, 31(2):221–239, 1989.
- [18] C. Fox G. Nicholls. Sampling conductivity images via mcmc. In *University of Leeds*, page 91–100, 1997.
- [19] M. Neumayer, T. Bretterkieber, M. Flatscher, and S. Puttinger. Pca based state reduction for invers problems using prior information. *COMPEL*, 36(5):1430–1441, 2017.
- [20] M. Neumayer, M. Flatscher, T. Bretterkieber, and S. Puttinger. Prior based state reduction in backprojection type imaging algorithms for electrical tomography. *I2MTC*, 2018.
- [21] H. Zangl, D. Watzenig, G. Steiner, a. Fuchs, and H. Wegleitner. Noniterative reconstruction for electrical tomography using optimal first and second order approximations. In *World Congress on Industrial Process Tomography WCIPT5*, 2007.

- 
- [22] Steven M. Kay. *Fundamentals of Statistical Signal Processing: Estimation Theory*. Prentice Hall PTR, 1993.
- [23] D. Simon. *Optimal State Estimation: Kalman, H-infinity, and Nonlinear Approaches*. John Wiley & Sons, Chichester, 2006.
- [24] R.E. Kalman. A new approach to linear filtering and prediction problems. *Journal Basic Engineering*, 82:35–45, 1960.
- [25] Kim H.C., Kim K.Y., Park J.W., and Lee H.J. Electrical impedance tomography reconstruction algorithm using extended kalman filter. In *of the IEEE International Symposium on Industrial Electronics, ISIE*, volume 3, pages 1677–1681, 2001.
- [26] D. Watzenig, G. Steiner, and B. Brandstätter. Managing noisy measurement data by means of statistical parameter estimation in electrical capacitance tomography. In: *Proc. of the 13th International IGTE Symposium*, 2004.
- [27] D. Simon and T.L. Chia. Kalman filtering with state equality constraints. *IEEE Transactions on Aerospace and Electronic Systems*, 38(1):128–136, 2002.
- [28] W. R. Gilks S. Richardson D. J. Spiegelhalter. *Markov chain Monte Carlo in practice*. Chapman & Hall/CRC, 1996.
- [29] L. Tierney. Markov chains for exploring posterior distributions. *Annals of Statistics*, 15:116–132, 1985.
- [30] G. Casella E. I. George. Explaining the gibbs sampler. *The American Statistician*, 46(3):167–174, 1992.
- [31] W. R. Gilks N. G. Best K. K. C. Tan. Adaptive rejection metropolis sampling within gibbs sampling. *Journal of the Royal Statistical Society. Series C (Applied Statistics)*, 44(4):455–472, 1995.
- [32] M. Weber. *Strömungsfördertechnik*. Krauskopfverlag, 1974.
- [33] M. Kraume. *Transportvorgänge in der Verfahrenstechnik*. Springer Vieweg, 2012.
- [34] Elizabeth D. Liss, Stephen L. Conway, and Benjamin J. Glasser. Density waves in gravity-driven granular flow through a channel. *Physics of Fluids*, 14(9):3309–3326, 2002.

- [35] Q. Guan, W. Wang, and J. Zhang. Flow patterns of pneumatic conveying of pulverized coal in horizontal pipes for pressurized conditions. In *2011 Asia-Pacific Power and Energy Engineering Conference*, pages 1–4, 2011.